A Measurement of the $Z\gamma$ Cross Section and Limits on Anomalous Triple Gauge Couplings at $\sqrt{s} = 7$ TeV Using CMS

by

Lindsey Gray

A dissertation submitted in partial fulfillment of

the requirements for the degree of

Doctor of Philosophy

(Physics)

at the

University of Wisconsin – Madison

2012

Date of final oral examination: 08/27/12

The dissertation is approved by the following members of the Final Oral Committee:

Sridhara Dasu, Professor of Physics

Wesley Smith, Bjorn Wiik Professor of Physics

Matthew Herndon, Professor of Physics

Lisa Everett, Associate Professor of Physics

Terrence Millar, Professor of Mathematics

A Measurement of the Zγ Cross Section and Limits on Anomalous Triple Gauge Couplings at $\sqrt{s} = 7$ TeV Using CMS

Lindsey Gray

Under the supervision of Professor Sridhara R. Dasu

At the University of Wisconsin–Madison

A study of the properties of the Zγ diboson system is presented using 5.0 fb^{-1} of proton-proton collision data from the LHC using the CMS detector. The pp $\to Z(\to \mu\mu)\gamma$ and pp $\to Z(\to ee)\gamma$ production cross sections are measured within the fiducial volume of CMS with a combined measurement of $\sigma_{\ell\ell\gamma} = 5.33 \pm 0.08$ (stat.) $\pm$ 0.25 (syst.) $\pm$ 0.12 (lumi.) pb that is in good agreement with Standard Model predictions. Upper limits on the neutral anomalous triple gauge couplings set are the most stringent limits on these couplings to date, with allowed regions: $-0.010 < h_3^\gamma < 0.010$, $-8.8 \cdot 10^{-5} < h_4^\gamma < 8.8 \cdot 10^{-5}$, $-8.6 \cdot 10^{-3} < h_3^Z < 8.3 \cdot 10^{-3}$, and $-8.0 \cdot 10^{-5} < h_4^Z < 7.9 \cdot 10^{-5}$ at 95% confidence level.

Acknowledgements

The body of work presented in this thesis represents the end of a nine year journey beginning in undergraduate, so there's a great number of people that I need to thank for their support along the years. First things first, chronologically, I'd like to thank Darin Acosta, Holger Stöck, and Bobby Scurlock for supporting, tolerating, and teaching me as an undergraduate at the University of Florida physics department. Without their enthusiasm and truly vast amount of knowledge I would have never learned about hardware and software development in HEP, nor would I have been with CMS since late 2003. I'd also like to thank my then colleagues, Nick Park and Evan Kim for their enthusiasm, friendship, and coding standards (one must learn this somewhere).

At The University of Wisconsin − Madison I'd first and foremost like to thank Professors Wesley Smith and Sridhara Dasu for their readily shared wealth of information, helpful ideas regarding analysis, and constant support throughout my graduate studies. During my stay at CERN Armando Lanaro played a large role in keeping me, at least somewhat, on rails and I'd like to thank him for the many useful discussions concerning analysis planning and physics. I'd like to thank Frank Petriello and Ulrich Baur (*en memoriam*) for their support during my somewhat extended period attempting to write a NLO accurate Zγ event generator. While the NLO part never ended up working in full due to issues with fragmentation photons, the attempt

forced me to learn a great deal about event generators and has helped me build a rich understanding of how Monte Carlos work. My fellow students Jeff Klukas, Mike Anderson, Ian Ross, and Michail Bachtis have all had helpful ideas and have been good friends and colleagues over the years.

At CERN I had a brief stint studying the physics of quarkonia under the direction of Carlos Lorenço and Hermine Wöhri. I learned a great deal from them both about polarization measurements and this was absolutely key to coming up with the method described in Appendix C. Additionally, I'd like to thank Greg Rakness for being amazingly helpful during my time as a on-call shifter for the CSCs. The CMS Vγ group has been absolutely instrumental, I'd like to thank specifically Yurii Maravin, Irakli Svindradze, Senka Djurić, and Jan Veverka who have all been great colleagues and friends along the way. The CERN Board Games club also deserves mention here, if not purely for keeping me sane all this time and the generally awesome nature of the people who comprise the group, foremost among them Peter Loscutoff, Johannes Ebke, Nathan Triplett, Rob Lambert, Helen Lambert, Seth Zenz, and Hugo Day. For this same reason Ryan Carroll also has my sincere gratitude.

Slightly outside the realm of direct contribution but most certainly worthy of thanks, I'd like to express my deep gratitude to Nathan Whitehorn and Elizabeth Heath-Heckman for giving me a place to stay in Madison while writing and all the other times I've visited. Also, I'd like to thank Corrinne Mills for her understanding and support while I was writing. Finally, I'd like to thank my parents, Dona Crelia and John Paul Gray, for their unwavering support of my decision to pursue physics and their patience in all of this.

Contents

Acknowledgements **iii**

List of Figures **ix**

List of Tables **xviii**

1 Introduction **1**

1.1 The Standard Model 2

1.2 Quarks and Leptons 2

1.3 Bosons 3

1.3.1 Electroweak Physics 4

1.3.2 The Higgs Boson and Electroweak Symmetry Breaking 6

1.3.3 Quantum Chromodynamics (QCD) 7

1.4 Proton-Proton Collisions 8

1.5 The Zγ Cross Section 10

2 Zγ Phenomenology **13**

2.1 Proton Collisions at the LHC 14

2.2 Standard Model Zγ Production 16

2.2.1 Z+Jets as a Background to Zγ 21

2.3 Anomalous Zγ Production 22

2.4 Observables Sensitive to aTGCs 25

3 Experimental Setup **29**

3.1 The Large Hadron Collider 29

3.1.1 The Luminosity Frontier 34

3.2 The Compact Muon Solenoid Experiment 37

3.2.1 CMS Geometry 38

3.2.2 Silicon Tracker 39

Pixel Detector 39

Silicon Strip Tracker 41

3.2.3 Electromagnetic Calorimeter 43

3.2.4 Hadronic Calorimeter 46

3.2.5 Muon Detectors 48

Drift Tubes 49

Cathode Strip Chambers 51

Resistive Plate Chambers 53

3.2.6 Trigger 54

Level-1 Trigger 55

High Level Trigger 57

4 Event Simulation **59**

4.1 Phase Space Integration and Event Generators 60

4.1.1 Matrix Element Generators 61

4.1.2 Parton Shower Monte Carlo 62

4.1.3 Merging Matrix Element Events with Parton Showers 64

4.2 Detector Simulation 66

5 Event Reconstruction **69**

5.1 Track and Primary Vertex Reconstruction 69

5.2 Muon Reconstruction 71

5.3 Electron Reconstruction 72

5.4 Photon Reconstruction 74

6 Analysis Methodology **77**

6.1 Event Selection 77

6.1.1 Trigger Requirements 78

6.1.2 Electron Selection 79

6.1.3 Photon Selection 84

6.1.4 Muon Selection 89

6.1.5 Event Topology 92

6.2 Background Estimation 92

6.2.1 Signal Component Shape 93

6.2.2 Background Component Shape 93

6.2.3 Two Component Fit 95

6.3 Comparison of Simulation to Data 95

6.4 Systematic Uncertainties 100

6.4.1 Luminosity 100

6.4.2 Electron and Photon Energy Scales 100

6.4.3 Photon and Electron Energy Resolution 101

6.4.4 Pileup Modeling 101

6.4.5 PDF Uncertainties 102

6.4.6 Data/Monte Carlo Efficiency Scale Factors 102

6.4.7 Background Estimation 103

Template method 103

7 The Measurement of the Zγ Cross Section **109**

7.1 Extraction of the Cross Section 110

8 Anomalous Triple Gauge Coupling Limits **113**

8.1 $ZZ\gamma$ and $Z\gamma\gamma$ couplings 114

8.2 Likelihood Formalism 114

8.2.1 Tests of Two Limit Setting Techniques 116

8.3 Limits on Zγ Anomalous Triple Gauge Couplings 118

8.4 Previous Results 119

8.4.1 The LEP Experiments 120

8.4.2 Experiments at the Tevatron 125

8.4.3 aTGC Limits from ATLAS with 1 fb^{-1} 126

8.4.4 Comparison To Presented Results 127

9 Conclusions **129**

9.1 Summary 129

9.2 Outlook 130

Bibliography **133**

A Template Method Fit Results **143**

B Other Anomalous Triple Gauge Coupling Measurements **151**

C A Data-Driven Method for Extraction of Spin Alignment Anisotropy Parameters **157**

List of Figures

1.1 The $SU(2)_L$ structure of each generation in the Standard Model. Quarks and charged leptons having a right handed singlet component. 5

1.2 Predictions for the cross sections of various SM processes, the heirarchy of rates that depends on the bosons involved. Wγ and Zγ have larger cross sections since the photon is massless. 10

2.1 The parton distribution functions for the quark and gluon contituents of a proton at two different values of momentum transfer. The u and d components are dominated by valence quarks at high x while s, c, b, and g are more prevalent at low x. The gluon fraction at low x increases by orders of magnitude at large momentum transfers. [12] 14

2.2 SM Z boson production and decay at a hadron collider. Only quarks are present in the initial state, but the final state can be quarks or leptons. . 16

2.3 The two leading order α_s diagrams for Zγ production in the SM. 18

2.4 The leading order α_s diagrams for FSR Zγ production in the SM. 18

2.5 The unique real emission diagrams for ISR Zγ. There are additional diagrams resulting from the permutation and crossings of the Z, γ, and final state parton. 19

2.6 The loop diagrams for ISR Zγ. The same initial states apply to the crossed graph in Figure 2.3 19
2.7 The photon fragmentation contribution to Zγ production at NLO. In the gluon contribution (left) there is additional hadronic radiation from the non-perturbative process to conserve color flow. The quark contribution also contains non-perturbative effects due to collinearity of the photon with the quark. 20
2.8 The loop diagrams for FSR Zγ. 20
2.9 The real emission diagrams for FSR Zγ. 21
2.10 The stages of jet evolution, starting from the perturbatively based scattering and ending with the nonperturbative hadronization. 22
2.11 The general form of the ZγV, vertex. V=γ,Z 23
2.12 The ZγZ, vertex function with the four couplings allowed by gauge and lorentz invariance. 23
2.13 The change in the photon p_T distribution coming from h_3 and h_4 type anomalous couplings. The standard model is shown for comparison. . . . 26
2.14 Change in the Z boson spin alignment resulting from aTGCs. 27

3.1 The layout and interconnections of the CERN accelerator complex. The LHC is the last stage in a multi-level injector chain starting with linear accelerators. [36] 30
3.2 A schematic view of the construction of an LHC main dipole. All components within the iron yoke (yellow shaded area) are cooled to a temperature of 1.9K. 33
3.3 An overview of the CMS experiment, given to scale. [32] 36

3.4 A cross section of the CMS Silicon Tracker, depicting its geometry in the rz plane of the detector and demonstrating η coverage of the instrumented region. [32] 40

3.5 The number of radiation lengths, x, of material in the CMS pixel detector as a function of η. The immense data output and power usage of the pixel detector requires, for its size, intensive cabling and cooling. [32] 40

3.6 The number of radiation lengths, x, of material in the CMS silicon tracker, including the pixels, as a function of η. Regions with a large radiation length are prone to generating converted photons. [32] 42

3.7 The layout of the barrel ECAL (EB) and endcap ECAL (EE). The EB crystals project towards the center of the detector to aid in reconstruction and uniform containment of electromagnetic particles that stop in the calorimeter. [32] 45

3.8 The layout of the various components of the CMS hadronic calorimetery. The Barrel HCAL (HB) and Endcap ECAL (HE) cover up to $\eta < 3.0$. The Outer HCAL (HO) helps to measure showers which are not contained by HB or HE. The Forward HCAL (HF) covers $3.0 < |\eta| < 5.0$, making the HCAL nearly hermetic in solid angle. [32] 47

3.9 An rz cross section of the CMS muon system, demonstrating the η coverage and overlap of all constituent subsystems. [46] 49

3.10 The momentum resolution of muons using the three possible choices of momentum measurements, from the silicon tracker alone, the muon system alone and the combined tracking fit of the silicon track and muon systems. Note the improved momentum measurement at large p_T from including the muon system. [32] 50

3.11 A schematic representation of a single drift tube in one cms drift tube chamber. The position of charged particles traversing the chamber is inferred from the 'charge radius' of ionized particles that drift towards the anode wire. [32] 51
3.12 The layout of a cathode strip chamber in CMS. The figure on the right demonstrates how the traversing particle's position and timing are deduced by induced and deposited charge in the chamber. [32] 52
3.13 Resistive Plate Chambers are of significantly simpler design than the DTs or CSCs and are used as a robust redundant system to the other muon subsystems. The detector operates in a similar manner to the wires of the CSCs and have a timing resolution of roughly 1 ns. [32] 53
3.14 A diagramatic representation of the information into, within and out of the CMS Level-1 Trigger System which is used to reject the majority of of the uninteresting collisions at the LHC. [48] 55
3.15 The improvement in the muon momentum resolution when including the information from the silicon tracker in the High Level Trigger for different muon system alignment scenarios. Note that the muon resolution improves by nearly an order of magnitude when including the silicon tracker information. [47] 58

4.1 An example event demonstrating schematically all of the effects simulated by a parton shower monte carlo in a hadronic Z decay, including the parton shower (colored lines labelled by quarks) and hadronization (black lines labelled by hadrons). [56] 62
4.2 D0 data demonstrating the disagreement of the Pythia MC program with W p_T data, even after an updated tune. [57] 64

4.3 Matching results using the MLM technique, note that above the matching threshold d_{match} the contribution from parton-level radiation dominates and describes the observed distribution from D0. [57] 66

5.1 An artistic representation of the ECAL-based and tracker-based components of electron reconstruction. The supercluster is the η-φ strip containing the energy deposits of the electron and any radiated photons. . . 73

6.1 Electron efficiency scale factors for the 2011 A run period. 82
6.2 Electron efficiency scale factors for the 2011 B run period. 83
6.3 Photon efficiency scale factors for the 2011 A run period. 87
6.4 Photon efficiency scale factors for the 2011 B run period. 88
6.5 Muon efficiency scale factors for the 2011 A and B run periods. 91
6.6 The $\sigma_{i\eta i\eta}$ distributions for barrel (left) and endcap (right) for Runs 2011 A and B. The difference of mean values between MC and data are accounted for by shifting the simulation signal shapes. 94
6.7 An example template fit in the 15-20 GeV bin in the barrel (left) and endcap (right).The signal distribution is indicated by the blue line and the background is indicated by the red line. The full set of template fit results may be found in Appendix A. 96
6.8 Dilepton invariant mass vs. $\ell\ell\gamma$ invariant mass for the $ee\gamma$ channel (top) and $\mu\mu\gamma$ channel (bottom). The ISR dominated and FSR dominated regions can be clearly seen as vertical and horizontal bands, respectively. 97
6.9 The fully selected distributions for the $ee\gamma$ channel. 98
6.10 The fully selected distributions for the $\mu\mu\gamma$ channel. 99

6.11 The uncertainty for 'sideband bias' and 'signal contamination' on the background template for barrel (left) and endcap (right). The change in the estimated number of background events due to 'anti-isolation' requirement (sideband bias) is given as a function of photon p_{T} as red circles, while the contamination from genuine photons are given as blue dots. The overall effect is given as black. 105

6.12 The results of applying the template method to the $\sigma_{i\eta i\eta}$ distributions in the observed data for the electron (top) and muon (bottom) channels in the EB (left) and EE (right). The black error bar is the statistical error and the hashed region represents additional systematic error. The significantly higher data-derived fake rate is expected. 106

7.1 The summary of all cross section measurements for the Zγ channel. . . . 112

8.1 CLs limits in the scenario of anomalous triple gauge couplings for a toy MC study representing 3 fb^{-1}. The left plot demonstrates the response of the limits in the case of no aTGC. The right plot demonstrates the response with an aTGC signal represent, and the non-exclusion of the null hypothesis, the Standard Model. 117

8.2 Profile likelihood limits on anomalous triply gauge couplings for the same toy MC study as Figure 8.1. Here the SM is excluded but only one of the degenerate allowed regions is found as shown in the likelihood scan in the right plot. 118

8.3 95% confidence level contours for $Z\gamma\gamma$ (left) and $ZZ\gamma$ (right) couplings from the combined information of the electron and muon channels. The observed limits are within one standard deviation of the expected sensitivity. 119

8.4 Limits on anomalous triple gauge couplings from the DELPHI collaboration using the $e^+e^- \to \nu\bar{\nu}\gamma$ final state. Limits are set on $h_3^{Z,\gamma}$ with a cutoff scale $\Lambda = 1$ TeV and n = 3. The square points correspond to the unitarity bounds of for this cutoff scale. [82] 121

8.5 Limits on anomalous triple gauge couplings from the L3 collaboration using the $e^+e^- \to \nu\bar{\nu}\gamma$ final state. Limits are set on $h_{3,4}^{Z}$ with cutoff scales $\Lambda = 0.5$ & 1 TeV and n = 3. A comparison to the CDF collaboration's results is displayed as well. [83] 122

8.6 Limits on anomalous triple gauge couplings from the ALEPH collaboration using the $e^+e^- \to q\bar{q}\gamma$ final state. Limits are set on all eight anomalous couplings using a reweighing technique. Both p_T and angular information are input to the fit. No form factor is used. [85] 123

8.7 Limits on anomalous triple gauge couplings from the OPAL collaboration using the $e^+e^- \to q\bar{q}\gamma$ and $e^+e^- \to \nu\bar{\nu}\gamma$ final states. Limits are set on all eight anomalous couplings using a multidimensional fit based on MC yields. Both p_T and angular information are input to the fit. No form factor is used. [29] 124

8.8 Limits from D0 on anomalous triple gauge couplings using all leptonic decay modes of the Z except that to taus. The spectrum shown to the left is for the $\nu\bar{\nu}\gamma$ final state only. [91] 126

8.9 Current limits from CDF on anomalous triple gauge couplings including all leptonic decays of the Z aside from taus. [90] 126

8.10 Current one dimensional limits from ATLAS using 1 fb^{-1} of integrated luminosity collected in 2011. A comparison to CDF, D0 and CMS 36 pb^{-1} results is shown. [92] 127

A.1 Template fit results in the ECAL barrel for 15 GeV $< p_{\mathrm{T}}^{\gamma} <$ 35 GeV in the muon channel. The blue line is the signal template and the red line is the background template. 143

A.2 Template fit results in the ECAL barrel for 35 GeV $< p_{\mathrm{T}}^{\gamma} <$ 500 GeV in the muon channel. The blue line is the signal template and the red line is the background template. 144

A.3 Template fit results in the ECAL endcap for 15 GeV $< p_{\mathrm{T}}^{\gamma} <$ 60 GeV in the muon channel. The blue line is the signal template and the red line is the background template. 145

A.4 Template fit results in the ECAL endcap for 60 GeV $< p_{\mathrm{T}}^{\gamma} <$ 500 GeV in the muon channel. The blue line is the signal template and the red line is the background template. 146

A.5 Template fit results in the ECAL barrel for 15 GeV $< p_{\mathrm{T}}^{\gamma} <$ 30 GeV in the electron channel. The blue line is the signal template and the red line is the background template. 146

A.6 Template fit results in the ECAL barrel for 30 GeV $< p_{\mathrm{T}}^{\gamma} <$ 500 GeV in the electron channel. The blue line is the signal template and the red line is the background template. 147

A.7 Template fit results in the ECAL endcap for 15 GeV $< p_{\mathrm{T}}^{\gamma} <$ 60 GeV in the electron channel. The blue line is the signal template and the red line is the background template. 148

A.8 Template fit results in the ECAL endcap for 60 GeV $< p_{\mathrm{T}}^{\gamma} <$ 500 GeV in the electron channel. The blue line is the signal template and the red line is the background template. 149

B.1 The LO α_S diagrams for Vγ production, where V=W,Z,γ^*. The Wγ coupling occurs naturally in the SM, unlike Zγ. In the case of Wγ production the charged lepton is radiating the photon in the FSR diagram. 151

B.2 The two (top) and one (bottom) dimensional limits on $\Delta\kappa_\gamma$ and λ_γ set with the electron and muon channels of the Wγ analysis. The two bottom plots are cross sections of the top plot when the coupling not being plotted is zero. 153

B.3 The LO α_S diagrams for VV production, where V,V'=W,Z. TGCs occur naturally in the SM between the massive vector bosons, except ZZ. . . . 154

B.4 The two dimensional limits for ZZ anomalous triple gauge couplings. The observed limit is within one sigma of the observed and sets the most stringent limits to date on ZZ aTGCs. [99] 154

C.1 A typical acceptance map used in polarization measurements, binned in $\cos\theta$ and φ. 159

C.2 The one-to-one correspondance between a chosen polarization frame and the lab frame, by way of a unique lorentz boost. 160

C.3 The phase space scan of the decay of a Z boson with $p_{\mathrm{T}} = 30$ GeV using the Zγ analysis cuts, the red regions are where both leptons are within kinematic cuts and white is where at least one is not. 161

C.4 The pull distributions of the polarization parameters given in when all true values of parameters are zero, *i.e.* isotropic distribution. All distributions have a mean consistent with zero and a standard deviation of one, implying that there is no bias. 162

C.5 The pull distributions of the polarization parameters given in when true $\lambda_\theta = 0.5$ and all other parameters are zero. All distributions have a mean consistent with zero and a standard deviation of one, implying that there is no bias. 163

C.6 The pull distributions of the polarization parameters given in when true $\lambda_\theta = -0.5$ and all other parameters are zero. All distributions have a mean consistent with zero and a standard deviation of one, implying that there is no bias. 164

List of Tables

1.1 The organization of the Standard Model matter particles. 3

1.2 The force mediating bosons of the Standard Model. Gluons, Weak gauge bosons and the photon in addition to their couplings and masses. 4

6.1 Selection criteria for the WP80 and WP85 electron candidates in the ECAL barrel and ECAL endcap. 81

6.2 Photon identification and isolation criteria. The $\sigma_{i\eta i\eta}$ variable is used in a fit to determine the estimated fraction of jets reconstructed as photons which pass all cuts. Effective areas, A_{eff} for EB and EE are given in Table 6.3. 85

6.3 A_{eff} used for PU correction for photon selection for barrel and endcap, respectively. 86

6.4 The photon pixel seed efficiencies as derived from photon FSR tag-and-probe. 86

6.5 Muon identification and isolation requirements. The loose selection is used to identify muons from Z candidates, while the tight selection is used for the W candidates. 89

6.6 Z/γ^*+jets background estimation for the template method compared to MC truth(Z+jets only) using full 2011 dataset. The uncertainty for the data-driven method is statistical and systematic, while the MC truth uncertainty is statistical only. 105

6.7 A summary of all systematic uncertainties on $A \cdot \varepsilon$, ρ_{eff}, N_{sig} and Luminosity. 107

7.1 Summary of parameter values for the $Z\gamma$ cross section measurement for the full 2011 dataset. 110

7.2 The summary of the Zγcross section measurements and predictions for photon $p_{\text{T}} > 60$ and 90 GeV. 112

8.1 One-dimensional limits on $Z\gamma$ anomalous trilinear gauge couplings. . . . 119

B.1 The one dimensional anomalous triple gauge coupling limits for ZZ. . . . 155

Chapter 1

Introduction

The Large Hadron Collider (LHC) is a high energy proton-proton collider built with the purpose of studying the fundamental interactions of nature on the smallest of distances scales. The LHC is designed to measure and verify if all aspects of the modern theory of fundamental interactions and matter, the Standard Model (SM), describe nature, and, if not, to measure the deviations beyond its predictions. Key among the topics to be studied within the SM are the mechanism by which the carriers of the Weak Force, the $W^{\pm}$ and Z_0 acquire mass in the context of the search for the Higgs boson, the corresponding lack of mass of the photon, and interactions between the W, Z, and photon. In particular, direct interactions between the Z and photon are predicted to not exist within the SM.

The Compact Muon Solenoid (CMS) detector is a general purpose particle detector located at one of the collision points of the two proton beams in the LHC. It is designed to perform these studies with unprecidented accuracy and precision. Therefore, searching for and analyzing events occuring in the CMS detector that contain both a Z and a photon is a powerful tool for validating the SM and in the search for possible Beyond Standard Model (BSM) effects. Any significant deviation from the

predicted total rate or distributions of Z production with an associated photon is a direct sign of new physics.

1.1 The Standard Model

The Standard Model is currently the most complete and well supported theoretical description of fundamental interactions in nature. The two main categories of particles are fermions, with spin-$\frac{1}{2}$, and bosons, with integer valued spin. The matter particles, quarks and leptons, are fermions. Quarks and leptons interact with each other by exchanging quanta of various forces which are bosons. Every particle also has a corresponding anti-particle with opposite quantum numbers.

The Standard Model describes the interactions of the electromagnetic, strong, and weak forces. The electromagnetic force is mediated by photons and gives rise to the world around us, defining how atoms form and interact with each other. Gluons mediate the strong force that determines the properties and formation of nuclei. The weak force is mediated by the W and Z bosons which govern nuclear decay. The Standard Model describes these forces accurately from the scale of atoms to the subatomic, making it a triumph of modern physics.

1.2 Quarks and Leptons

Quarks and leptons are spin-$\frac{1}{2}$ particles, fermions, that comprise all observed matter in the universe. Leptons do not interact via the strong force and are organized into three generations of doublets, sets of two fields that transform together, consisting of one charged lepton and one neutral lepton. All leptons interact via the weak force while only the charged leptons interact via the electromagnetic force. The charged

leptons are: the electron (e), muon (μ), and tau (τ) and each charged lepton has the charge of the electron. The neutral leptons are known as neutrinos and in each generation are prefixed by the name of the charged lepton in their doublet. All of the charged leptons have non-negligible mass while the neutrinos' masses are zero in the Standard Model. However, modern experiments have shown that the mass-squared-differences between different generations of neutrino are non-zero [1–4], indicating that neutrinos also have a very small mass.

Quarks and Leptons in the SM			
Quarks	up	charm	top
	down	strange	bottom
Leptons	ν_e	ν_μ	ν_τ
	e	μ	τ

Table 1.1: The organization of the Standard Model matter particles.

Quarks interact via the strong force in addition to the weak and electromagnetic forces. Quarks are organized into three generations of doublets with one 'up' type quark with electric charge $\frac{2}{3}$ and one 'down' type quark with charge $-\frac{1}{3}$. The up and down type quarks additionally differ by their weak charge, defined in Equation 1.1. Due to the quarks' interaction via the strong force (Section. 1.3.3) quarks cannot be seen bare, due to color confinement [5], and are only found in bound states known as hadrons.

1.3 Bosons

In the Standard Model forces between the fermions are mediated by spin-1, or vector, particles. Since forces are mediated via exchange of quanta there is the additional consequence that the force mediating particles may interact amongst themselves, in addition to the fermions. The way that the forces interact amongst themselves is

rigidly predicted within the Standard Model by group symmetries that determine how the fields which represent these forces can transform in 3+1 dimensional spacetime. These symmetries are connected to conserved quantum numbers by way of Noether's first theorem [6], which states that for every continous symmetry of a system there is a corresponding conservation law. Since the SM uses non-Abelian[1] groups to describe the symmetries of the strong force and unified electromagnetic and weak forces, interactions between the force carriers arise. Measurements of these interactions are extremely stringent tests of the assumptions and structure of the Standard Model since they directly probe the implications of these assumed symmetries.

	Strong	Weak		Electromagnetic
Carrier	g (gluon)	$W^{\pm}$	Z_0	γ (photon)
Coupling Strength	$\alpha_S \sim \frac{1}{10}$	$G_F = 1.167 \cdot 10^{-5}\text{GeV}^{-2}$		$\alpha_{EM} \sim \frac{1}{137}$
Mass	0	80.4 GeV	91.2 GeV	0

Table 1.2: The force mediating bosons of the Standard Model. Gluons, Weak gauge bosons and the photon in addition to their couplings and masses.

1.3.1 Electroweak Physics

The $SU(2)_L \times U(1)_Y$ symmetry that defines the electroweak[2] interactions is broken at low energies to yield the weak and electromagnetic forces which we are familiar with. The electroweak sector describes the interactions and symmetries between particles that carry non-zero values of the quantum number hypercharge, Y, defined as:

$$Y = 2(Q - T_3) \tag{1.1}$$

where Q is the electric charge and T_3 is third component of weak isospin. The weak force is mediated by the massive $W^{\pm}$ and Z_0 vector bosons and the electromagnetic

[1] Non-commutative, *i.e.* $AB \neq BA$

[2] The unified description of the electromagnetic and weaks forces

$$\begin{pmatrix} u \\ d \end{pmatrix}_L \quad \begin{pmatrix} \ell \\ \nu_\ell \end{pmatrix}_L \quad (u)_R \quad (d)_R \quad (\ell)_R$$

Figure 1.1: The $SU(2)_L$ structure of each generation in the Standard Model. Quarks and charged leptons having a right handed singlet component.

force is mediated by the photon, γ. The massive nature of the weak vector bosons reduces the effective range and causes the strength of their interactions to be small.

The subscript L on the $SU(2)_L$ symmetry denotes that the $SU(2)$ transformations operate on Standard Model fermions with left handed (negative) chirality, the orientation of a particle's spin to its momentum. Chirality can be defined by the projections of four component fermion fields, ψ, given in equation (1.2).

$$\begin{aligned} \psi_L &= (1-\gamma_5)\psi \quad \text{'Left handed', negative chirality spinor projection.} \\ \psi_R &= (1+\gamma_5)\psi \quad \text{'Right handed', positive chirality spinor projection.} \end{aligned} \tag{1.2}$$

This means that each generation of the Standard Model can be further organized by its left handed and right handed components. The doublet structure given in (1.1) now acquires meaning in the sense that each generation's $SU(2)_L$ doublet, for quarks and leptons individually, defines the weak interactions between left-handed particles in the doublets. Each doublet's components also exist as right handed singlets that do not transform under $SU(2)_L$ and hence do not interact with the weak force, with the sole exception of neutrinos which do not have a right handed component in the Standard Model.

The electromagnetic portion of the force is mediated only by the photon. The photon only interacts with objects that carry non-zero electric charge, defined in Equation 1.1. This implies that the photon and Z do not couple in the SM and Z + γ pairs, Zγ, may only be produced by radiation of photons and Z bosons from fermions and, to a far lesser extent, the charged weak bosons. This quality of SM photons in particular predicts the SM production rate of Zγ pairs very accurately,

making the process very sensitive to non-Standard Model physics that could add direct interactions between the Z and the photon.

1.3.2 The Higgs Boson and Electroweak Symmetry Breaking

The most theoretically rich and powerfully predictive part of the Standard Model is the electroweak theory that provides a unified framework for describing the seemingly disparate elecromagnetic and weak forces. The underlying idea is that the electromagnetic ($U(1)_{\mathrm{EM}}$[3] symmetry) and weak ($SU(2)_L$[4] symmetry) forces merge at high energies, above 100 GeV, to form a single force that is described by an $SU(2)_L \times U(1)_Y$ symmetry. The form of the force at high energies, instead of being given by the W, Z_0, and γ bosons, given by four massless fields:

$$\begin{pmatrix} W_\mu^1 \\ W_\mu^2 \end{pmatrix} \qquad \begin{pmatrix} W_\mu^3 \\ B_\mu \end{pmatrix} \tag{1.3}$$

where the W^3 and B are chargeless and the $W^{1,2}$ fields are charged. All four fields transform under rotations in $\mathrm{SU(2)_L} \times \mathrm{U(1)_Y}$, where Y is hypercharge.

The doublets, a pair of fields that transform in $SU(2)_L$, given in 1.3 mix to generate the W, Z, and photon (A_μ) in the following superpositions:

$$\begin{aligned} W_\mu^\pm &= \tfrac{1}{\sqrt{2}} \left(W_\mu^1 \mp i W_\mu^2 \right) \\ Z_\mu &= \cos\theta_{\mathrm{W}} W_\mu^3 - \sin\theta_{\mathrm{W}} B_\mu \\ A_\mu &= \sin\theta_{\mathrm{W}} W_\mu^3 + \cos\theta_{\mathrm{W}} B_\mu \end{aligned} \tag{1.4}$$

where θ_{W} is known as the weak mixing angle, an experimentally measureable quantity of the SM that determines the mass difference between the $\mathrm{W}^\pm$ and Z_0 bosons.

[3]This symmetry corresponds to invariance of magnitude of a complex scalar number under rotations in the complex plane, i.e. rotations of phase.

[4]This symmetry corresponds to invariance under rotations of complex two component vectors.

Additionally there is the Higgs field, which forms another $SU(2)$ doublet. When determining how these fields exist in the vacuum and interact with each other, i.e. by solving their equations of motion, a possible solution is one non-trivial Higgs field and its various interactions with linear superpositions of the electroweak fields. These superpositions are the Weak and Electromagnetic bosons. The interactions between the resulting Higgs field and the electroweak fields provides mass to the W and Z bosons at low energy. The process of giving masses to the weak vector bosons is known as the Higgs mechanism or Electroweak Symmetry Breaking [7].

1.3.3 Quantum Chromodynamics (QCD)

Quantum chromodynamics describes the interactions between particles that carry one of three 'color' charges. The mediator of the strong force, the massless gluon (g) carries color charge and interacts with itself, much like the triple gauge couplings between two W bosons and either a Z or a photon. Consequently, the gluon, which has eight color permutation, can self-interact. This property, along with having three charges, causes the strong force to exhibit increasing strength over longer distances, in stark contrast to the weak and electromagnetic forces. The strong force exhibits a property known as asymptotic freedom where the coupling constant, α_S, becomes small at short distances or high energies. This implies that the coupling strength changes as a function of the energy of strong interactions and that for energetic interactions we may study strong interactions in the same mathematical framework as used for electromagnetic and weak interactions. Likewise, at large distances and low energies, below 1 GeV, QCD interactions cannot be calculated using perturbation theory and rely on non-perturbative techniques for predictions.

In this low energy regime, QCD charged particles form bound states that have no net color charge called hadrons. Hadrons are divided into two major categories.

Those comprised of three quarks, such as protons, are called baryons and those of two quarks are mesons. The hadron constituents, quarks and gluons, are known generally as partons. Baryons and mesons form the largest spectrum of composite particles comprised of basic Standard Model constituents. In high energy proton collisions the transition from high energy QCD to its low energy manifestation is visible in the form of radiated gluons or ejected quarks from energetic collisions of partons. These radiated, initially high energy, particles then lose energy by creating more quarks and gluons in a process called fragmentation. Once the average energy per particle enters the low energy regime the fragmented quarks and gluons finally form hadrons in a collimated, physically observable structure known as a 'jet'. At the LHC, in particular, jet production occurs very often in association with electroweak processes and the understanding of the QCD corrections to electroweak processes is of paramount importance to properly understand the observed data.

1.4 Proton-Proton Collisions

Protons are hadrons made of of three 'valence' quarks (uud). The effects of the proton being bound together by the strong force become readily apparent when attempting to probe its substructure. The most striking feature being that if one probes a high-energy proton at short distances, one does not necessarily interact with one of the valence quarks and the interaction may even be with quarks of entirely different generations. This effect comes from the evolving substructure of the proton with energy. The proton, while remaining in a bound state generates a 'sea' of quarks, anti-quarks and gluons through gluon radiation color charged objects and pair-production of quarks and anti-quarks from gluons. This sea contribution to the structure of the proton becomes more dominant as the energy of the proton is increased. This means

that proton-proton interactions at the LHC can consist of of $q\bar{q}$, qq, qg or gg initial states and electroweak or QCD final states. The gg initial state is the most common at the LHC due to the very high energy of the protons being collided and indeed the very reason for using proton-proton collisions at the LHC since the Higgs boson should be dominantly produced through gluon collisions. In comparison, this makes using anti-protons ineffective cost-wise, given the goals of the LHC machine, since higher luminosities are more easily achievable using only proton beams.

The probabilities of various combinations of initial and final states occuring together to form an interaction as observed in nature are modeled and calculated through the theoretical framework of Quantum Field Theory (QFT). These probabilities are known as 'cross sections', denoted by the symbol σ, and are given in units of barns, 10^{-24}cm^2. Intuitively, the larger the cross section, the higher the probability of an interaction occuring in a single proton-proton collision. We may then proceed to repeat the proton-proton collisions to convert these probabilities into rates. The rate of a process is given by the total rate of proton-proton collisions resulting in any interaction, called the instantaneous luminosity '$\mathcal{L}$', and the cross section of the final state of interest (1.5).

$$\text{rate} = \frac{\mathrm{d}N}{\mathrm{d}t} = \mathcal{L}\sigma \tag{1.5}$$

Since the perturbative cross sections are calculated using the SM and the formalism of QFT, they are rigorously predicted where expected to be accurate, and serve as excellent benchmarks for the theories that predicted them. Furthermore, since the rates of various combinations of initial partons and the final states from those partons change with energy, these predictions can and should be verified across multiple energy ranges to determine the SM's accuracy. However, some cross sections such as the total proton-proton inelastic cross section [8], cannot be calculated using

perturbative techniques and are derived from non-perturbative methods or directly from data.

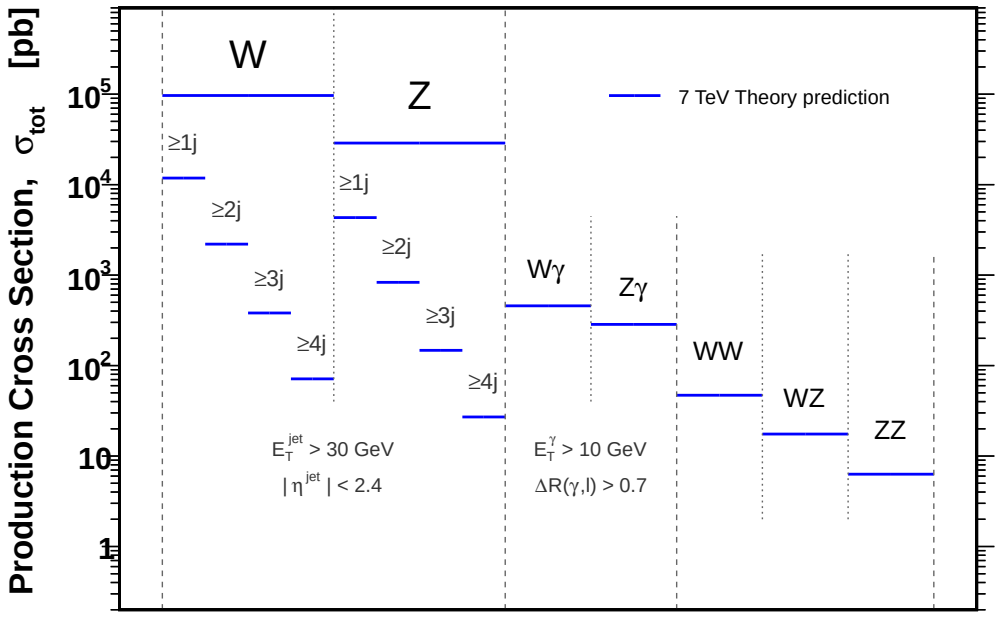

Figure 1.2: Predictions for the cross sections of various SM processes, the heirarchy of rates that depends on the bosons involved. Wγ and Zγ have larger cross sections since the photon is massless.

1.5 The Zγ Cross Section

After the weak vector bosons were discovered at CERN [9] and electroweak theory's initial predictions were validated, the quest to validate the theory to greater accuracy started. The logical continuation was to search for processes containing the signatures of two electroweak bosons, which allows for processes where the vector bosons interact with each other. According to the SM there is no interaction allowed directly between the photon and the Z, so the goal here is to see if the rate of radiation of Z bosons

in association with photons from quarks and charged leptons agrees with the SM prediction. Previous experiments at the LEP electron-positron collider at CERN and at the Tevatron proton-antiproton collider at FermiLab have measured the cross section of the neutral electroweak bosons produced in association, as will be discussed further in section 8.4.

The aim of this dissertation is to measure the cross section of the radiative process $pp \to Z(\to \ell\ell)\gamma$, where ℓ are electrons or muons, using the CMS experiment at the LHC. The cross section and distribution of observed photons can then be used to infer the presence of non-SM couplings between the Z and the photon. The presence of colored partons in the initial state at the LHC requires the understanding of additional QCD radiation and the associated correction to the Zγ cross section must be taken into account when analyzing the data and comparing to theory.

The predictions of the Zγ cross section calculated using perturbative electroweak theory and corresponding QCD corrections are necessary for performing tests of the standard model. The Zγ cross section is sensitive to the addition of non-standard couplings of the Z and the photon [10] and can be used as a precision tool for the understanding of the SM.

Chapter 2

Zγ Phenomenology

Zγ production provides a useful test of the SM; however, the requirement of two electroweak bosons in the final state and the Z boson decaying leptonically greatly reduces the cross section, via branching fraction, and increases the effect of possible backgrounds imitating photons. The jet-rich nature of collisions at the LHC requires the use of corrections from perturbative QCD (pQCD), since the larger phase space coming from additional final state configurations alters both the predicted cross sections from electroweak theory and additional production processes from anomalous triple gauge couplings, 'aTGCs' [11]. An outline of the general theoretical framework for describing proton-proton collisions and the subsequent need for pQCD corrections to electroweak, 'EWK', predictions will be presented in Section 2.1. Section 2.2 will describe in further detail the Zγ production mechanisms, including contributions that are next-to-leading,'NLO', in the strong coupling constant α_S. The production of the Zγ final state by way of anomalous triple gauge couplings will be discussed in Section 2.3 and the observables sensitive to the aTGCs in Section 2.4.

2.1 Proton Collisions at the LHC

As noted earlier, the proton has a dynamic substructure that evolves with energy and is non-perturbative. However, it is still possible to perturbatively calculate processes initiated by quark and gluon initial states by factorizing the perturbative and non-perturbative parts of the cross section. This is achieved by averaging over all possible initial states for a process and weighting this average by the probability of that initial state to occur with the requisite energy. These weights are provided by experimentally derived functions known as parton distribution functions (PDFs). These functions, $f_i(x, Q^2)$, define the probability of finding a parton of some given type i with momentum fraction x at momentum transfer Q^2 of the process[1]. The

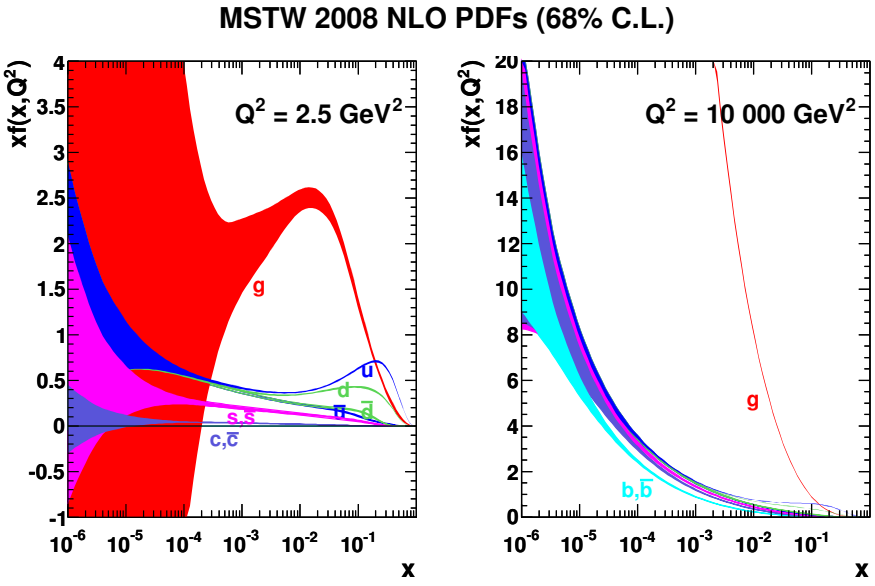

Figure 2.1: The parton distribution functions for the quark and gluon contituents of a proton at two different values of momentum transfer. The u and d components are dominated by valence quarks at high x while s, c, b, and g are more prevalent at low x. The gluon fraction at low x increases by orders of magnitude at large momentum transfers. [12]

[1] Q^2 is a measure of the energy at which the reaction being studied takes place.

PDFs are determined empirically since there is not a valid predictive technique for using QCD that describes the structure of hadrons. All PDFs used for predictions at the Large Hadron Collider were measured at experiments on previous high energy hadron colliders such as the Tevatron at Fermilab and the hadron-electron colliders such as HERA at DESY, with additional inputs from the study of tau decays [13] and quarkonium measurements [14].

The perturbative part of the high energy collision process can be calculated through the formalism of Quantum Field Theory by summing over all possible elementary processes contributing to the observed final state. For example, leading order di-jet production at the LHC consists of a number of input processes, with multiple parton types as initial states. Since the probabilities of certain initial states are factorized out, the cross section can be written in terms of general kinematic dependencies and coupling constants.

$$\hat{\sigma}_{pp',ff'}(\hat{s},\hat{t},\hat{u}) = \begin{cases} \frac{4\pi\alpha_s^2}{9\hat{s}^2}\left[\frac{\hat{s}^2+\hat{u}^2}{\hat{t}^2}\right] & pp' = qq', ff' = qq' \\ \frac{4\pi\alpha_s^2}{9\hat{s}^2}\left[\frac{\hat{s}^2+\hat{u}^2}{\hat{t}^2} + \frac{\hat{t}^2+\hat{u}^2}{\hat{s}^2} - \frac{2}{3}\frac{\hat{u}^2}{\hat{s}\hat{t}}\right] & pp' = q\bar{q}, ff' = q\bar{q} \\ \frac{4\pi\alpha_s^2}{9\hat{s}^2}\left[\frac{\hat{u}^2+\hat{s}^2}{\hat{t}^2} + \frac{\hat{t}^2+\hat{s}^2}{\hat{u}^2} - \frac{2}{3}\frac{\hat{s}^2}{\hat{u}\hat{t}}\right] & pp' = qq, ff' = qq \\ \frac{32\pi\alpha_s^2}{27\hat{s}^2}\left[\frac{\hat{u}}{\hat{t}} + \frac{\hat{t}}{\hat{u}} - \frac{9}{4}\frac{\hat{t}^2+\hat{u}^2}{\hat{s}^2}\right] & pp' = q\bar{q}, ff' = gg \\ \frac{\pi\alpha_s^2}{6\hat{s}^2}\left[\frac{\hat{u}}{\hat{t}} + \frac{\hat{t}}{\hat{u}} - \frac{9}{4}\frac{\hat{t}^2+\hat{u}^2}{\hat{s}^2}\right] & pp' = gg, ff' = q\bar{q} \\ \frac{4\pi\alpha_s^2}{9\hat{s}^2}\left[-\frac{\hat{u}}{\hat{s}} - \frac{\hat{s}}{\hat{u}} + \frac{9}{4}\frac{\hat{s}^2+\hat{u}^2}{\hat{t}^2}\right] & pp' = qg, ff' = qg \\ \frac{9\pi\alpha_s^2}{2\hat{s}^2}\left[3 - \frac{\hat{t}\hat{u}}{\hat{s}^2} - \frac{\hat{s}\hat{u}}{\hat{t}^2} - \frac{\hat{s}\hat{t}}{\hat{u}^2}\right] & pp' = gg, ff' = gg \end{cases} \quad (2.1)$$

Equation 2.1 [15] is an example of a typical parton level matrix element, in this case, dijet production at leading order in perturbative QCD. pp' and ff' represent the incoming and outgoing particles, indicating the various initial and final states involved. Due to the various initial states, the contribution from each subprocess changes as a function of the proton's energy, thus causing the fractions of observed final states to change. This change in the 'dominance' of various final states plays a

large role at the LHC due to the large dynamic range of Q^2, the momentum transfer in the collision.[2]

The net result is a general expression for the cross section of a generic final state produced in a proton-proton collision:

$$\sigma(pp \to \mathrm{P} + X) = \frac{1}{3}\sum_{p,p'} \int \mathrm{d}x_1 \mathrm{d}x_2 f_1(x_1, Q^2) f_2(x_2, Q^2) \hat{\sigma}_{\mathrm{P}}(\hat{s}, \hat{t}, \hat{u}), \tag{2.2}$$

with $f_i^{1,2}$ the parton distribution functions of the two colliding protons and $\hat{\sigma}_{\mathrm{ME}}(\hat{s}, \hat{t}, \hat{u})$ the parton-level cross section for some matrix element. The process 'P' is determined by a perturbative matrix element. The factorization used to separate the proton's structure from the interaction being studied allows for the perturbative treatment of the considered process in terms of Feynman diagrams.

2.2 Standard Model Zγ Production

The Z boson may decay to any kinematically accessible quark-antiquark or lepton-antilepton pair. However, the Z couples to leptons and quarks with slightly different strengths since leptons and quarks carry different electric and weak charges.

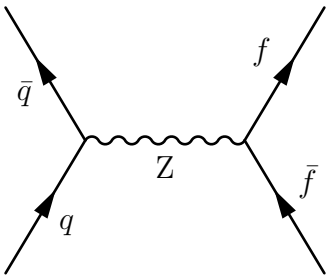

Figure 2.2: SM Z boson production and decay at a hadron collider. Only quarks are present in the initial state, but the final state can be quarks or leptons.

There are 5 possible quark pairs to decay into, each with 3 color combinations, and there are 6 possible lepton choices. The result is that the probability, or branching

[2]Two orders of magnitude, for inclusive Z production, three for dijet production.

ratio, of a Z decaying to quarks is roughly 5/7 while to leptons is 2/7, to within corrections from electroweak couplings. The fraction of Zs decaying to charged leptons or neutrinos is determined by weak charge $T_3 - Q \sin^2 \theta_{\mathrm{W}}$, where θ_{W} is the weak mixing angle and $\sin^2 \theta_{\mathrm{W}} \approx 0.2397 \pm 0.0013$ and T_3 is the third component of weak isospin. Since neutrinos do not have electric charge and their coupling is not damped by the weak mixing angle, the Z will decay to neutrinos with probability $\sim$2/3 and then to the charged leptons with probability 1/3. Amongst each neutrino and charge lepton type the Z decays nearly democratically, to within corrections from lepton mass. The measured branching ratios to electrons and muons individually are 3.36%. The electron and muon are the most easily detectable and reconstructable decay products of the Z. The leptons' masses are negligible in comparison to the Z causing the mass of the Z to become the momentum of the leptons, leaving the striking signature of two energetic leptons in a particle physics detector. This clean signature makes associated Z boson production an excellent handle for studying particles that are difficult to identify on their own among the plethora of background particles produced at hadron colliders.

The photon couples to the electric charge of other particles. In the case of Z production at hadron colliders, the initial state almost always contains a quark and this quark can radiate photons. This process is called initial state radiation, or ISR. Likewise, for the decay of the Z, additional photons can be emitted from the charged daughter particles through final state radiation, FSR. Photons are produced in abundance at the LHC by these radiative processes, making them a prominent background to non-radiative sources of photons.

Since the Z and photon are pair-produced in the SM only by radiative processes, there are only two major contributing Feynman diagrams. In the case of the Z decaying to two charged leptons there is the additional FSR contribution to the final

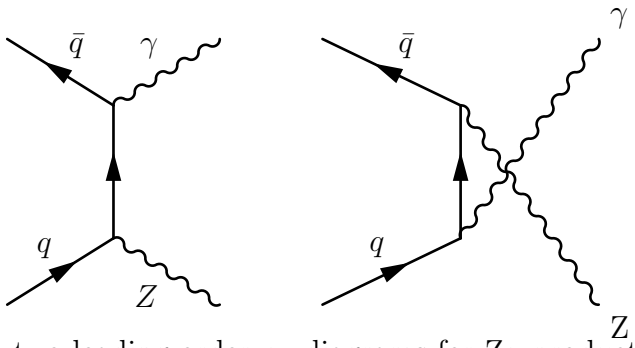

Figure 2.3: The two leading order α_s diagrams for Zγ production in the SM.

state of two leptons and a photon. For Zγ, in stark contrast to Wγ [16, 17], there is

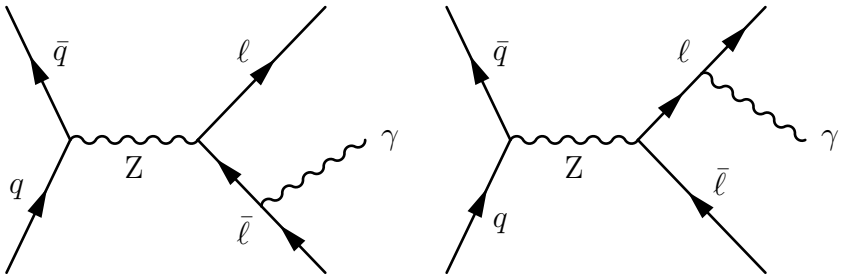

Figure 2.4: The leading order α_s diagrams for FSR Zγ production in the SM.

no interference between the initial and final radiation processes, since for the former the TGC is a forbidden process in the SM. This means that it is relatively easy to separate the FSR and ISR contributions and exploit them for different purposes. The SM FSR process is primarily useful for determining the response of CMS calorimetry to photons, since the three body mass is kinematically constrained to the observed Z invariant mass distribution. ISR production, as stated previously, is precisely predicted within the perturbative framework of the standard model and constitutes the primary background to the aTGC searches. In particular, ISR photons produced in association with Zs are the primary background to the possible neutral aTGC signal.

At the LHC at least one of the incoming partons is likely to be energetic. This forces the probability to emit a jet to be very large, especially at low jet energies, and consequently makes higher, next-to-leading (NLO), order α_s effects on the SM Zγ

cross section more important [18]. Additionally, the large gluon fraction of protons at the LHC causes gluon-quark initiated processes to be enhanced, which also contribute at NLO in Zγ production.

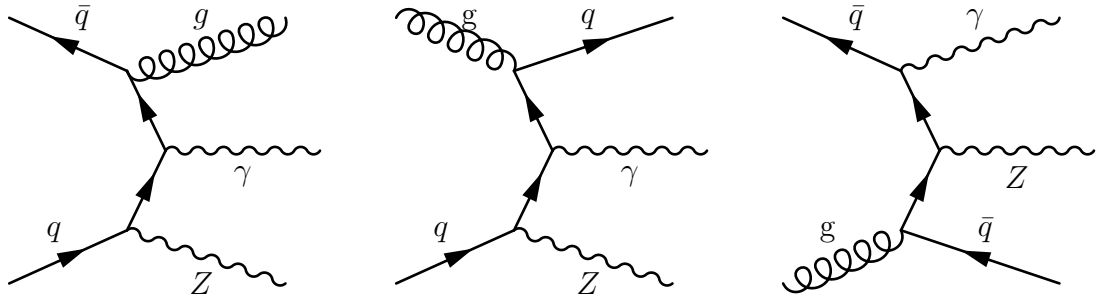

Figure 2.5: The unique real emission diagrams for ISR Zγ. There are additional diagrams resulting from the permutation and crossings of the Z, γ, and final state parton.

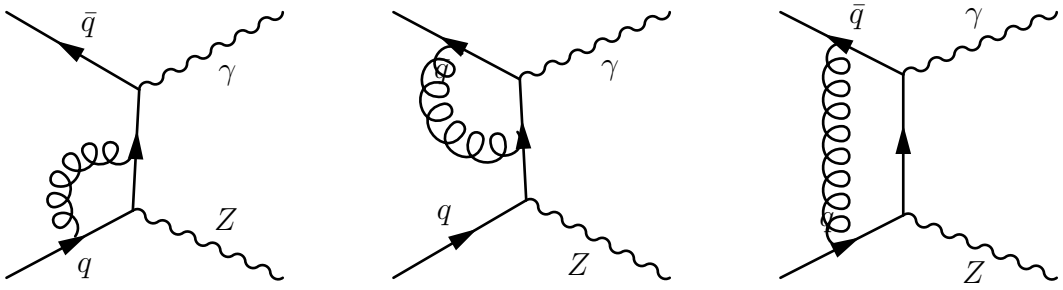

Figure 2.6: The loop diagrams for ISR Zγ. The same initial states apply to the crossed graph in Figure 2.3

The calculation of NLO corrections in quantum field theory requires the introduction of radiative processes which, on their own, contain unphysical singularities when the additional radiation becomes too low energy or collinear to the particle that emitted it. These unphysical singularities are removed when accounting for the interference between the leading order process and so-called 'loop' diagrams, which introduce counter-terms to the singularities in the radiative processes [15]. The calculation of the NLO corrections to the ISR processes is theoretically difficult since the photon may be emitted from final state 'fragmentation photons' or initial state

quarks. The fragmentation photons may also have a non-perturbative part when the photon is very close to the object that radiates or when photon radiation from gluons is involved. This significantly complicates the calculation with respect to the

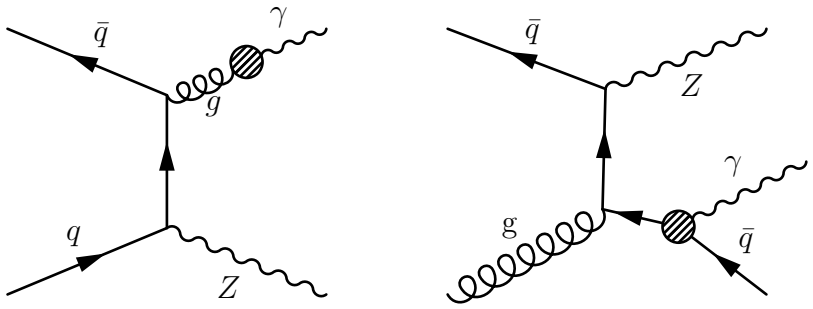

Figure 2.7: The photon fragmentation contribution to Zγ production at NLO. In the gluon contribution (left) there is additional hadronic radiation from the non-perturbative process to conserve color flow. The quark contribution also contains non-perturbative effects due to collinearity of the photon with the quark.

singularities introduced at NLO in α_s since it is hard to treat the photon as both radiation and a product of the matrix element in a consistent way. There are some Monte Carlo programs which calculate this contribution, but none are interfaced to parton showers [11, 19]. The problem of correctly dealing with photon fragmentation is the primary reason for the slow advancement of NLO α_s accurate calculation of processes with photons in the final state towards NLO accurate event generation [20].

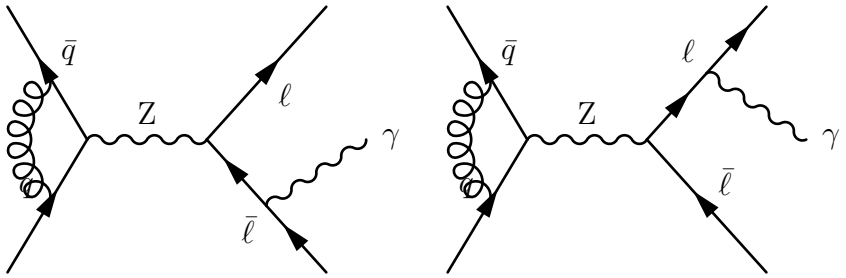

Figure 2.8: The loop diagrams for FSR Zγ.

The FSR portion of the process is theoretically more accessible as it is merely

Z production with an extra complication in the decay of the Z. The NLO and NNLO α_s corrections to Z boson production are well understood and being improved upon [21, 22]. However, since it is tied to the ISR process as they share the same

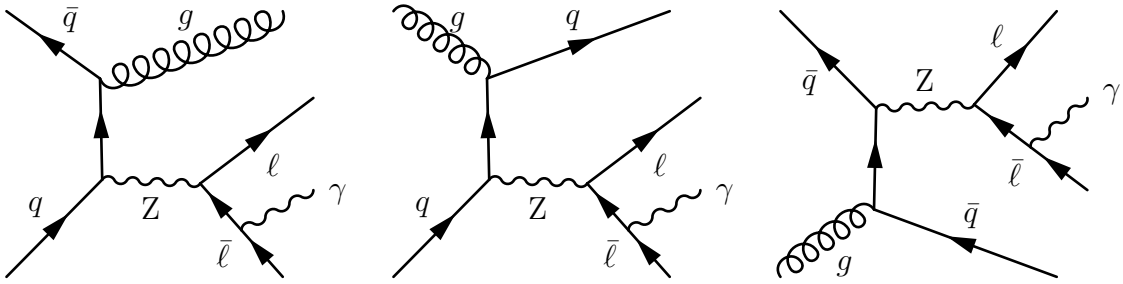

Figure 2.9: The real emission diagrams for FSR Zγ.

final state, the FSR contribution to Zγ production cannot benefit from these more recent theoretical improvements. Anomalous production of Zγ, which is kinematically similar to FSR[3], cannot gain from an improved theoretical understanding of these kinematically simpler processes for the same reason. The NLO, order α_s, contributions result in more energetic photons being produced. The understanding of and ability to simulate these contributions in SM and anomalous production at hadron colliders are extremely important for probing the standard model through the measurement of anomalous couplings. Though a number of complications have been presented in the context of the theoretical calculation of the Zγ final state, accurate cross section calculations do exist and the majority of difficulties arise in the context of event generation.

2.2.1 Z+Jets as a Background to Zγ

At the LHC, the Z boson is most often produced in association with jets, in comparison to photons, as α_s is roughly an order of magnitude larger than α_{EM}. The evolution of these jets is described by both perturbative and non-perturbative processes. The

[3]The photon is not emitted by the initial state quarks.

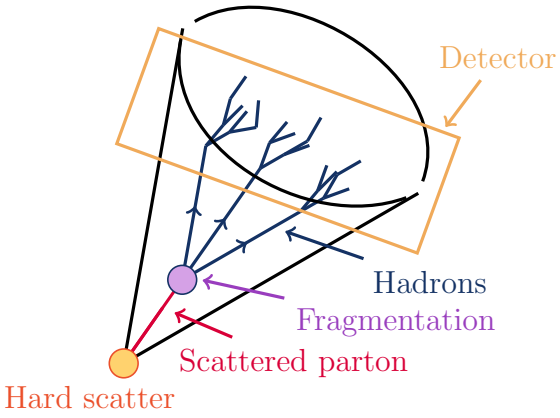

Figure 2.10: The stages of jet evolution, starting from the perturbatively based scattering and ending with the nonperturbative hadronization.

last step in these processes describing the jet evolution is known as hadronization and describes the non-perturbative formation of hadrons from low energy partons in jets. The final states from hadronization can fluctuate significantly from jet-to-jet and there are a variety of final-state hadrons that decay electromagnetically into two or more photons, for instance π^0s. Thus, it is likely for a jet to produce a final state that is primarily composed of secondary photons from the decay of hadrons. These collections of photons coming from jets whose hadrons decay primarily electromagnetically are similar to promptly produced real photons in terms of their appearance in a detector. Due to the much larger cross section of Z+Jets production and the non-zero probability of these jets to hadronize into photons, Z+Jets serves as the primary background to SM Zγ production at hadron colliders.

2.3 Anomalous Zγ Production

The theoretical understanding of neutral anomalous triple gauge couplings has been well described for years [10, 11, 23]. The chosen symmetries of the standard model

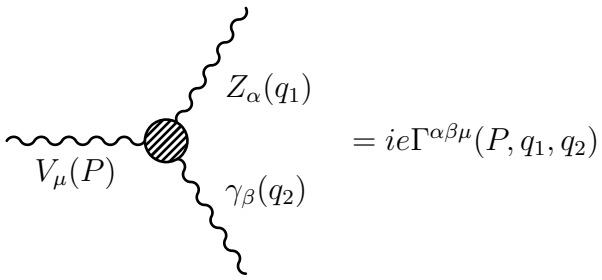

Figure 2.11: The general form of the ZγV, vertex. V=γ,Z

are not completely fundamental requirements and the SM can be extended by adding new terms that still obey more basic properties, like gauge and Lorentz invariance. In the case of the Zγ anomalous couplings there are 4 couplings both for Z→Zγ and γ →Zγ that are allowed by gauge and Lorentz invariance but not by the SU(2)×U(1) structure of the standard model [10]. The vertex function given in Figure 2.12 has

$$\begin{aligned}\Gamma^{\alpha\beta\mu}_{\mathrm{Z}\gamma\mathrm{Z}}(q_1, q_2, P) &= \frac{P^2 - q_1^2}{m_{\mathrm{Z}}^2}\Bigg[\; h_1^{\mathrm{Z}}(q_2^\mu g^{\alpha\beta} - q_2^\alpha g^{\mu\beta}) \\ &\quad + \frac{h_2^{\mathrm{Z}}}{m_{\mathrm{Z}}^2} P^\alpha \Big[(P\cdot q_2) g^{\mu\beta} - q_2^\mu P^\beta\Big] \\ &\quad + h_3^{\mathrm{Z}} \epsilon^{\mu\alpha\beta\rho} q_{2\rho} \\ &\quad + \frac{h_4^{\mathrm{Z}}}{m_{\mathrm{Z}}^2} P^\alpha \epsilon^{\mu\beta\rho\sigma} P_\rho q_{2\sigma}\Bigg]\end{aligned}$$

Figure 2.12: The ZγZ, vertex function with the four couplings allowed by gauge and lorentz invariance.

the form for the ZγZ vertex and the forms of all four allowed couplings. The vertex for Zγγ has almost exactly the same structure as the ZγZ vertex, except for labelings and the following substitution in the prefactor due to Bose symmetry:

$$\frac{P^2 - q_1^2}{m_{\mathrm{Z}}^2} \to \frac{P^2}{m_{\mathrm{Z}}^2} \qquad \text{and} \qquad h_{1-4}^{\mathrm{Z}} \to h_{1-4}^{\gamma} \tag{2.3}$$

Due to Yang's theorem [24], all of these couplings vanish at leading order in the SM and when the incoming particles are on shell[4]. For both γ and Z initiated couplings, h^1 and h^2 are CP-odd while h^3 and h^4 are CP-even, leading to slightly different kinematic dependencies for each coupling. The terms multiplying $h^{1,3}$ scale as the center of mass energy of the incoming parton, $\hat{s}$, while $h^{2,4}$ scale as $\hat{s} \cdot q_2^2$, resulting in more significant variations in the theoretical cross section when attempting to determine $h^{2,4}$ using experimental data.

Finally, none of the couplings as defined preserve unitarity at high energies since they grow without bound as a function of the incoming vector boson's energy. Motivations for a form of regularization of the couplings are given in [11]. The result being the use of an ad-hoc 'form-factor' that supresses the coupling at very high energies. The general form of the commonly used dipole form factor is given in Equation 2.4. The dipole form-factor suppresses the divergent behavior of neutral aTGCs at high energy, above the cutoff scale Λ.

$$f(\hat{s}) = \frac{1}{(1 + \hat{s}/\Lambda^2)^n} \tag{2.4}$$

This simulates the effect of resolving new physics at some cutoff scale[5] which is above the kinematic reach of existing hadron colliders[6]. However, while these form factors do regularize the contributions of aTGCs at arbitrarily high energies, they are not entirely necessary when searching for new physics using diboson production. One can take as an example the attempt to compare limits on new physics at different hadron colliders where one hadron collider uses a cutoff scale that is well below the other's kinematic reach [23]. In order to compare results, the collider with higher

[4] i.e. when the photon is massless or the Z is exactly 91.18 GeV

[5] or 'Scale of New Physics', 'Mass Scale'. Mathematically, a non-infinite integration bound.

[6] As a rule of thumb, the kinematic reach of a proton-proton collider is half the center of mass energy of the beam and for a proton-antiproton collider it is about 2/3 the center of mass energy. This difference comes from the probing valence (anti)quarks in the (anti)protons versus probing valence quarks in one proton and sea quarks in the other.

kinematic reach needs to use a form factor with cutoff scale that is lower. This leads to the unphysical scenario where the higher energy machine would have seen this new physics the lower energy collider was probing for, making the form factor merely an arbitrary limitation on the higher energy machine's ability to detect new physics. As such, experimentally determined bounds of the values of aTGCs have also been presented without using a form factor.

2.4 Observables Sensitive to aTGCs

Anomalous triple gauge couplings enhance or generate entirely new coupling structures in observed physics processes. Thus, it is important to understand these new structures in terms of the shapes and correlations they induce on the physical observables. In the case of aTGCs the new couplings grow as the center of mass energy of the incoming partons, $\hat{s}$, and it is assumed that the observed vector boson pair is the decay product of some parent vector particle. These two properties lead to striking changes in the decay angle and p_T distributions of the final state bosons in comparison to the standard model expectations.

Since the anomalous couplings grow as some function of $\hat{s}$ there is a large bias towards higher photon p_T in the observed diboson final state when the aTGCs deviate from their standard model predictions. This bias is driven by the convolution of the much larger parton-level cross section with the proton's parton distribution function, which naturally vanishes and more energetic, and less probable, initial states are required to produce a final state. An excess in Zγ yield coming from an aTGC would be detected at high photon p_T and would come from a massive initial state. The understanding of the standard model photon p_T shape is important, especially for small aTGCS. An accurate description of the SM p_{T} distribution is achieved through

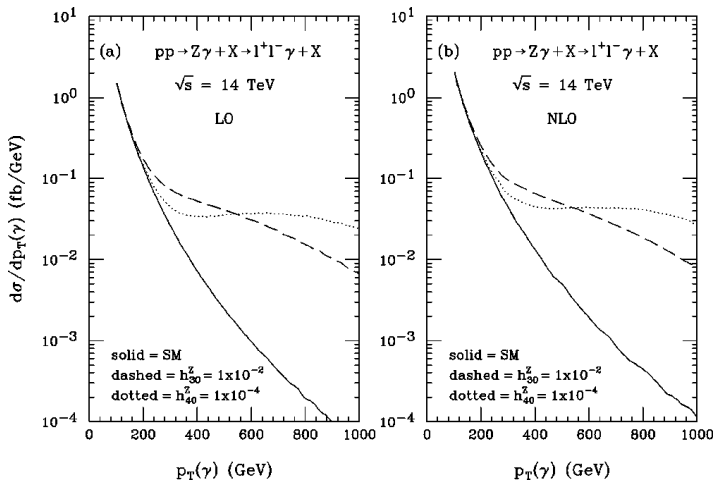

Figure 2.13: The change in the photon p_T distribution coming from h_3 and h_4 type anomalous couplings. The standard model is shown for comparison.

the use of NLO differential cross section calculations, which account for the larger available phase space available at high photon p_T when an extra jet is present in the interaction [11, 19, 25–28]. These programs also calculate the NLO α_s corrections to the aTGC production, which are however quite small due to the dominating leading order effect of the aTGCs. In Figure 2.13 the shape differences in the photon p_T distribution coming from NLO effects and various strengths and types of aTGCs are shown.

A more subtle effect coming from the presence of aTGCs is the change in the distribution of the decay angles θ^*_γ and θ^*_ℓ. Here θ^*_γ describes the angle at which the photon is emitted in the rest frame of the Zγ system with respect to the momentum of the Zγ system in the lab frame. The angle θ^*_ℓ is the equivalent for leptons coming from the decay of the Z boson. In the SM the Z and photon are never produced at the same interaction vertex since Zγ interaction is not allowed, and consequently their spins are decorrelated. Therefore the distribution of θ^*_γ is flat, since there is no preferential direction of photon spin with respect to the Zγ momentum and the distribution of θ^*_ℓ

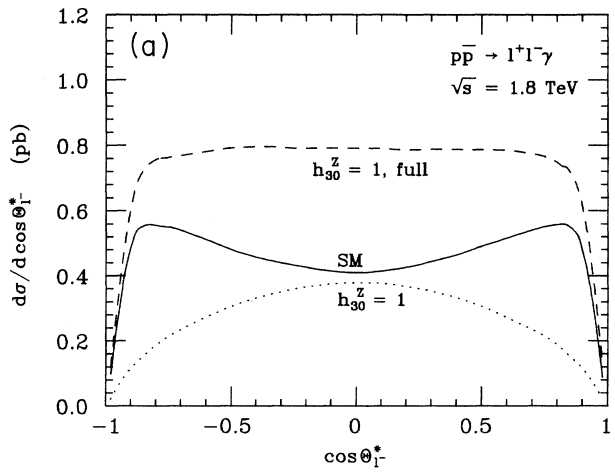

Figure 2.14: Change in the Z boson spin alignment resulting from aTGCs.

is exactly that of Z bosons produced in the SM. For aTGCs, these distributions change to reflect the vector nature of the parent particle of the Z and photon in the final state. Specfically, θ^*_γ has a distribution such that $d\sigma/d\cos\theta^*_\gamma \sim 1 + \cos^2\theta^*_\gamma$, since the initial state photons and Zs involved in the aTGC coupling have primarily transverse polarization. In contrast, angle of θ^*_ℓ will be distributed as $d\sigma/d\cos\theta^*_\gamma \sim 1 - \cos^2\theta^*_\gamma$, or 'longitudinally' polarized [10, 23]. This effect is caused by the final state photon being on shell, so the photon can only be transversely polarized [15]. Consequently, the longitudinal mode of the Z boson becomes enhanced, since the total spin of the final state must be that of the transversely polarized initial state, in the case of aTGCs. Furthermore, since the CP conserving aTGCs mix with the standard model final states there are angular correlations linear in the aTGCs, providing information on the sign of the aTGC. This information is completely missing when looking only at the photon p_T distribution, which effectively integrates over these correlations [29]. In this thesis, a p_{T} based aTGC analysis is used to set limits on anomalous triple gauge couplings.

Chapter 3

Experimental Setup

The Large Hadron Collider [30] (LHC) has been operating with high efficiency and uptime for two years [31]. The center of mass energies achieved by the LHC, 7 TeV and more recently 8 TeV, have allowed unprecedented kinematic reach in tests of the Standard Model and searches for new physics beyond. The Compact Muon Solenoid detector (CMS) [32] has operated concurrently with the LHC, collecting data from the collisions produced by the LHC in order to make these measurements.

3.1 The Large Hadron Collider

CERN's Large Hadron Collider (LHC) [30] and its experiments: CMS, ATLAS, LHCb, and ALICE [32–35] represent the culmination of years of dedicated effort by accelerator and particle physicists towards the understanding of our universe on the smallest of distance scales. The LHC accelerator complex is located in Switzerland and France, northwest of Geneva, Switzerland. The LHC made use of the pre-existing tunnel from the LEP accelerator which had been decommisioned to make way for the LHC.

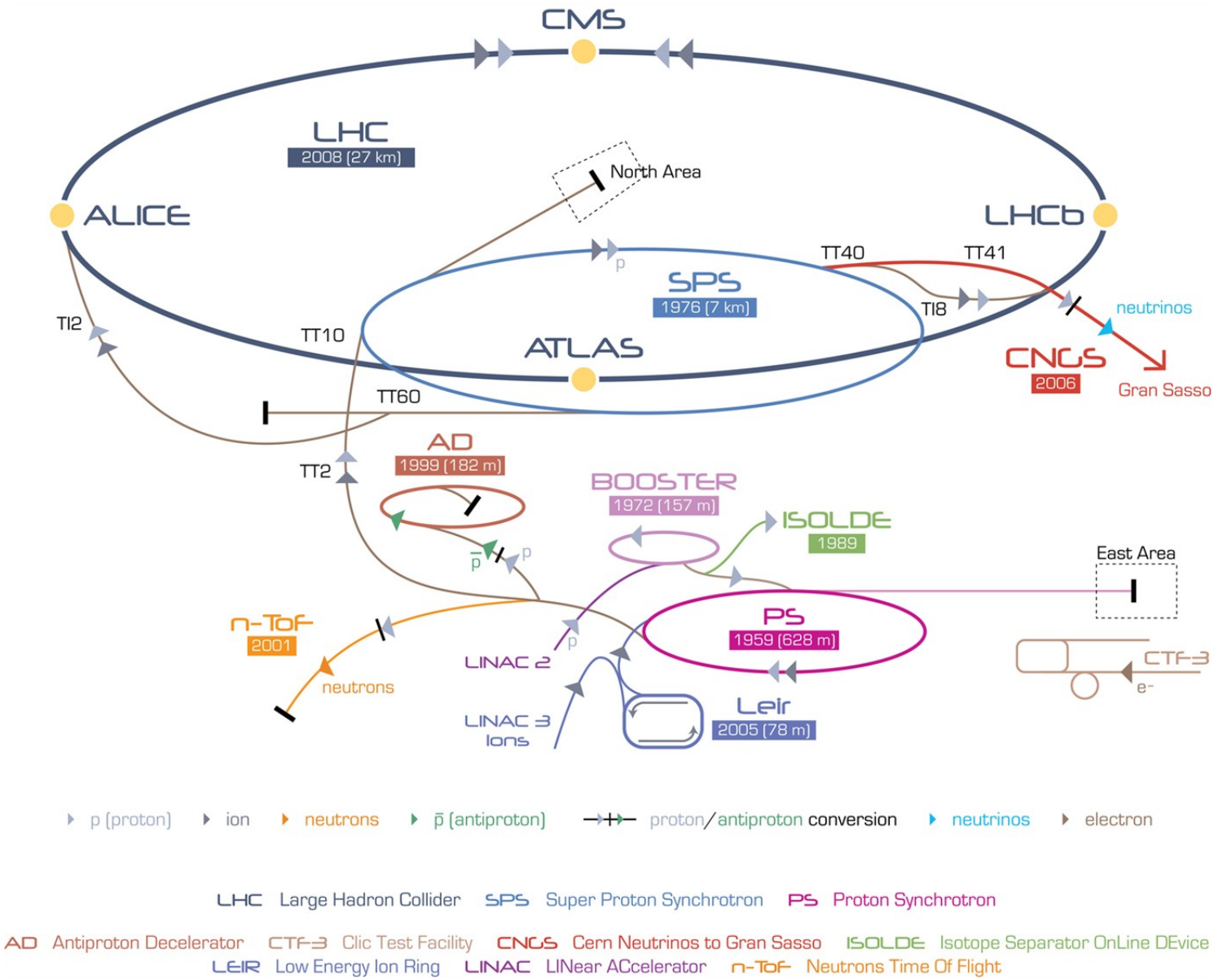

Figure 3.1: The layout and interconnections of the CERN accelerator complex. The LHC is the last stage in a multi-level injector chain starting with linear accelerators. [36]

Unlike LEP which was an electron-positron collider, the LHC is a proton-proton collider. The reasoning behind this choice being that protons lose less energy as they accelerate since they are more massive, giving a higher energy reach to the collider. This choice is made a necessity when considering the LHC's design energy of 7 TeV per beam. If the LHC were an electron-positron collider instead, the leptons would lose a factor of 11×10^{12} more energy than a proton for each orbit of the ring, making acceleration of electrons impossible with this energy [37, 38].

Another design decision was the choice to collide protons instead of protons and antiprotons and is motivated by two reasons. First, achieving large bunch populations is straightforward with proton beams in terms of generating protons, while achieving larger bunch populations of antiprotons is expensive and requires dedicated machinery. Second, with the primary goal of the LHC being to study electroweak symmetry breaking the benefits of using anti-protons are small as the Higgs boson is produced primarily through gluon fusion in high-energy proton-(anti)proton and the gluon PDFs of protons and anti-protons are the same. Therefore, since it more cost effective and easier to provide higher luminosities with proton-proton collisions and that they yield the same physics potential, LHC was designed as a symmetric collider.

Due to issues with commissioning the superconducting magnets for the LHC and, in particular, the protection system for those magnets, the LHC presently operates at energies of up to 3.5 TeV and 4 TeV per beam in 2011 and 2012, respectively. While the per-beam-energy is lower than the design energy, it still provides more than 3.5-4 times the kinematic reach of previous hadron colliders[1]. This increase in energy reach makes the LHC a powerful tool for probing for new physics and testing the Standard Model.

[1]The LHC will make progress towards achieving its design energy of 7 TeV per beam during the long shutdown starting in 2013.

As depicted in Figure 3.1, the LHC is the last accelerator in a complex chain of accelerators. Each of of these accelerators provide some experimental functionality in addition to providing beam for the LHC. The linear accelerators (linac) Linac2 provides protons at an energy of 50 MeV to the Proton Syncrotron Booster (PSB). The radio frequency, RF, techniques used for accelerating and bunching the proton or ion beams in the linac results in very long bunches compared to what is needed by the LHC's 25 nanosecond bunch spacing. In order to achieve the requisite bunch length for the LHC, the bunches from the linacs are accelerated and simultaneously split in the boosters, with the PSB splitting the input bunches into groups of four bunches and accelerating them to 1.4 GeV. The booster then feeds into the Proton Synchrotron (PS) where the bunches are twice split in two, accelerated to 26 GeV, and then injected into the Super Proton Syncrotron (SPS). In the SPS, the bunches are accelerated to 450 GeV and then injected into the LHC. Once in the LHC, the bunched charged particles are captured by its 400 MHz radio frequency (RF) acceleration system and contained in 2.5 ns wide RF 'buckets' that are organized with 25ns gaps between them. In 2011 LHC running, every other RF bucket contains a proton bunch, resulting in a bunch spacing of 50ns. The design specifications of the LHC have consecutive RF buckets filled, resulting in 25 ns bunch spacing. The standard LHC machine clock is 40.08 MHz, the LHC RF system runs at a higher frequency to achieve small bunch lengths, keeping collision events well contained within the LHC experiments and increasing luminosity. Once the beams are captured and found to be stable, they are accelerated to their collision energies and made to collide.

The LHC machine and its experiments made extensive use of the pre-existing tunnel dug for the LEP collider. This created design challenges for the LHC, specifically in terms of the size and power of magnets needed to direct the LHC's proton beams. Considering this need, along with that fact the same magnetic field cannot used to

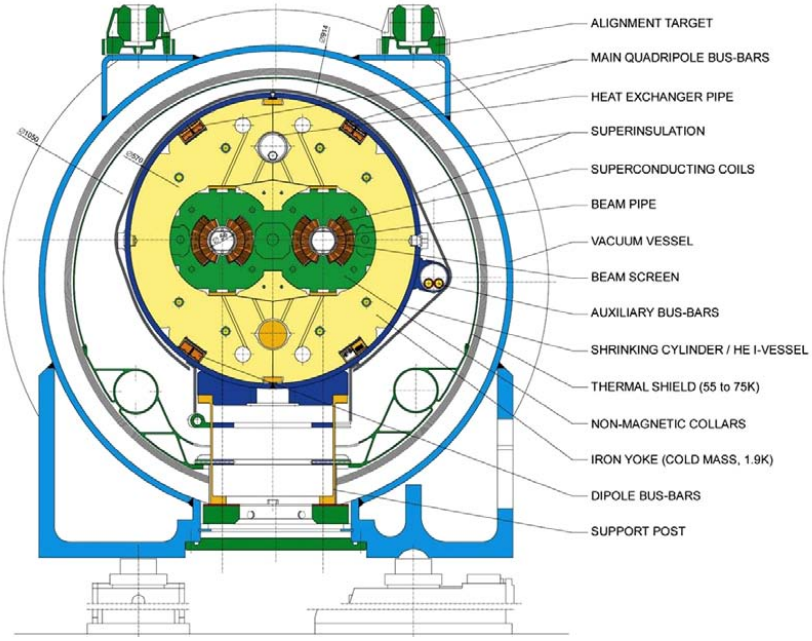

Figure 3.2: A schematic view of the construction of an LHC main dipole. All components within the iron yoke (yellow shaded area) are cooled to a temperature of 1.9K.

bend the counter circulating proton beams in the same direction, the main bending magnets of the LHC are dual bore superconducting magnets with opposing field directions in each bore, as shown in Figure 3.2. The use of superconductors to carry the current used for producing the magnetic fields is necessary since at the design energy of 7 TeV per beam a current of 11850A is required to achieve the 8.33 T field for adequate deflection in the proton beam's path. Normal conducting current leads and magnetic coils would make the design specifications impossible to achieve. The other magnets in the LHC follow a similar dual bore design but have different field configurations to meet various needs of controlling the LHC beams, such and beam focusing and energy dispersion management.

3.1.1 The Luminosity Frontier

The LHC also represents a significant increase in instantaneous luminosity, $\frac{\mathrm{d}\mathcal{L}}{\mathrm{d}t}$, compared to previous hadron colliders like the Tevatron. This quality is very important in the search for standard model and possible beyond standard model physics since it directly influences the rate at which these events happen as demonstrated in equation 3.1.

$$\frac{\mathrm{d}N}{\mathrm{d}t} = \frac{\mathrm{d}\mathcal{L}}{\mathrm{d}t}\sigma_{\mathrm{event}} \tag{3.1}$$

During the 7 TeV run in 2011, the LHC achieved a maximum instantaneous luminosity of $3.6{\times}10^{33}\mathrm{cm}^{-2}\mathrm{s}^{-1}$ [39], nearly an order of magnitude higher than the tevatron's record luminosity of $4.3{\times}10^{32}\mathrm{cm}^{-2}\mathrm{s}^{-1}$ [40].

The instantaneous luminosity delivered by a collider can be calculated from equation 3.2.

$$\mathcal{L} = \frac{N_b^2 n_b f_{\mathrm{rev}} \gamma_r}{4\pi\varepsilon_n \beta^*}\mathcal{F}(\vartheta) \tag{3.2}$$

The numerator of this equation defines rate at which protons enter an interaction region: N_b is the number of protons in an RF bucket, or a 'bunch', n_b is the number of colliding bunches at the interaction point, $f_{\mathrm{rev}} = 11.8$ kHz the frequency at which a proton bunch orbits the LHC when accelerated to 3.5 TeV, and γ_r is the relativistic gamma factor, $E_p/m_p = 3730$. The denominator is the tranverse geometrical cross section of the luminous region at the interaction point: ε_n is the normalized emittance, a measure of how quickly particles are leaving a bunch and thus it's transverse width, β^* is a measure of the betatron oscillation envelope at the interaction point and can be thought of as a focal length. Finally, there is one more relativistic correction factor, $\mathcal{F}$, defined in equation 3.3 that determines the reduction in the luminosity in the case that the bunches are not colliding head on, *i.e.* a non-zero 'crossing-angle'.

$$\mathcal{F}(\vartheta) = \sqrt{1 + \left(\frac{\vartheta\sigma_z}{2\sigma^*}\right)^2} \tag{3.3}$$

Here, ϑ is the crossing angle itself, σ_z is the lab frame bunch length and σ^* is the bunch's transverse width in the lab frame.

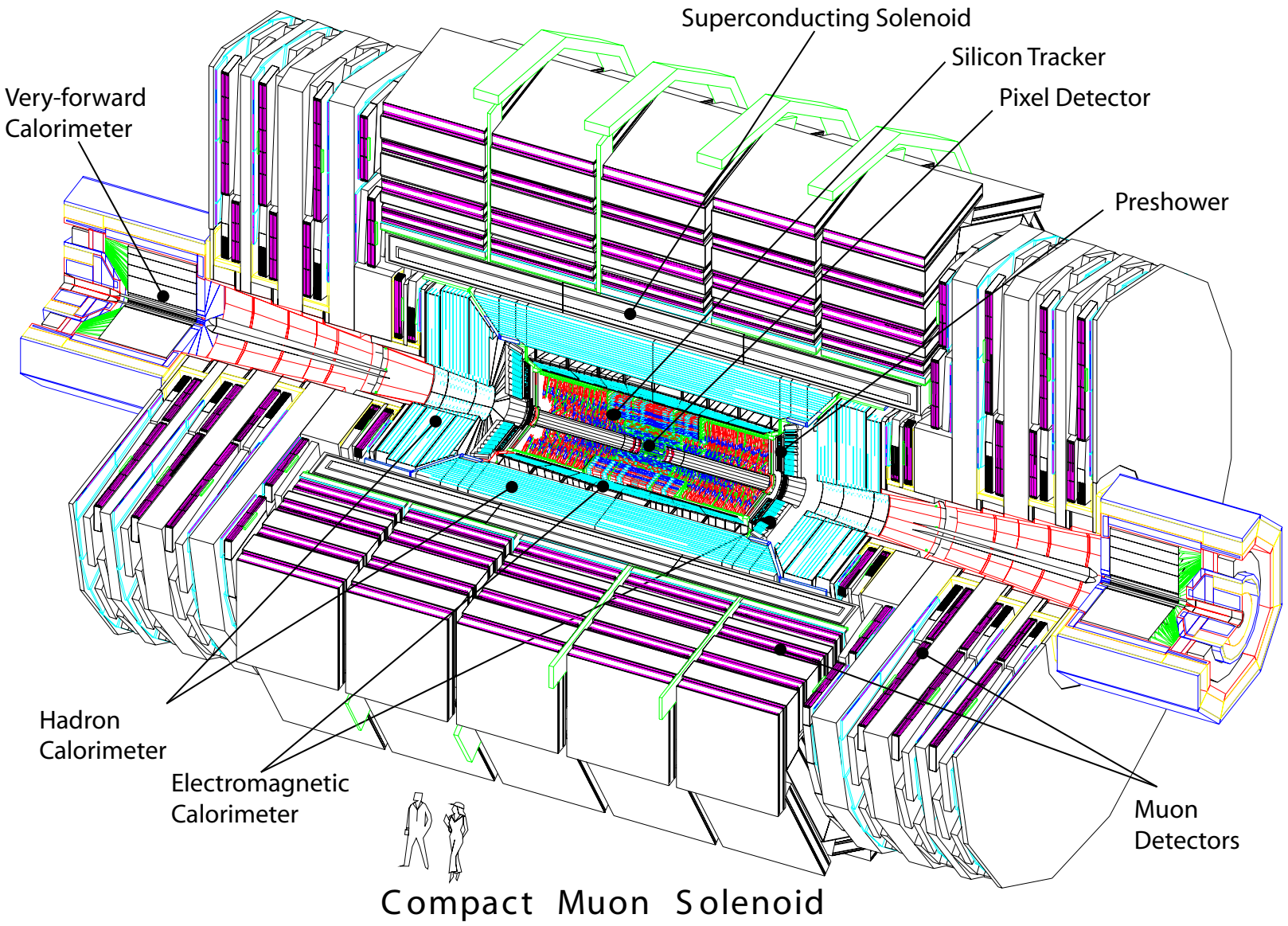

Figure 3.3: An overview of the CMS experiment, given to scale. [32]

3.2 The Compact Muon Solenoid Experiment

The CMS Detector [32] is located in the French village of Cessy to the north of the CERN main facilities. Naturally, it is located on one of the four instrumented interaction regions of the LHC, colloquially known as 'Point 5'[2], where the beams are brought into collisions. CMS's counterpart and direct competition at the LHC is the ATLAS detector, as both are general purpose particle physics detectors designed with the goal of discovering new physics, such as the Higgs Boson [7] or Super-Symmetry [41], along with a wide array of possible standard model physics applications. The design of CMS is indicative of the advancements in detector design over the years, exploiting combinations and new implementations of technologies from separate previous experiments.

The innermost region of CMS is instrumented with silicon pixel and strip detectors, to identify and measure the tracks of charged particles, out to a radius of 1.1m and is immersed in a magnetic field of 3.8 Tesla. Surrounding the tracker and still within the magnetic field volume are the electromagnetic calorimeter (ECAL) and hadronic calorimeter (HCAL) that measure the energy of electromagnetic or strong charged particles that are not minimum-ionizing. This design choice allows for accurate determination of electromagnetic and hadronic shower energies and hence particle identification. The 3.8 T superconducting magnetic coil is not instrumented for particle detection but is surrounded by muon chambers attached to a steel superstructure 'return yoke' that returns and contains the magnetic field generated by the coil. The muon chambers exploit the 2 T return field by measuring the further bending of muons as they traverse the return yoke. A to-scale representation of the CMS detector is given in Figure 3.3.

[2]ATLAS is located at Point 1, ALICE at Point 2 and LHCb at Point 8.

3.2.1 CMS Geometry

The CMS detector is cylindrical and has three major subdivisions, a central barrel region and two endcaps, each with an additional attachment containing instrumentation that requires proximity to the beam line. The detector is 14.6m in diameter and 21.6m in length. CMS uses a right handed Cartesian coordinate system with the origin located at the assumed interaction point at the center of the detector. However, this is not necessarily the point at which a proton-proton collisions will occur since the beam can be slightly off center to due alignment of the LHC. Furthermore, the bunches have non-trivial transverse and longitudinal extent and an interaction may take place anywhere within the volume where the colliding bunches overlap.

The CMS x-axis points towards the center of the LHC ring, the y-axis points radially outwards from the earth's center, and the z-axis is oriented along the anti-clockwise beam direction. From this, we define the usual cylindrical coordinates, $r = \sqrt{x^2 + y^2}$ and $\varphi = \arctan(x, y)$. The type of detector being used varies as r, for particle identification purposes, and the detector is symmetric in φ. Particular to hadron colliders, instead of using the polar angle from z-axis ϑ, the quantity 'pseudorapidity' (η) defines the second 'angle' in the coordinate system and is defined:

$$\eta = -\ln \tan \frac{\vartheta}{2} \tag{3.4}$$

This quantity is used since the distribution of nearly massless particles in η, is roughly constant. The constituent detectors of CMS each have specific ranges in η. The silicon tracker extends to $|\eta| < 2.5$ and the muon system to $|\eta| < 2.4$, changing detector technology over the eta range $0.9 < |\eta| < 1.2$. Both calorimeters are split into 'barrel' and 'endcap' regions, with the ECAL covering $|\eta| < 1.479$ and $1.479 < |\eta| < 3.0$. However, since cabling and other services must reach the tracker, the ECAL barrel and endcap are longitudinally separated at $|\eta| = 1.479$, causing poor

EM shower containment in the region $1.4442 < |\eta| < 1.560$. The HCAL has uniform coverage for $|\eta| < 3.0$. Finally the Forward Hadron Calorimeter (HF) covers the range $3.0 < |\eta| < 5.0$ and allows CMS to have hermetic calorimetric coverage for most of the solid angle as $\eta = 5$ corresponds to a polar angle of 13 milliradians from the beam pipe.

3.2.2 Silicon Tracker

The CMS tracking detector [42] is composed of two primary components, the silicon strip and silicon pixel trackers. Both operate using the same principles of deducing the location of a charged particle in a collection of pixels or on a doped strip of silicon using the ionization charge left by the incident particle. To achieve this, the sensors are constructed as reversed-biased p-n diodes, which yield a detectable current when the bias voltage across the diode is lowered by the ionization depositions. The use of silicon-based detectors is critical to the operation of the CMS tracker since the small thickness of the sensor results in very short charge collection times, allowing for fast readout. Additionally, the use of silicon allows for high detector granularity, granting excellent position resolution to reconstructed tracks, for a low cost in material. The layout of the complete CMS tracking detector is given in Figure 3.4.

Pixel Detector

The pixel detector [42] is closest to the interaction region and experiences the largest charged particle flux of the detectors in CMS. In order to not be overwhelmed by the charged particle multiplicity, the pixel detector has fine granularity with 65.9 million pixels covering an active area of roughly 1 m^2. The pixel detector uses 100×150 μ m^2 pixels and has excellent position resolution, $\approx$ 10 μm in the r-φ plane and 20 μm in the r-z plane. The full detector comprises three concentric layers forming a

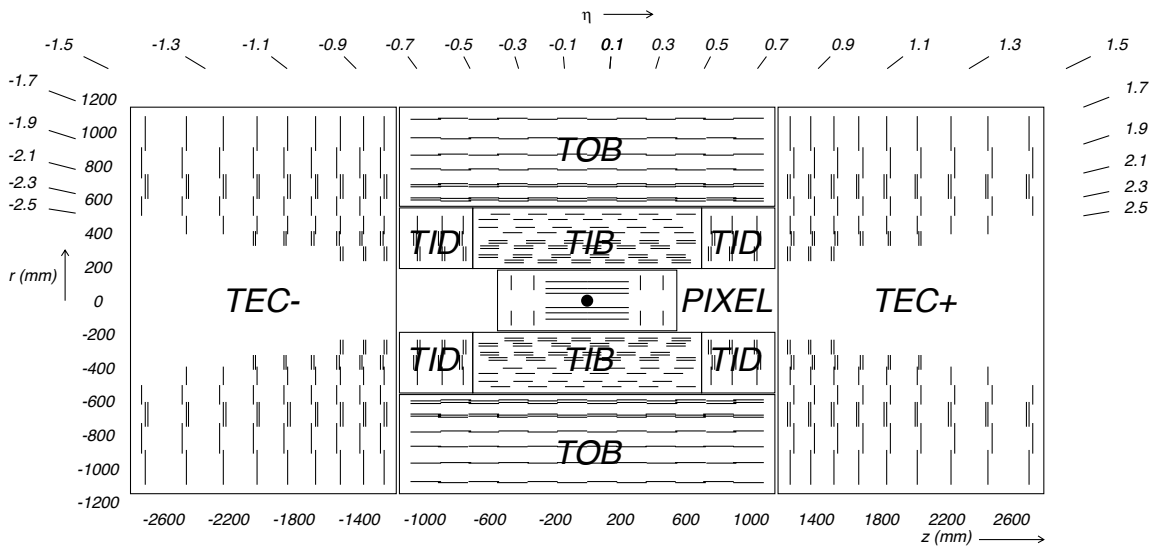

Figure 3.4: A cross section of the CMS Silicon Tracker, depicting its geometry in the rz plane of the detector and demonstrating η coverage of the instrumented region. [32]

barrel region and two layers on each side forming endcaps. The total η coverage of the pixels is $-2.5 < \eta < 2.5$, allowing the detection of tracks in a large portion of the full solid angle. Additionally, the proximity of the pixels to the interaction region allows for accurate and efficient identification of secondary vertices from particles with non-trivial lifetimes, such as b-hadrons and τ leptons.

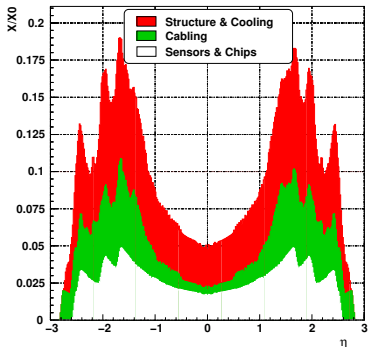

Figure 3.5: The number of radiation lengths, x, of material in the CMS pixel detector as a function of η. The immense data output and power usage of the pixel detector requires, for its size, intensive cabling and cooling. [32]

In the case of unconverted photons, which do not induce charge in the doped silicon, the pixel detector is used to identify electrons that have not been fully reconstructed and veto them. Due to the non trivial radiation length of the pixel detector, traversing the detector can induce pair-production of electrons from real photons, causing the photon to appear as though it is an electron since the pair-produced electrons will leave tracks. One radiation length, X_0, is the mean distance after which the electron or photon loses $1/e$ of its original energy as given by equation 3.5.

$$E(\mathrm{x})/E_0 = e^{-\mathrm{x}/\mathrm{X}_0} \tag{3.5}$$

The number of radiation lengths as a function of η in the pixel detector is given in Figure 3.5.

Silicon Strip Tracker

From 20 cm $< r <$ 110 cm the tracker uses silicon strip detectors organized into four functional units: the Tracker Inner Barrel (TIB), Tracker Inner Disks (TID), Tracker Outer Barrel (TOB) and Tracker EndCap (TEC) as depicted in Figure 3.4 [42]. The tracker consists of 11.4 million silicon strips distributed over 210 m^2 of silicon wafers. Due to the distance from the interaction point, the granularity and resolution of the tracker is less than that of the pixels. The TIB has a position resolution of 230 μm and the TOB 530 μm. Since the tracker is within the 3.8T magnetic field of the solenoid, the charged particles bend with radius of curvature R in the transverse plane of the detector according to:

$$R = \frac{p_T}{qB} \tag{3.6}$$

where $p_T = \sqrt{p_x^2 + p_y^2}$. Since the tracking detector has excellent position resolution, samples the charged tracks multiple times along their trajectories and is situated in

a strong magnetic field, the momentum measurements derived from it have very high resolution, given by:

$$\frac{\sigma_{p_T}}{p_T} = (15 p_T \oplus 0.5)\%(TeV), \ |\eta| < 1.6 \tag{3.7}$$

$$\frac{\sigma_{p_T}}{p_T} = (60 p_T \oplus 0.5)\%(TeV), \ |\eta| = 2.5 \tag{3.8}$$

This corresponds to 0.6% momentum resolution for a track with 40 GeV transverse momentum, typical of tracks coming from the e and μ decays of Z bosons. The momentum measurement resolution degrades as the track momentum becomes larger since the track's radius of curvature becomes larger and the track appears more linear in the tracking volume. This causes the experimentally observed curvature to be more and more subject to the position resolution of the detector as well as simply not sampling enough of the track to accurately determine the track's deviation from linearity, resulting in larger errors on the reconstructed momentum, with errors of 1.2% at 200 GeV and 15% at 1 TeV using only the tracker.

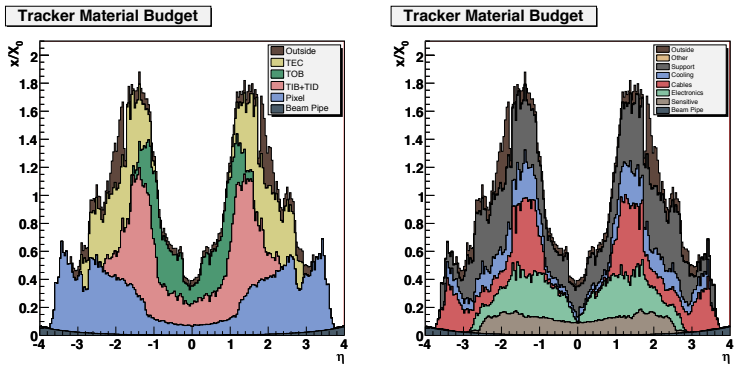

Figure 3.6: The number of radiation lengths, x, of material in the CMS silicon tracker, including the pixels, as a function of η. Regions with a large radiation length are prone to generating converted photons. [32]

Finally, due to the large amount material necessary to support and read out the information from the tracker, and the detectors themselves, the tracker forms up

to 1.8 radiation lengths, with an average of 0.8, in the detector before reaching the ECAL. Therefore, an electron will emit bremsstrahlung on average 55% of the time, with a maximum of 83% depending on rapidity. Likewise, photons will pair produce with equivalent rates before reaching the ECAL. This degrades the energy resolution of electrons and photons when being measured by the ECAL, since energy is lost in the tracker. Additionally for photons, this allows jets to fake photons more easily due to the two electron tracks and wider ECAL deposit from the electron and positron being separated by the magnetic field.

3.2.3 Electromagnetic Calorimeter

The CMS ECAL [43] is located immediately after the tracker at a radius from the beamline of 1.2 m. The ECAL radiator comprises 76,832 lead tungstate ($PbWO_4$) crystals, which are transparent and allow light from electromagnetic showers to be collected, integrating over the whole shower length. Lead tungstate is electronically dense, resulting in a very short radiation length of 0.89 cm. Since the crystals are also 23 cm long, all but the most energetic electrons and photons deposit all of their energy via bremsstralung and electromagnetic pair production in the ECAL crystals and none in the HCAL situated behind it. The readout electronics are located on the 'back' of each crystal, collecting all of the light emitted in the electromagnetic shower. The readout electronics consist of solid state avalanche photodiodes in the barrel region and radiation-hard vacuum phototriodes used in higher $|\eta|$, more 'forward', regions where the radiation dose is higher.

The gross organizational structure of the CMS ECAL is given in Figure 3.7. The ECAL is divided into the ECAL barrel (EB) in the range $|\eta| < 1.4442$, and the endcaps (EE) and endcap preshower detector (ES) both in the range $1.566 < |\eta| < 3.0$. The EB contains 61,200 crystals in 36 'supermodules' (SM) 18 in φ for each

half-barrel, each composed of 4 'modules' segmenting the SM in η. The EE contains 7234 crystals per endcap organized into 'supercrystals' each with a varying number of crystals. Lead tungstate has a density of 8.3 g cm^{-3} and a Molière radius (R_M), the transverse area that contains 90% of an EM shower in a given material, of 22 mm. The EB crystals are rectangular prisms have the dimensions 22 mm×22 mm×230 mm, corresponding to 25.8 radiation lengths in longitudinal shower depth and 1 R_M in the transverse shower size. The EE crystals are trapezoidal in shape, having a rear face of 30 mm×30 mm while the front face is as that of the barrel crystals. All of the crystals in the ECAL point towards the center of the CMS detector so that EM showers tend to be contained mostly within 3x3 sets of crystals as each crystal is roughly one R_M. The ES is composed of two layers of lead radiator interleaved with perpindicularly oriented wafers of silicon strips to estimate the EM shower shape before entering the more coarsely segmented EE with the goal of enhanced rejection of $\pi^0 \to \gamma\gamma$ events [43].

The use of solid lead tungstate crystals allows for excellent position and timing resolution. However, there is no longitudinal segmentation along the EM shower which impedes the ability of the ECAL to determine the angle at which photons enter the calorimeter. Each crystal contains most of a shower's transverse profile and the 0.89 cm radiation length induces showers quickly, with 80% of a shower's final light yield being produced within the first 25ns of interaction with the ECAL. This results in excellent energy resolution given by:

$$\left(\frac{\sigma}{E}\right)^2 = \left(\frac{2.8\%}{\sqrt{E}}\right)^2 + \left(\frac{0.12}{E}\right) + (0.30\%)^2 \tag{3.9}$$

The first term represents the statistical error coming from the stochastic nature of electromagnetic shower evolution. The second term represents the error in the energy measurement coming from electronic noise and a small contribution generated by

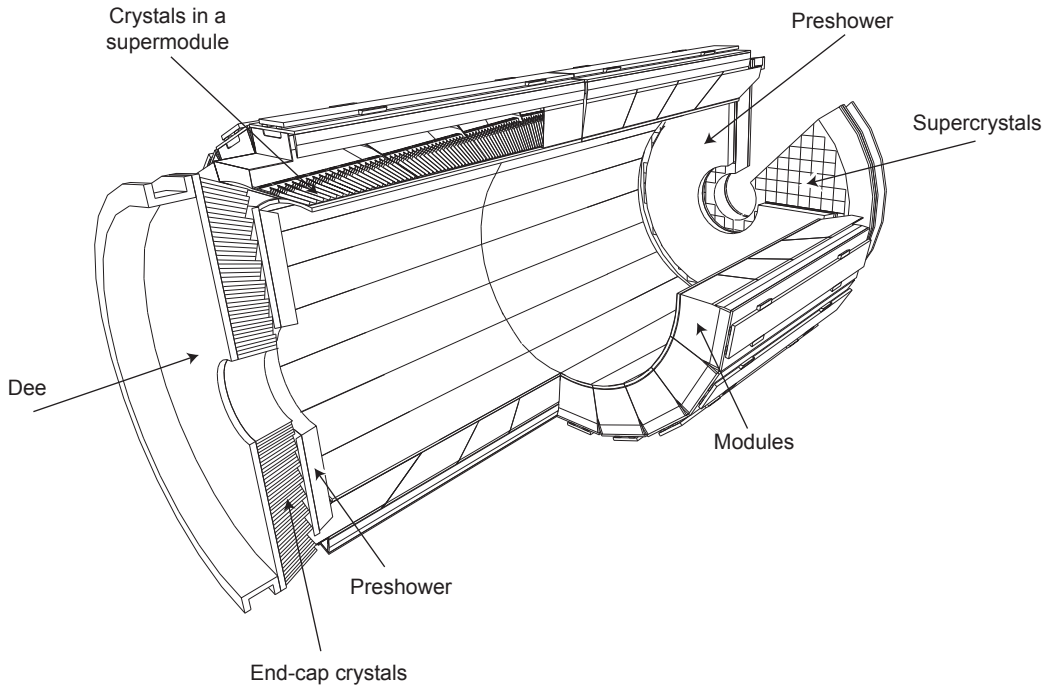

Figure 3.7: The layout of the barrel ECAL (EB) and endcap ECAL (EE). The EB crystals project towards the center of the detector to aid in reconstruction and uniform containment of electromagnetic particles that stop in the calorimeter. [32]

energy depositions from additional soft interactions (pileup). The final term is derived from intrinsic detector non-uniformities and calibration uncertainties. This results in the ECAL yielding useable energy measurements over three orders of magnitude from 1 GeV to 1 TeV, when EM showers begin to leak into the HCAL. Finally, the crystals manifest radiation damage as a change in transparency, yielding non-uniform scintillation light transmittance as a function of time. This is monitored and corrected for using a laser calibration system that records the change in transparency during the operation of the LHC [43].

3.2.4 Hadronic Calorimeter

Outside the ECAL is the HCAL [44] which measures strongly interacting particles by forcing them to interact with a dense material interleaved or embedded with a scintillator. Additionally, it has the largest angular coverage of all the sub-detectors of CMS and therefore plays a large role in the measurement of missing transverse energy, since it samples very forward energy deposits.

For analyses which do not rely on direct measurement of the missing transverse energy, the HCAL plays two additional important roles. First, the due to the large radiation depth of the ECAL, electromagnetic objects leave no energy deposit and so the absence of an HCAL deposit behind an electromagnetic deposit is indicative of a deposit from a true electromagnetic object, rather than a hadronic object that has interacted with a nucleus in the ECAL. Second, the large angular coverage of the HCAL allows for a complete description of pileup energy depositions. The residual effects of pileup such as an increase in the hadronic activity around and behind real EM objects can then be estimated and subtracted out.

The three sub-detectors making up the HCAL are all sampling calorimeters and their locations within the CMS detector are shown in Figure 3.8. The HCAL barrel and endcap, HB and HE respectively, are made up of interleaved layers of brass radiator and scintillating tiles to sample the shower as it forms. The forward hadron calorimeter (HF) is made of steel plates embedded with quartz fibers to better withstand the high radiation doses at forward angles. The HB covers the angular region $|\eta| < 1.305$ and the HE from $1.305 < |\eta| < 3.0$. The HF covers the very forward region from $3.0 < |\eta| < 5.0$.

The number of interactions a charged hadron undergoes while traversing material is characterized by the 'interaction length' λ_0. Unlike the radiation length, λ_0 is related to the nuclear density of the material. It takes a large amount of material

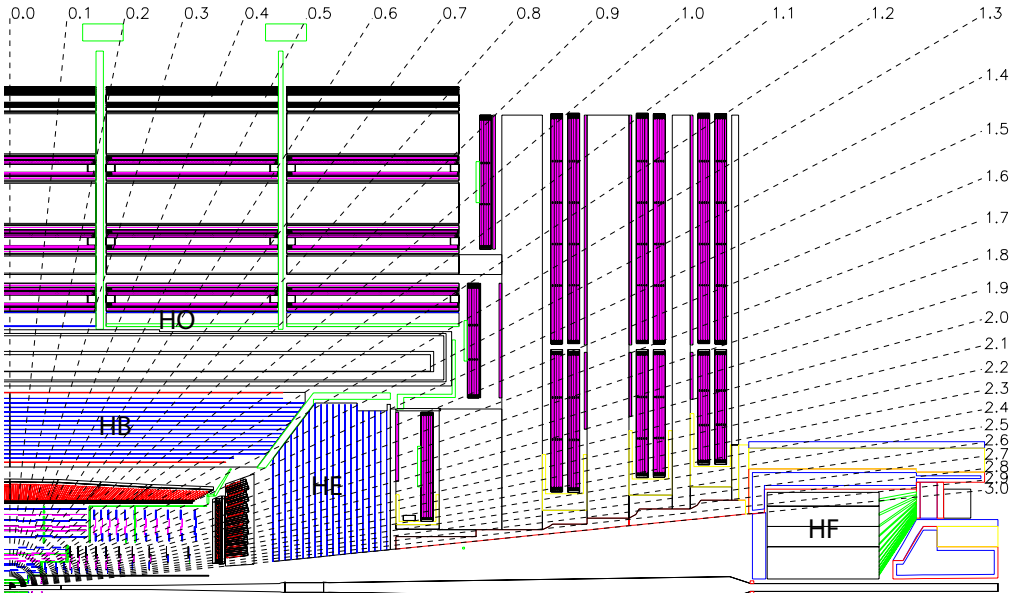

Figure 3.8: The layout of the various components of the CMS hadronic calorimetery. The Barrel HCAL (HB) and Endcap ECAL (HE) cover up to $\eta < 3.0$. The Outer HCAL (HO) helps to measure showers which are not contained by HB or HE. The Forward HCAL (HF) covers $3.0 < |\eta| < 5.0$, making the HCAL nearly hermetic in solid angle. [32]

to create a hadronic calorimeter that contains the entirety of an energetic hadronic shower. Similar to a radiation length, an interaction length is the corresponding metric for hadronic interactions giving the number of interactions a particle will undergo, as given by the energy loss. Since the interaction length is governed by nuclear interactions, the showers generated in the radiating material of the calorimeter will be extended over a long distance, increasing the time needed for light collection. In the case of a sampling calorimeter, this increases the dependence of the measured energy of the shower on its stochastic evolution within the calorimeter.

In the case of the HB and HE, the particles produced in nuclear interactions of hadronic particles with the brass radiator pass through the interleaved scintillating material to produce light. The collected light is used as an estimate of the energy of the shower. For the HF, Cherenkov radiation from the particles in the evolving

shower traversing quartz fibers is used as the energy estimate. These two methods of estimating the energy in the shower yield different energy resolutions, which are given in Equations 3.10 and 3.11:

$$\left(\frac{\sigma}{E}\right)^2 = \left(\frac{90\%}{\sqrt{E}}\right)^2 + (4.5\%)^2 \quad \text{HB and HE} \tag{3.10}$$

$$\left(\frac{\sigma}{E}\right)^2 = \left(\frac{172\%}{\sqrt{E}}\right)^2 + (9.0\%)^2 \quad \text{HF} \tag{3.11}$$

Here, the first term in each equation is the stochastic term in the resolution, which is considerably larger than that of the ECAL, and the constant term is due uncertainties in calibration.

3.2.5 Muon Detectors

Situated furthest from the interaction region are the CMS muon detectors [45]. They are placed after the calorimeters and the solenoid and serve the primary function of accurately tagging muons. Muons are minimum ionizing particles and do not deposit much of their energy in the calorimeters, allowing them to leave the inner CMS detectors. The muon detectors also serve as tracking detectors in the return field of the CMS magnet, giving enhanced resolution at large transverse momentum, as seen in Figure 3.10. The muon system is composed of three subsystems, the drift tubes (DT), the resistive plate chambers (RPC) and cathode strip chambers (CSC). Each subsystem's layout can be seen in Figure 3.9 and the subsystems used vary as a function of η depending on the expected rates of muon and background particles from the LHC.

The DT comprise the barrel region of the muon system, covering the pseudorapidity region $-1.2 < \eta < 1.2$. The CSCs form the two endcaps of the system, covering $0.9 < |\eta| < 2.4$. The RPCs cover the region $-1.6 < \eta < 1.6$ and provide redundancy as well as significantly more accurate timing. The central detectors operate in

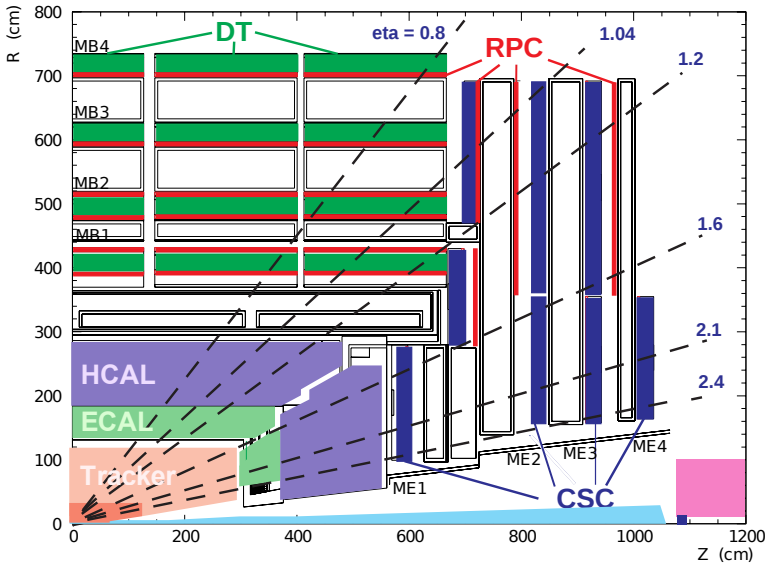

Figure 3.9: An rz cross section of the CMS muon system, demonstrating the η coverage and overlap of all constituent subsystems. [46]

a relatively stable 2 T return field oriented in the opposite z-direction of the main solenoidal field of CMS. The forward detectors operate within the point of the flux return where the magnetic field is rapidly varying in magnitude and direction as a function of distance from the interaction region. This results in worse p_T resolution, as demonstrated in Figure 3.10 not only because of the larger amount of material traveled, but also since the track is less perpendicular to the solenoidal magnetic field. Despite containing a non-uniform magnetic field, the endcap muon system can still improve the momentum measurement of high p_{T} muons.

Drift Tubes

The drift tube system makes up the instrumented volume between the steel layers of the return yoke in the barrel. The full chambers consist of multiple drift tubes, each containing an anode wire and two cathode strips on either side, as in Figure 3.11. As the particles traverse the drift tube, they ionize the gas in the tube and the ionized

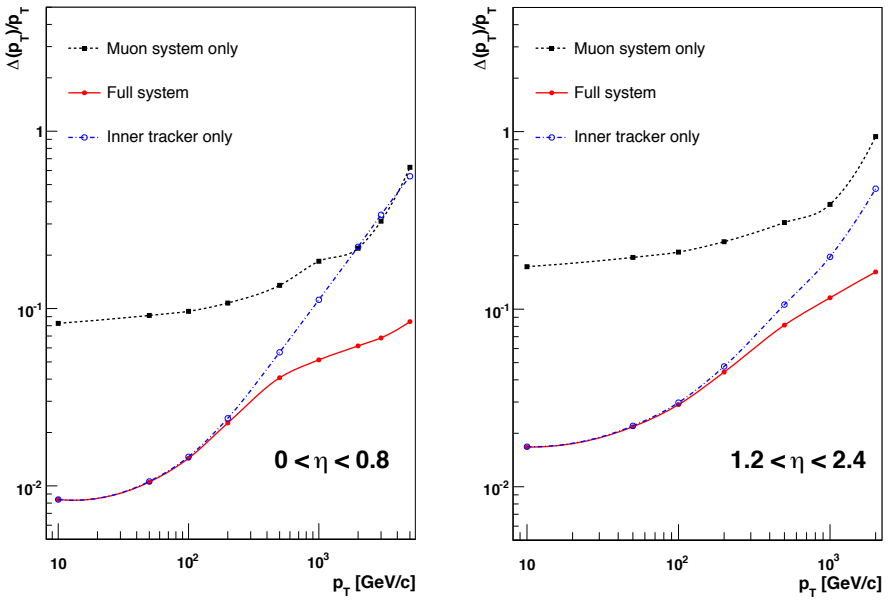

Figure 3.10: The momentum resolution of muons using the three possible choices of momentum measurements, from the silicon tracker alone, the muon system alone and the combined tracking fit of the silicon track and muon systems. Note the improved momentum measurement at large p_T from including the muon system. [32]

atoms are collected by the anode, creating a detectable electronic pulse. Since the electric field generated by the anode of the square drift tube in the return field is well known, the arrival time and shape of the electronic pulse can be interpreted as the distance of the charged particle from the anode wire. To measure the charge particle's track over the full chamber, there are multiple drift tubes measuring this distance organized into to two layers in the chamber. The spatial resolution of a DT chamber is 100 μm in the r-φ place, and 150 μm in the z direction, with a drift time of 386 ns and timing resolution of 3.8 ns using 3 consecutive staggered drift cells, estimated using test beam data. The high timing resolution is important for triggering and allows for accurate assignment of identified muons to correct bunch crossings, since bunches are spaced 50ns apart in 2011 running and 25ns apart in LHC design specifications. These measurements can then be turned into a 3+1 dimensional line segment, representing

the direction and timing of the particle as it traversed the chamber. Finally, since there are four 'stations' of chambers, as depicted in Figure 3.9, the evolution of the track's direction over the whole DT system can be measured. From this ensemble of information, the muon's track can be reconstructed as it traverses the DT system.

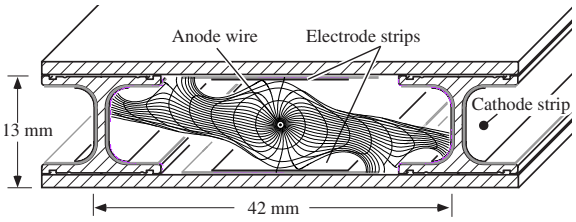

Figure 3.11: A schematic representation of a single drift tube in one cms drift tube chamber. The position of charged particles traversing the chamber is inferred from the 'charge radius' of ionized particles that drift towards the anode wire. [32]

Cathode Strip Chambers

The cathode strip chamber system in CMS covers the forward endcap disks of the detector. The change in detector technology is motivated by the higher particle flux, in terms of muons and muon backgrounds, encountered at more forward angles. CSCs have faster refresh times with signal pulses lasting 150 ns, accomodating a higher rate. To determine the position and timing of a charged particle that traverses the CSC system, two methods are exploited simultaneously. A schematic representation of these methods is given in Figure 3.12.

The strips of the CSCs function by measuring a charge pulse being induced on copper strips that is collected over time to determine the position on the strip with a resolution of better than 100 μm, depending on the strip size. However, due to the spatial extent of the strips, the timing resolution from this alone is very poor, greater than 25 ns, and cannot be used for precision timing. To augment this, the timing information from the anode wires is used yielding timing resolution of 15 ns

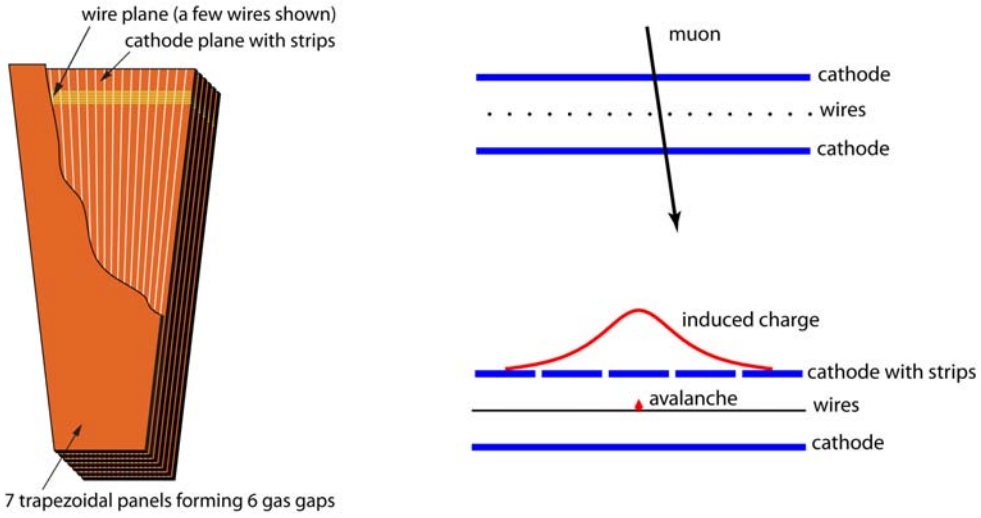

Figure 3.12: The layout of a cathode strip chamber in CMS. The figure on the right demonstrates how the traversing particle's position and timing are deduced by induced and deposited charge in the chamber. [32]

for a single plane. This, in addition to finer granularity compared to the DT system, allowing for considerably higher fluxes through the detector without performance loss. Additionally, the CSCs achieve good spatial and timing resolution of less than 100 μm and 7 ns, respectively, using a whole chamber. To construct a 3D representation of the muon track as it passes through the chamber, there are 6 layers of strips and wires in a CSC. The CSCs are organized into four layers (stations) of concentric rings of chambers. The most important of part of these stations being the portion of innermost station, 'ME 1/1' that is situated directly behind HE, within the strong magnetic field, and allows the transverse momentum to be measured more accurately than using only the fringe field in the stations more distant from the interaction region.

Resistive Plate Chambers

RPCs are used over a wide η range in CMS from $-1.6 < \eta < 1.6$ and contribute excellent timing resolution to the muon system's measurements. The RPCs are constructed of two highly resistive electrodes and a layer of readout strips immersed in a thin layer of inert gas, as shown in Figure 3.13. As charged particles traverse the RPC, the gas is ionized and releases electrons which then, due to the 9 kV electric field in the RPC, ionize more atoms, releasing more electrons in an 'avalanche'. These avalanches of electrons are collected on a cathode pad and used to deduce the timing and position of the incident particle. Due to the compact design, simple readout and high voltages used in the RPC the timing resolution is small and less than one nanosecond.

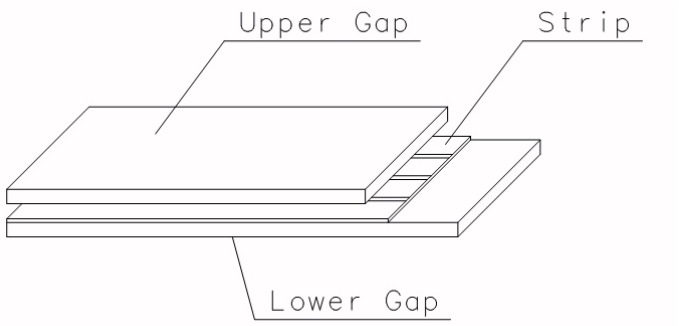

Figure 3.13: Resistive Plate Chambers are of significantly simpler design than the DTs or CSCs and are used as a robust redundant system to the other muon subsystems. The detector operates in a similar manner to the wires of the CSCs and have a timing resolution of roughly 1 ns. [32]

Since the design configuration of the LHC specifies 25 ns bunch spacing the requirements on timing of the CMS muon system are exceptionally stringent given the distance of the detectors from the interaction point. The excellent timing resolution of the RPCs significantly improves the CMS detector's ability to assign a detected muon to a specific collision in the LHC. However, since the RPCs do not give 3D in-

formation about the trajectory of the muon passing through them and the subsystem has a comparatively poor spatial resolution of 1 cm; the momentum and spatial resolution are correspondingly worse than that of the DT or CSC subsystems if only the RPC system is used to measure a muon's momentum. To measure the best estimate of a muon's momentum and timing the systems must be used collectively.

3.2.6 Trigger

The total rate of interactions at the LHC can be calculated as follows:

$$\frac{\mathrm{d}N}{\mathrm{d}t} = < N_{\mathrm{PU}} > \sigma_{pp\to X} \frac{\mathrm{d}\mathcal{L}}{\mathrm{d}t} \tag{3.12}$$

where $< N_{\mathrm{PU}} >$ is the average number of simultaneous collisions per bunch crossing and $\sigma_{pp\to X}$ is the total inelastic cross section for proton-proton collistions at 7 TeV, 68.3 mb. This results in a total collision rate, at the design parameters of the LHC [30], of 1 GHz. The average size of an event at design luminosity, including all detector information, is 1 MB [47]. The average size event size in 2011 running was 300 kB/event. This would yield a information rate of 1 PB s^{-1} for the design luminosity of the LHC, which obviously cannot all be archived for analysis. To meet the challenge of achieving an acceptable rate of data that also contains physically useful information, a multi-tiered and highly configurable triggering system is used by the CMS Experiment. The major division in the trigger is between the level-one, 'L1', trigger and higher level trigger, 'HLT'. The 'L1' trigger reduces the input rate of events from 1 GHz to less than 100 kHz for real-time processing by the HLT which then reduces the rate to 300-600 Hz using simplified or even the same reconstruction techniques used in the full, offline, reconstruction. The events selected by the HLT are stored for later offline analysis.

Level-1 Trigger

The L1 trigger is composed of dedicated electronics that perform real-time, pipelined physics calculations with a total latency of 3.2 μs[3] [48] at the rate of the LHC clock, 40.08 MHz. As mentioned previously, the L1 trigger serves to reduce the data rate by six orders of magnitude to 100 kHz. Due to the high input data rate, the L1 trigger cannot use the information from the silicon trigger, since it cannot be read out quickly enough, and relies soley on the information of the calorimeters and muon systems. The L1 trigger achieves this goal by using embedded reconstruction and identification algorithms to loosely select events with possibly interesting physics. Specfically, the L1 trigger identifies muons, electromagnetic objects[4], missing transverse energy ($\not\!\!E_T$), jets, and τs as well as combinations of any of these objects.

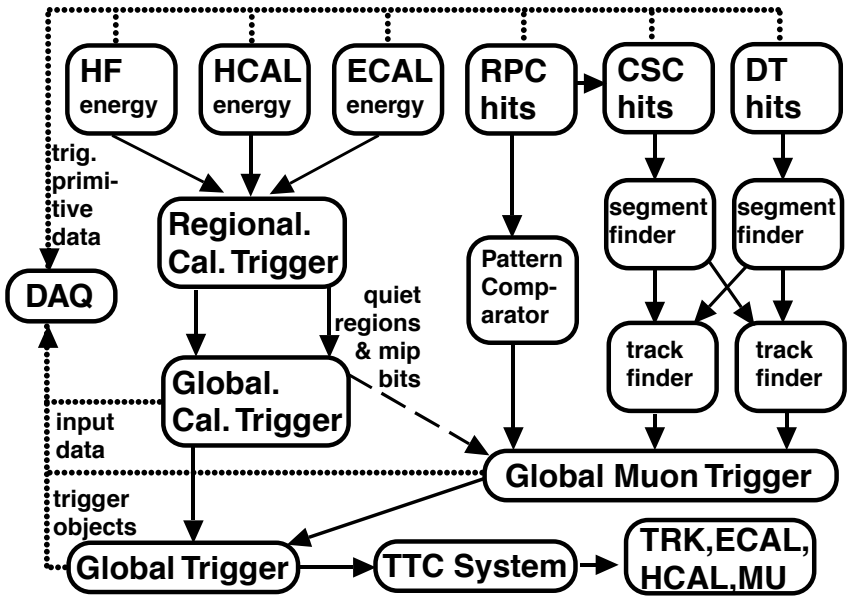

Figure 3.14: A diagramatic representation of the information into, within and out of the CMS Level-1 Trigger System which is used to reject the majority of of the uninteresting collisions at the LHC. [48]

[3] 1-1.5 μs is used for calculations, the rest is for cable delays.

[4] Electrons and photons appear the same at L1 due to the lack of tracking information.

The flow of information in the L1 trigger is depicted in Figure 3.14. Each subsystem, with the exception of the CSCs, contributes all of its information to the L1 trigger decision. The calorimeter information is first processed by the regional calorimeter trigger (RCT) which looks for the signatures of electromagnetic deposits and jets, dividing the detector into 5×5 'towers' of ECAL crystals and single units of HCAL readout channels and performing energy sums in 4×4 regions of these towers. The Global Calorimeter Trigger (GCT) receives from the RCT information describing eight electromagnetic energy deposits and four jets. This information is sorted then used to calculate detector wide energy sums and coarse estimates of the missing transverse energy.

The DT and RPC muon triggers each, in real time, use the recorded waveforms from ionization deposits to find the patterns of hits consistent with muons coming from the interaction region. In the case of the RPC subsystem this is always done looking at an entire station to find a set of hits. The DT subsystem can look for these patterns first at the chamber level, since their chambers contain multiple drift tubes, creating 'segments'. The CSC subsystem has additional step of a chamber-level pre-trigger on the cathode strips. This pretrigger means a CSC will only be read out if a configurable number of layers, normally 3, of cathode strips are active. After pre-triggering two segments per chamber are found with dedicated hardware. The segments are then sorted per station in units of 30 or 60 degree 'sectors' by quality criteria[5]. Then, for both the DT and CSC subsystems, patterns of segments are combined together to find and measure tracks. The subsystem-level triggers are merged together to create a 'global' interpretation of muons for the entire muon system, allowing explotation of the overlap between sub-detectors and the information reconstructed by each trigger. Finally, the information from the calorimetry and muon

[5]Number of hit anode and cathode layers and coincidence.

system are combined in the Global Trigger to provide configurable triggering based on possibly complex mixed event topologies, consisting of calorimetric and muon data.

High Level Trigger

The last level of event selection before the event is considered fully selected and written to disk for further analysis offline is the HLT. The HLT uses a computing farm to reconstruct events using software based algorithms to filter out events tagged as interesting by the L1 trigger but are in reality jet-fakes from QCD and other backgrounds. Notably, unlike previous experiments, there is no dedicated 'level two' trigger that attempts to reduce the rate further before the final HLT reconstruction. Instead, to reduce the overall CPU usage, the HLT retains a pipelined structure and stops executing a decision 'path' when a step in that path fails. The L1 trigger completely determines which HLT decision paths will be run. If there are only muons present in the event and no interesting electromagnetic deposits then only muon reconstruction algorithms will be run.

The HLT gains most of its rejection power and selection efficiency from the ability to include tracking information due to the significantly lower input rate to the HLT, allowing the tracker to be read out. For example, until the final stages of the HLT, muons are treated only using the information from the muon system. Once the muon-system-only tracks are matched with their corresponding tracks in the tracker and reevaluated, the resolution improves by nearly an order of magnitude as can be seen in Figures 3.10 and 3.15. This allows the HLT to very efficiently select high p_T muons, which is of paramount importance for selecting the signatures of electroweak bosons. These same optimizations and improvements coming from inclusion of tracking information apply to the identification of electrons in the trigger, supplying improved energy resolution and better jet rejection. Particularly in the case of

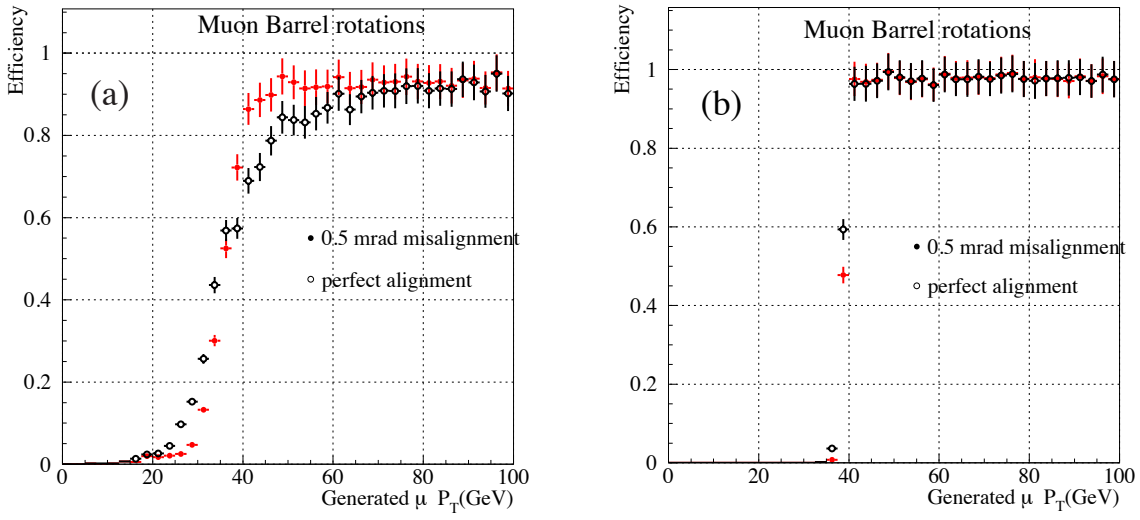

Figure 3.15: The improvement in the muon momentum resolution when including the information from the silicon tracker in the High Level Trigger for different muon system alignment scenarios. Note that the muon resolution improves by nearly an order of magnitude when including the silicon tracker information. [47]

selecting Z bosons, the CMS trigger can be configured to trigger on pairs of muons or pairs of electrons. Since high p_T lepton pairs are rare and difficult to fake, the energy thresholds on these objects can be kept very low even for very high luminosities, providing a rich baseline dataset to study the production of Zγ with muon and electron decays.

Chapter 4

Event Simulation

Physicists' present knowledge of Electroweak Theory and QCD allows a precise description of fundamental interactions. However, at the LHC, the presence of high energy colored partons in the interaction requires the understanding of processes with additional energetic QCD radiation, creating considerably more complex final states. While the Matrix Elements for processes are still integrable and treatable using equation 2.2, the initial and final states become complex to the point that an analytical treatment becomes nearly impossible, requiring the use of numerical techniques to evaluate the full integral. Furthermore, the statistical interpretation of many processes in detector physics such as shower stochastics, energy loss, and detector noise are easily implemented and considerably more useful in the context of numerical simulations. The most widely used and flexible of these techniques are known as 'Monte Carlo' (MC) algorithms [49], due to their reliance on random numbers and non-deterministic behavior. The core idea of these algorithms is that the function being randomly sampled has a 'stable distribution' to which the statistical estimate of that function will converge, given enough sampling. These methods, in concert with the theoretical descriptions of fundamental interactions and interactions

of particles with material provide a complete and accurate simulation of particle physics detectors and the interactions they observe. This allows a wide array of studies to be performed and realistic comparison of theoretical models to data.

4.1 Phase Space Integration and Event Generators

In order to calculate the integral of a matrix element, and thus determine the cross section of a given process, the multidimensional volume that comprises all sets of momenta accesible to the process, or 'phase space', must be determined. For the MC treatment, this corresponds to sampling an n-dimensional cube of random numbers, where n is the number of free parameters in the integrand, and assigning to each point a weight given by the integrands' value and a volume. In the case of calculating cross sections, the integrand typically corresponds to a parton level matrix element, i.e. something that can be represented by Feynman Diagrams. If the matrix element being integrated has a peaked shape or sharp edges, due to a resonance, kinematic cut, or proximity to a singularity, blind random sampling becomes inefficient and techniques known as 'importance sampling' [50] must be used to calculate accurate integrals. These computational methods together allow the simultaneous calculation of total and differential cross sections, since the differential cross section is simply the sampled phase space points projected along some chosen variable. This provides a powerful tool in terms of the validation of theory, since the full sets of four momenta of a given final state are provided, and allows any distribution of interest to be calculated and compared to data.

In order to generate events, the same MC techniques are exploited in a two phase procedure. First the distribution that the events are generated from must be deter-

mined. This is exactly equivalent to the phase space integration, except that during the sampling of the phase space the maximum weight encountered is saved. Then the distribution is sampled again and the ratio of a given event's weight to the maximum weight is used define a survival probability. A random number on the unit interval is drawn and the sampled event is saved or rejected if the random number is below or above the survival probability. This technique is known as 'unweighting' [51] and by construction yields a collection of events that have exactly the distribution of the integrand, but with each event having unit weight. In high energy physics, unweighting is exceptionally useful since it reflects the manner in which events are produced in nature, and allows statistical techniques to be applied per-event without the need to account for intra-event correlations that are encoded in phase space weights.

4.1.1 Matrix Element Generators

Matrix Element Generators are programs which implement phase space integrals of matrix elements and include the effects of parton distribution functions and possibly higher-order corrections. Some examples of these programs are: Pythia [52], MadGraph [53], SHERPA [28], POWHEG BOX [54], and MC@NLO [55], each of which implement a large number of processes. These programs need only very simple input information, such as the type of colliding particles, the beam energy and requirements on the final state particles. Specifically in the case of Zγ, the MadGraph5 (MG5) generator is used to produce Zγ events with 0, 1, and 2 additional 'hard' partons in the final state at $\sqrt{s} = 7$ TeV. A parton is considered hard when it is produced with large p_T, well above the QCD scale of $\Lambda_{\mathrm{QCD}} = 217^{+25}_{-23}$ MeV where perturbative QCD is valid. MG5 is an automatic matrix element generator and, given this information, determines algorithmically all of the contributing Feynman Diagrams for the requested processes. It then performs the unweighting procedure on the result-

ing matrix elements to produce 'parton level' events that are properly distributed in initial state parton type according to parton distribution prediction, initial state momentum, and final state momenta of the process. These parton level events are saved for further processing by a parton shower monte carlo where they are evolved into fully decayed 'exclusive' events and is discussed in Section 4.1.2.

4.1.2 Parton Shower Monte Carlo

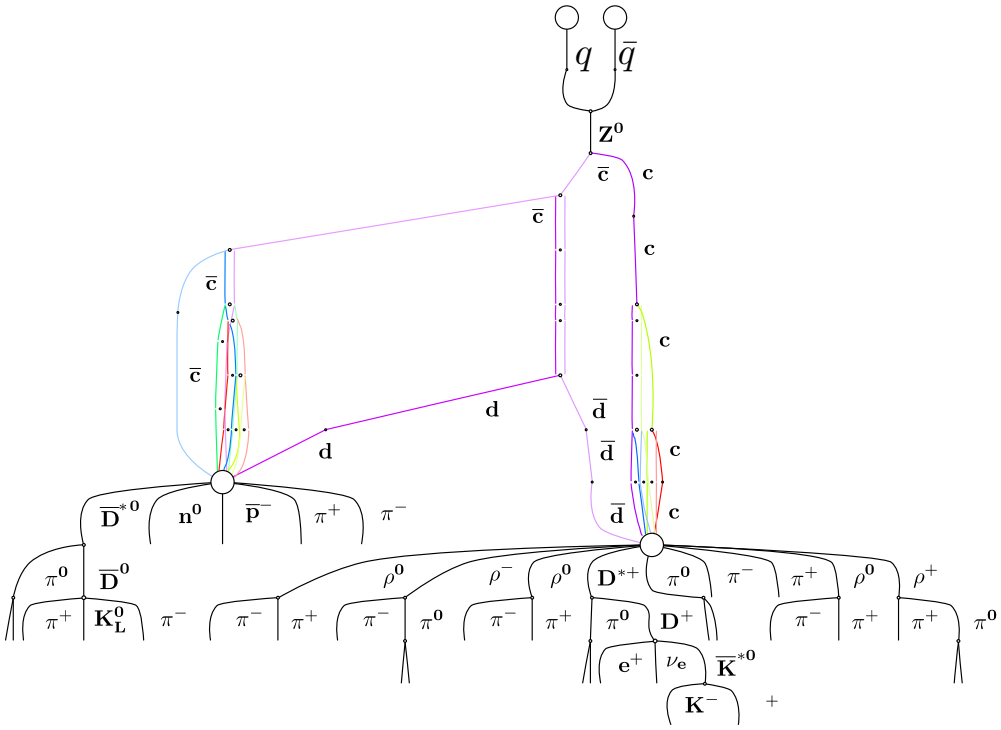

Figure 4.1: An example event demonstrating schematically all of the effects simulated by a parton shower monte carlo in a hadronic Z decay, including the parton shower (colored lines labelled by quarks) and hadronization (black lines labelled by hadrons). [56]

Parton Shower Monte Carlos, SMCs, simulate the evolution of energetic final state colored partons into jets, in addition to the approximation of the effects of initial and final state radiation of photons, gluons, and quark pairs. The evolution of

a parton level final state quark or gluon is acheived in two steps. First, the parton is taken from the matrix element generator and the probability of the splitting processes $q \to qg$, $g \to q\bar{q}$, and $g \to gg$ for some energy of the emitted parton are evaluated and stochastically applied. Once the parton splitting has occurred in the simulation, the same algorithm is applied recursively to all daughter partons until the energies of all partons are individually less than Λ_{QCD}. If a splitting results in an especially energetic new particle that is separate from the main jet that is forming, this is known as final state radiation. This creates a 'shower' of collimated partons, which then need to be hadronized into color singlet states to represent a physically observable jet. At this point, the treatment of the problem using perturbative QCD is no longer valid and the showered partons are turned into hadrons using phenomenologically motivated 'fragmentation' probabilities. Additional initial state radiation can be simulated using the same framework as the evolution of a jet, using initial state partons from the beam as the initial leg of the shower and forming a new parton shower from this additional interaction.

After applying the parton showering to an unweighted event it represents an approximation of all the high energy, 'hard' and low energy, 'soft', interactions that could have occured from the interaction of the two initial state partons. However, since there is an exchange of color charge in the event, the other quarks in the remnants of the colliding proton must re-hadronize and in the process of doing so emit soft radiation. This radiation from the proton remnants is known as the 'underlying event'. With the addition of the underlying event, the SMC corrected unweighted event represent a fully decayed 'exclusive' event and reflects a full theoretical understanding of what happens in nature during a single high energy collision.

These exclusive events are then ready to be further processed by a detector simulation for a further degree of realism and this is discussed in Section 4.2. However,

the issue of merging the additional matrix element level partons using SMC will be discussed first since it is of importance to this analysis.

4.1.3 Merging Matrix Element Events with Parton Showers

In the ongoing quest to develop better descriptions of proton-(anti)proton collision data it was found that using leading order theoretical predictions in monte carlo generators, even with full treatment of of ISR and FSR, resulted in disagreement with the observations in data. These effects become especially pronounced when the process being simulated has a large transverse boost, as seen in Figure 4.1.3. This disagreement is due to the leading order parton level event having no intrinsic p_T and the leading order treatment of the parton shower SMCs, in this case Pythia's implementation [52] but equally applicable to other leading-log parton showers. Since each additional ISR shower is produced without taking into account the possiblity of multiple partons being emitted at once, it significantly reduces the probability that the simulated event will recoil with large p_T since this part of the total phase space is reduced.

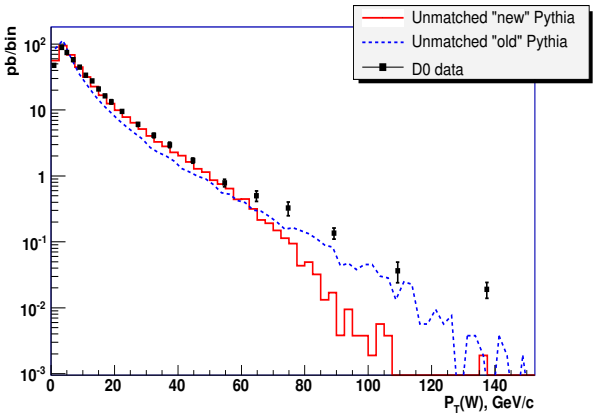

Figure 4.2: D0 data demonstrating the disagreement of the Pythia MC program with W p_T data, even after an updated tune. [57]

This disagreement makes the important point that SMCs are only accurate in the 'soft-collinear' approximation and aren't expected to work for energetic or wide-angle QCD radiation. To combat this shortcoming, the process being studied can be generated such that additional initial state radiation is included at the parton level, which solves immediately the problem of artificially restricted phase space. Additionally, this solves the problem of the radiation not being accurate at large angles since this is where the parton-level radiation is accurate, because it is perturbatively calculated without the soft-collinear approximation. Because of the different choice of approximations the parton-level radiation is not accurate when it is soft or collinear, to the point of causing unphysical singularities in the cross section. Finally, there is also the problem of 'double counting' where the SMC can produce the same jets in an event with no parton-level radiation as an event that has parton level radiation.

The double counting occurs despite the fact that different approximations are used because there is an overlap in phase space between the two treatments. In particular, the SMC can produce wide-angle or high energy radiation, but it will not have the right distribution since it is heavily supressed by the assumed soft-collinear approximation.

To solve these problems simultaneously various techniques for determining when to use parton level radiation vs. the SMC, known as 'matching', were developed. Two matching schemes exist MLM [58] and CKKW [59], each of which solve this problem. Here, only the MLM method will be discussed, as the core ideas between the two are very similar. The MLM method works by vetoing input events with parton level radiation if the SMC produces a hadronized parton shower that is more energetic than the 'matching scale', usually some minimum p_T, unless the event has the highest parton-level multiplicity being considered for matching. This solves the double counting issue since any events that would be double counted are explicitly

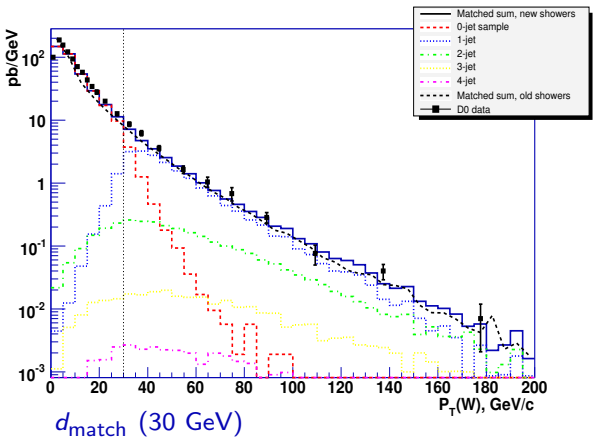

Figure 4.3: Matching results using the MLM technique, note that above the matching threshold d_{match} the contribution from parton-level radiation dominates and describes the observed distribution from D0. [57]

removed. The choice of when to use the SMC for radiation and when to use the parton-level radiation is implicit, since any radiation below the matching scale must come from the SMC. The result of matching a sample using the MLM methdology that contains parton-level radiation with up to four quarks or gluons and a matching scale of 30 GeV is shown in Figure 4.1.3. A majority of the MC samples used for signal and background predictions in the Zγ analysis have been matched using the MLM method.

4.2 Detector Simulation

With the exclusive event fully determined by the matrix element generator and subsequent treatment by the SMC, the event information can be propagated into a simulation of the CMS detector. The simulation is built using the toolkit GEANT4 [60] and has a variety of models and parameterizations that describe the interaction of particles with matter. The simulation keeps track, in detail, of the materials comprising sensitive detector elements, readout electronics, and uninstrumented structural ma-

terial. Additionally, the simulation keeps a detailed model of the CMS magnetic field that is derived from measurements taken from the real detector, allowing for accurate simulation of the trajectories of particles. Furthermore, with this description GEANT can statistically model how a variety of particles interact, both electromagnetically and strongly, with the detector materials, predicting a variety of distributions such as raw light yields in scintillating material and charge depositions in doped silicon. After GEANT has simulated the raw information that various detectors collect, a detailed electronics simulation of every subdetector is applied. This allows for a fine grained and tuneable estimation of additional detector effects, such as analog noise, and yields a realistic respresentation of the detector output given the estimation of the input from GEANT. The simulated detector response is stored in the same raw data format as used by the CMS detector so that exactly the same reconstruction algorithms are used in simulation as in real data. In addition to the detector response, the simulation and generator information is saved and can be used to calculate measurement extrapolations, efficiencies and calibrations.

Chapter 5

Event Reconstruction

Events that pass the preselection of the trigger are archived to disk at a rate of 200-400 Hz for detailed analysis. The full information of each subsystem is recorded separately. This yields a full description of the event but only at the level of individual detectors' responses to particles produced in the collision. To understand the collisions in a physically intuitive way, the responses of the subdetectors must be analyzed together; searching for and collating correlated signatures of interesting particles such as electrons or muons. The techniques for achieving this are collectively known as 'reconstruction'. For the $Z\gamma$ analysis the reconstruction of muons, electrons, and photons is of primary interest.

5.1 Track and Primary Vertex Reconstruction

Electron and muon recontruction both critically depend on the ability to accurately find and precisely measure the momenta of charged tracks from collisions in the CMS detector. Due to the tracker's high position resolution and fine granularity, as well as the 3.8 T magnetic field, this can be done with high efficiency with CMS. Tracks in

CMS are found using an iterative process beginning with the 'seeding' of the tracks from pairs or triplets of pixel and strip deposits, or 'hits', closest to the beamline.

Seeds are found by performing helical track fits of silicon detector hits over a small radial distance from the beamline to reduce bending and noise effects, resulting in tracks that approximate straight lines. These seeds are then used as initial guesses, or candidates, for the momenta of all possible tracks to be reconstructed using the silicon information. For each track candidate, hits further away from the interaction region in the silicon track are searched for by propagating the current track hypothesis to the next layer of silicon and searching for hits within an error window about the track. This error window is determined by the position resolution of the tracker, simulation of possible multiple scattering of the particle within the material of the tracker, and the error in the measured magnetic field. If a hit within the error window is found, it is added to the track and the parameters of the track are redetermined to improve the measurement of its momentum and errors. This process is then iteratively repeated until there are no more detectors which may have information to add in the track's path. This process of continually updating the track as new information is added and accounting for errors to regenerate the track hypothesis is known as Kalman fitting and smoothing [61]. Finally, once a track is found it is rebuilt reversing the propagation direction of the track and assembling the track from the outer tracker inwards, reducing the rate of fake tracks. This technique is used in the muon system as well to find muon tracks leaving the silicon tracker volume.

At the LHC the expected number of interactions per beam crossing is much larger than one, meaning that tracks originate from more than one point, or 'vertex', within the interaction region. The position of vertices can be inferred from curvature of tracks at their position closest to the beam line. To infer the position of vertices a technique called deterministic annealing in employed [62]. Deterministic annealing

estimates the position of vertices by simulating a thermodynamic system to cluster tracks together based on their estimated positions and errors closest to the beam. Once the tracks are clustered together, the position of the vertex and its errors can be estimated using the information of all the tracks in the cluster. Finally, the estimated position of the vertex can be used as an additional point in each of the tracks used in determining the vertex, resulting in improved momentum resolution. The determination of the number of primary vertices is directly related to the amount of pileup interactions, as the vertices are the location of these interactions, and is used to parameterize efficiencies that are dependent on pileup.

5.2 Muon Reconstruction

Muons are reconstructed by including the additional tagging and tracking information of the muon detectors situated around the outside of CMS. There are three primary methods of reconstructing muons in CMS know as the 'tracker muon', 'standalone muon', and 'global muon' algorithms [46]. The tracker muon algorithm uses only the momentum measurement from the tracker, propagating a candidate track through the muon system and searching within the track's position errors for track segments in the muon system. If at least one track segment is found in the muon system, the propagated track is promoted to a muon. This makes the tracker muon algorithm ideal for identifying low p_{T} muons. However, since the requirement for reconstructing a muon is finding at least one matching segment, the tracker muon algorithm suffers from higher misidentification rates at low muon p_{T}. Standalone muons are muons reconstructed using only the information of the muon system and the additional constraint that the muon points towards the measured position of the interaction region. To construct the standalone muon, an innermost segment is found and a

track is extrapolated using the angle of the track in the detector where it was found. Then, in a similar way to tracks in the silicon, additional hits are found and added to the standalone track. The standalone track is kept if at least two segments are found to make a track. Since the standalone muon algorithm requires two segments to be found it becomes inefficienct for low p_{T} muons that can stop in the steel of the muon system after the first station. The global muon algorithm uses the standalone muon algorithm as input, propagating the standalone muon track to the innermost surface of the calorimeter. A matching track in the silicon is searched for within the errors in position and energy of the propagated standalone track. If a track is found within the search window, it is combined with the muon system track. The tracking information from both detectors is then used in a global track fit, improving momentum resolution at larger muon p_{T}.

5.3 Electron Reconstruction

Electrons are reconstructed using tracker hits and ECAL deposits since electrons traverse the tracker and then stop in the ECAL. This requires first that an ECAL energy deposit, or 'cluster', with $E_{\mathrm{T}} > 4$ GeV be found in the ECAL with nearby hits in the tracker. Using the location of the shower and the beamspot as a seed, a track fit is performed propagating inwards from the EM shower's location in the ECAL. Since electrons can emit many bremsstralung photons as their trajectory bends in the magnetic field, there is a significantly larger amount of non-gaussian stochastic noise when performing a track fit. This enhancement in noise is such that a different track fitting algorithm known as a 'Gaussian Sum Filter' (GSF) [61] that allows for non-Gaussian corrections to the track to be properly accounted. Using this robust fit, the electron's track and curvature are measured in the tracker. In addition to the

electron's track, its ECAL deposit is also altered by bremsstralung, possibly creating a series of ECAL deposits located along tangents to the electron's trajectory. To account for this, the initial ECAL cluster is extended in φ to sum the additional energy of these photons into an object known as a 'SuperCluster' (SC), as shown in Figure 5.1.

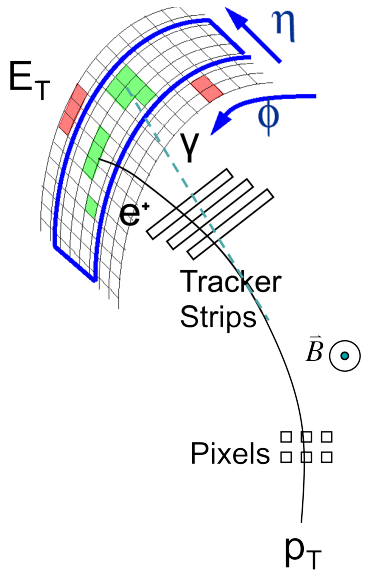

Figure 5.1: An artistic representation of the ECAL-based and tracker-based components of electron reconstruction. The supercluster is the η-φ strip containing the energy deposits of the electron and any radiated photons.

Additional requirements are made during the reconstruction of the electron that improve purity. The ratio of HCAL energy behind a SC to ECAL energy in it, $\frac{H}{E}$, being less than 0.15 is used to reject ECAL deposits that come from jets. Additionally, the reconstructed track is required to be close to the ECAL deposit by requiring $|\Delta\varphi| < 0.15$ and $|\Delta\eta| < 0.02$ between the SC and the GSF track and reduces background. Since the electron is measured by the tracker and the ECAL, the measured energy is calculated as the weighted mean of the tracker and ECAL measurements when $|E/p - 1| < 2.5\sigma_{E/p}$, where $\sigma_{E/p}$ is the total error of the ECAL energy and

tracker momentum measurements. If the E/p is not compatible with one within its errors, the ECAL energy measurement is used. Since lower p_{T} tracks bend more in the magnetic field before reaching the ECAL, the error on the momentum measurement is small and contributes more to the measurement. Since the track bends less at higher p_{T} and the momentum error is larger, the ECAL energy measurement is given a larger weight in the momentum measurement.

5.4 Photon Reconstruction

Photons are reconstructed using exactly the same ECAL clustering algorithms as for electrons. This allows simultaneous reconstruction of converted and unconverted photons without loss of efficiency due to deformations in the shower shape in φ since the clusters are formed dynamically, with the minimum size of a reconstructed photon being 5×5 ECAL crystals [63]. The choice of 5×5 being the minimum size of a photon shower is driven by the Moliére radius and each crystal being roughly 1 radius in cross section. For a perfectly centered unconverted photon most of the energy is contained in 3×3 crystals with the tails of the shower being contained in 5×5 crystals. The center of the photon shower is determined from a log-weighted energy sum given in equation 5.1:

$$x = \frac{\sum x_i \cdot W_i}{\sum W_i}, \text{ where } W_i = W_0 + \log \frac{E_i}{\sum E_j} \tag{5.1}$$

and E_i is the energy i^{th} crystal in the SC.

Normally, identification of photons is enhanced by the use of tracking information as photons that do not convert leave no signal in the silicon detectors. However, due to the large and varying material budget of the silicon tracker, photons will convert at different rates depending on η within CMS. Additionally, many of the photons produced in CMS do not convert and have no corresponding tracking information.

Consequently, there is no secondary measurement of the particle's momentum to compare to for use as preliminary rejection criteria against misreconstructions, as with electrons. It is therefore significantly harder to identify real photons since there is a large background both from jets and from electrons. This difficulty is due to the production of tracks associated with real photons through conversion and the corresponding lack of information from various subdetectors that are usually used as powerful rejectors of background. The details of identification and selection of photons are discussed in section 6.1.3.

Chapter 6

Analysis Methodology

The Zγ analysis is done for the two final states including the FSR contribution, $ee\gamma$ and $\mu\mu\gamma$, representing the decay of the Z boson into electrons and muons, respectively. The double lepton triggers are used to initially select events and the associated photon is searched for without the use of a trigger. Once the events have been selected by the HLT there is further processing that needs to take place in order to remove background events that also pass the trigger. The reducible backgrounds in each channel are removed with kinematic cuts and object identification cuts. The primary irreducible background contamination is estimated using a photon shower-shape fit and the subleading backgrounds are estimated using Monte Carlo.

6.1 Event Selection

The data taking periods during 2011 are divided into two periods by instantaneous luminosity and pileup, denoted as runs '2011A' and '2011B' comprising 2.3 fb^{-1} and 2.7 fb^{-1}, respectively, for a total of 5.0 fb^{-1}. The primary difference between these two sets is the distribution of the number of simultaneous, or pileup, interactions

that occur in the same bunch crossing as the vertex that produces the Zγ interaction. Run 2011 A had a mean vertex multiplicity of 5.1 pileup vertices per bunch crossing, Run 2011 B had a mean of 8.4 pileup interactions per bunch crossing. However, the selections used for leptons and photons in the Zγ analysis are constructed such that they do not depend on the number of primary vertices in an event. The efficiencies of selection cuts are derived for each run period individually and are combined statistically, event-by-event, to represent the efficiency seen in the full 5 fb^{-1} 2011 dataset.

6.1.1 Trigger Requirements

The $ee\gamma$ final state is selected by using unprescaled electron triggers with the lowest available p_T thresholds. The isolated double electron triggers have asymmetric p_T thresholds of 17 GeV and 8 GeV on the leading and trailing electrons respectively. The trigger-level isolation requirements of both the leading and trailing electron candidates were made more stringent in 2011B data taking to increase purity due to the increase in combinatorial background coming from pileup. The $\mu\mu\gamma$ events are triggered using the same general strategy as for electron final states.

The double muon trigger does not require muon candidates to be isolated in the detector, and the only change throughout the 2011 data taking period was the change of the muon candidate p_{T} thresholds. For the majority of the run, the lepton threshold for the leading muon candidate was 13 GeV and 8 GeV for the trailing one. Smaller portions of the muon data were triggered with a symmetric dimuon trigger with 7 GeV $_{\mathrm{T}}$ thresholds and an asymmetric trigger with an increased p_{T} threshold of 17 GeV on the leading muon. These triggers represent 216 pb^{-1} and and 880 pb^{-1} of the total dataset, respectively.

6.1.2 Electron Selection

SuperClusters (SC), deposits of electromagnetic energy associated with electrons are required to be inside the η coverage of the tracker, $|\eta| < 2.5$. The crack region between barrel and endcap sections of the ECAL, $1.4442 < |\eta| < 1.566$, is also excluded since energy reconstruction and background rejection are degraded in this region.

The width of the SC in η is characterized by the quantity $\sigma_{i\eta i\eta}$, defined as:

$$\sigma^2_{\mathrm{i}\eta\mathrm{i}\eta} = \frac{\sum (\eta_\mathrm{i} - \bar{\eta})^2 w_\mathrm{i}}{\sum w_\mathrm{i}},\ \bar{\eta} = \frac{\sum \eta_\mathrm{i} w_\mathrm{i}}{\sum w_\mathrm{i}},\ w_\mathrm{i} = \max\left(0, 4.7 + \log(E_\mathrm{i}/E_{5\times5})\right), \tag{6.1}$$

where the sum runs over the 5×5 crystal matrix around the most energetic crystal in the SC. The SC width is required to be narrow, consistent with the profile of an electromagnetic shower. The reconstructed electron track is required to have no missing hits to reduce background from combinatorics. Early photon conversions can also be reconstructed as electrons, since they produce electron pairs that make it to the calorimeter. These conversions are rejected based on the distance, |dist|, and angle, $|\cot \Delta\vartheta|$, to partner tracks indicative of electron pair production from photons. To select energetic electrons, indicative of electroweak boson production, each selected electron is required to have a transverse momentum $p_\mathrm{T} > 20$ GeV.

The production of two electroweak bosons in an event requires a significant transfer of energy between partons from the colliding protons. This results not only in energetic lepton tracks originating from the vertex but also a larger amount of lower energy tracks as well. To select electrons coming from the interation vertex, the transverse distance of closest approach, or impact parameter, d_0 to the event's primary vertex[1], PV, is required to be less than 0.02 cm. Additionally, the z component of the impact parameter, d_z, is required to be less than 0.1 cm. These two cuts together

[1]The reconstructed vertex with the largest scalar p_T sum of associated tracks.

ensure that the reconstructed electron is consistent with a vertex from a high energy interaction.

The rate of jets being misreconstructed as electrons is reduced by requiring that the reconstructed electrons have little adjacent hadronic activity indicated by signals in the tracker, ECAL, or HCAL. The energy in the isolation regions is calculated by summing in the tracker and ECAL in a $\Delta R = \sqrt{\Delta\varphi^2 + \Delta\eta^2}$ cone with radius 0.3 that has a veto region, where energy is not added to the sum. The veto region is the size of two crystals in $\Delta\eta$ and a five crystal strip in $\Delta\varphi$ as to not include bremsstrahlung in the isolation sum. The energy in the HCAL is summed in a solid cone with $\Delta R < 0.3$. To remove excess energy associated to pileup vertices, the average energy density per unit area deposited in the calorimeters ρ is calculated using the FastJet algorithm [64]. To subtract off this average contribution from pileup inside the cone, ρ is multiplied by the isolation cone area $\pi\Delta R^2$ and subtracted from the summed energy in the isolation region. To implement the cut, the pileup corrected sum of tracker, ECAL, and HCAL activity normalized to the electron p_{T} is required to not exceed 0.053 if the electron is in the ECAL barrel and 0.046 in the ECAL endcap.

In addition to the selection of $Z \to ee$ events for the primary result, electron samples are also selected with other criteria to determine the difference in shower shape between data and MC for real electromagnetic showers. These selection criteria comprise two working points, WPs, that select electrons with 85% and 80% signal efficiency, called respectively WP85 and WP80. WP85 is used as the primary selection criteria in the Zγ analysis and is tighter than the isolation criteria imposed at the trigger level.. WP80 is used to select electrons with more stringent requirements 'tag' possible Z events, allowing a systematic study of the other Z electron. This study examines the shower shape distribution of the other Z electron, which was selected with the $\sigma_{i\eta i\eta}$ requirement removed. The summary of the criteria defining

these working points is given in Table 6.1.

	WP85		WP80	
	Barrel	Endcap	Barrel	Endcap
$\Delta\varphi_{\text{vtx}}$	0.039	0.028	0.027	0.021
$\Delta\eta_{\text{vtx}}$	0.005	0.007	0.005	0.006
$\lvert\cot\Delta\vartheta\rvert$	0.02	0.02	0.02	0.02
$\lvert\text{dist}\rvert$	0.02	0.02	0.02	0.02
$\sigma_{i\eta i\eta}$	0.01	0.031	0.01	0.031
Combined relative isolation	0.053	0.042	0.04	0.033

Table 6.1: Selection criteria for the WP80 and WP85 electron candidates in the ECAL barrel and ECAL endcap.

The WP85 selection efficiency is estimated from data using the 'tag-and-probe', or T&P, method [46]. This method is based on a simultaneous fit of signal and background distributions of electron pairs where one electron, the 'tag', passes full identification criteria and the other, the 'probe', either passes or fails the selection criterion. These efficiencies are measured differentially in p_{T}, η, and vertex multiplicity in the data and MC with differences arises from the calibration of the ECAL, which evolves in time with radiation dose. These differences are corrected for in the MC by applying a per electron weight calculated as the ratio of efficiency in data to that in MC. The efficiencies in MC agree with those measured from data to better than 3% and the the scale factors used can be seen in Figure 6.1 for Run 2011 A and 6.2 for Run 2011 B.

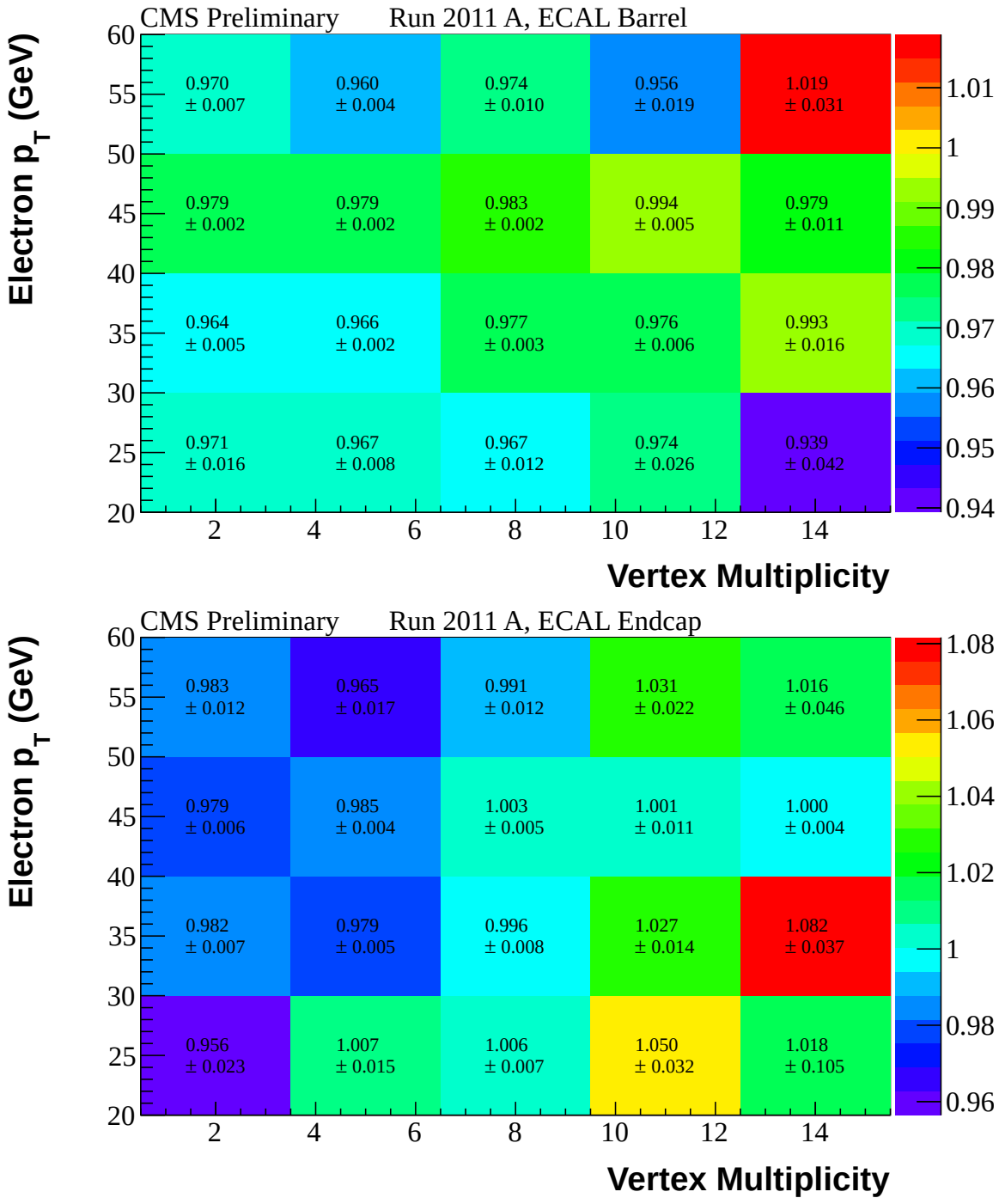

Figure 6.1: Electron efficiency scale factors for the 2011 A run period.

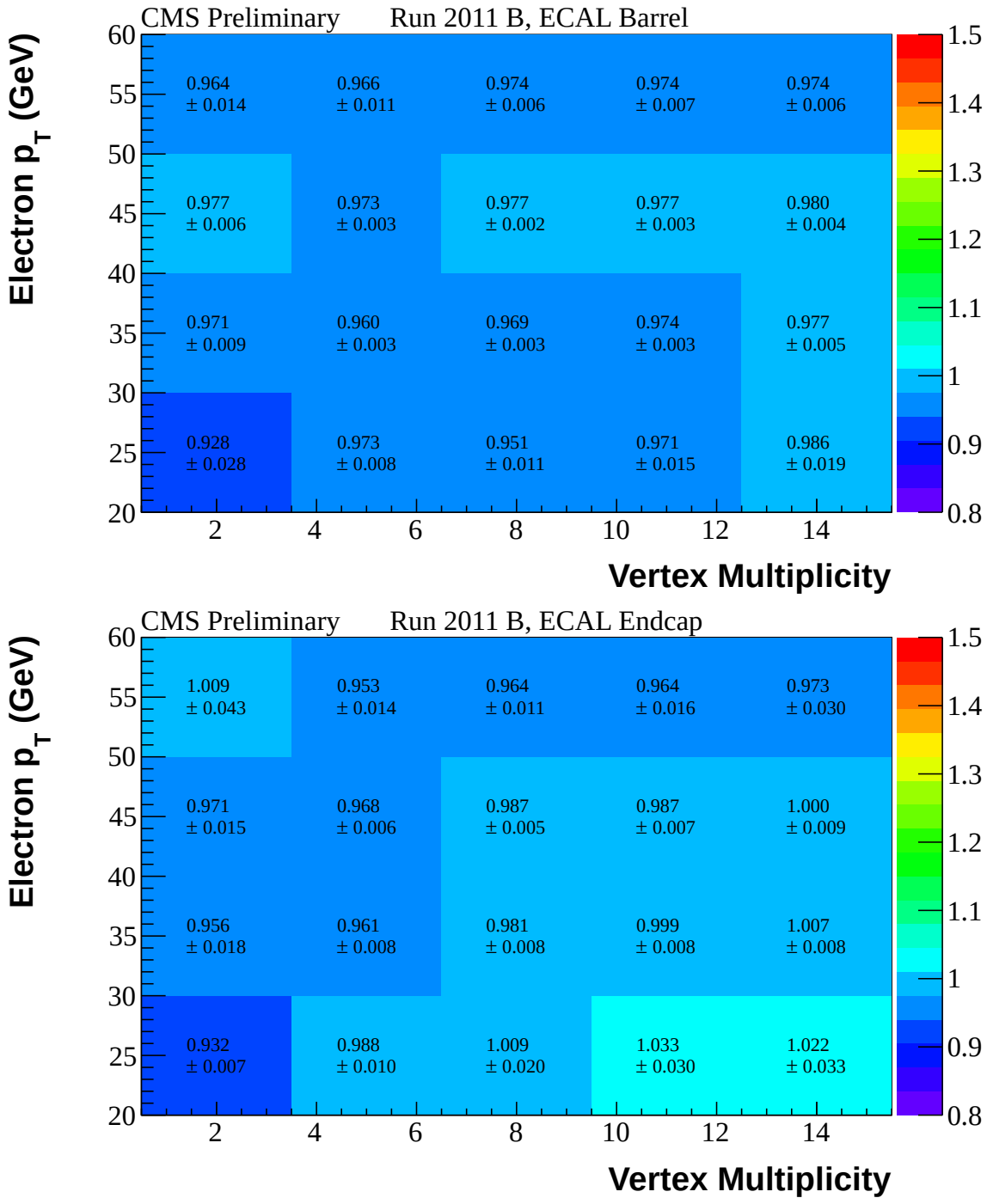

Figure 6.2: Electron efficiency scale factors for the 2011 B run period.

6.1.3 Photon Selection

Photon candidates are reconstructed from superclusters and are required to have $E_{\mathrm{T}} > 15$ GeV and be within the η converage of the ECAL. The photon ID is implemented following the same methodology as used in the 2010 CMS Vγ measurement[2] [65]. As with the electron ID, the photon ID focuses on reducing jet backgrounds by using shower shape criteria and pileup corrected isolation cuts. Misreconstructed photons from jets are primarily caused by jets that hadronize into highly collimated sprays of π^0s that decay into two photons. Since the photons from these π^0s have a small opening angle and there is little track activity since the jet hadronized into neutral hadrons, the resulting jet looks almost exactly like a single photon. Furthermore, there is no additional discriminating power coming from consistency with heavy resonance production, as in lepton identification. The rate of jets being misreconstructed as photons that pass all selection criteria is not well known since the hadronization processes producing EM-rich jets are not well known. Therefore, a background estimate, Section 6.2, using data sidebands must be implemented and the photon ID is designed with ease of implementation in mind.

To reject electrons that emit too much bremsstralung to be recovered by the GSF algorithm or that have lost hits in the strip tracker, pixel seeds are used to veto electrons that fake photons. Pixel seeds are tracks fit using 2 or 3 pixel hit and the constraint of the beamspot location. If the reconstructed photon's shower is kinematically consistent with the pixel seed, the photon is flagged and this flag may be used as a veto.

As for the lepton ID, the photon identification is pileup corrected. However, a different pileup correction procedure is implemented in order to maintain efficiency and minimize fake-rates since the isolation veto regions used for photons vary as a

[2] A 36 pb^{-1} result also with considerable involvement from the author.

Description	criterion
Kinematics	$E_{\mathrm{T}} > 15$ GeV
	$1.4442 < \lvert\eta\rvert < 1.566$ and $\lvert\eta\rvert < 2.5$
Ratio of HCAL to ECAL energy (H/E)	< 0.05
Shower width, $\sigma_{i\eta i\eta}$	< 0.011 in EB and < 0.030 in EE
Photon has pixel seed	False for both EB and EE photons
Tracker Isolation	$I_{\mathrm{trk}} - 0.001 \cdot E_{\mathrm{T}} - \rho \cdot A_{eff}^{\mathrm{trk}} < 2.0$
ECAL Isolation	$I_{\mathrm{ECAL}} - 0.006 \cdot E_{\mathrm{T}} - \rho \cdot A_{eff}^{\mathrm{ECAL}} < 4.2$
HCAL Isolation	$I_{\mathrm{HCAL}} - 0.0025 \cdot E_{\mathrm{T}} - \rho \cdot A_{eff}^{\mathrm{HCAL}} < 2.2$

Table 6.2: Photon identification and isolation criteria. The $\sigma_{i\eta i\eta}$ variable is used in a fit to determine the estimated fraction of jets reconstructed as photons which pass all cuts. Effective areas, A_{eff} for EB and EE are given in Table 6.3.

function of sub-detector. For all isolation criteria the outer edge of the cone is defined to be $\Delta R < 0.4$. The tracking isolation sum is calculated by vetoing energy within a cone of $\Delta R < 0.05$. However this is not expected to depend much on pileup since the tracking isolation is calculated using only those tracks associated with the primary vertex of the event. ECAL isolation energy is summed by vetoing a rectangular region of size $\Delta\eta \times \Delta\varphi = 0.04 \times 0.40$ to minimize efficiency loss from photon conversions, as well as an inner veto cone of $\Delta R < 0.04$ to remove the super cluster. HCAL isolation is performed with a central veto cone of $\Delta R < 0.15$, to decorrelate the HCAL isolation cut from the cut on the ratio of hadronic to electromagnetic energy immediately around the SC. A_{eff}, defined as 'effective area', is calculated by determining the slope of the quantities $\frac{I_{\mathrm{trk}}}{\rho}$, $\frac{I_{\mathrm{ECAL}}}{\rho}$, and $\frac{I_{\mathrm{HCAL}}}{\rho}$, the ratios of a specific isolation to the average energy density ρ calculated from the FastJet package. The values of A_{eff} are tabulated for all three isolation criteria separately for barrel and endcap in Table 6.3. The tracking isolation has a small effective area, 0.0167 cm^2 (EB) and 0.032 cm^2 (EE), and hence a small dependence on pileup as expected. Once the effective areas are determined, the corrected isolation for a subdetector is calculated as Iso $- \rho \cdot A_{eff}$. The cuts are summarized in Table 6.2.

Isolation	barrel	endcap
Tracker	0.0167	0.032
ECAL	0.183	0.090
HCAL	0.062	0.180

Table 6.3: A_{eff} used for PU correction for photon selection for barrel and endcap, respectively.

The efficiency of the H/E, $\sigma_{i\eta i\eta}$, and isolation requirements are determined using electron based tag-and-probe, where the probe electron's SC is matched to the corresponding reconstructed photon. The tag electron is required to pass WP80 selection criteria, the pixel seed veto requirement is dropped for the probe and the resulting efficiency scale factors are given in Figures 6.3 for Run 2011 A and 6.4 for Run 2011 B.

The efficiencies for the pixel seed veto are calculated using $Z \to \mu\mu\gamma$ FSR events, where the tags are dimuons off the Z peak and probes are reconstructed photons close to one of the muons where the Z+Jets background is minimal. Using this pure sample of photons the pixel seed veto efficiency is extracted from data and equivalently in MC. Again, a scale factor is constructed and applied to the MC as a correction factor, shown in Table 6.4.

	Data (%)	MC (%)	Data/MC (%)
	Run 2011 A		
EB	97.2 ± 0.3	97.8 ± 0.2	99.4 ± 0.3
EE	90.0 ± 0.9	91.0 ± 0.5	98.9 ± 0.9
	Run 2011 B		
EB	96.1 ± 0.4	97.1 ± 0.2	99.0 ± 0.4
EE	87.3 ± 1.3	89.3 ± 0.5	97.8 ± 1.6

Table 6.4: The photon pixel seed efficiencies as derived from photon FSR tag-and-probe.

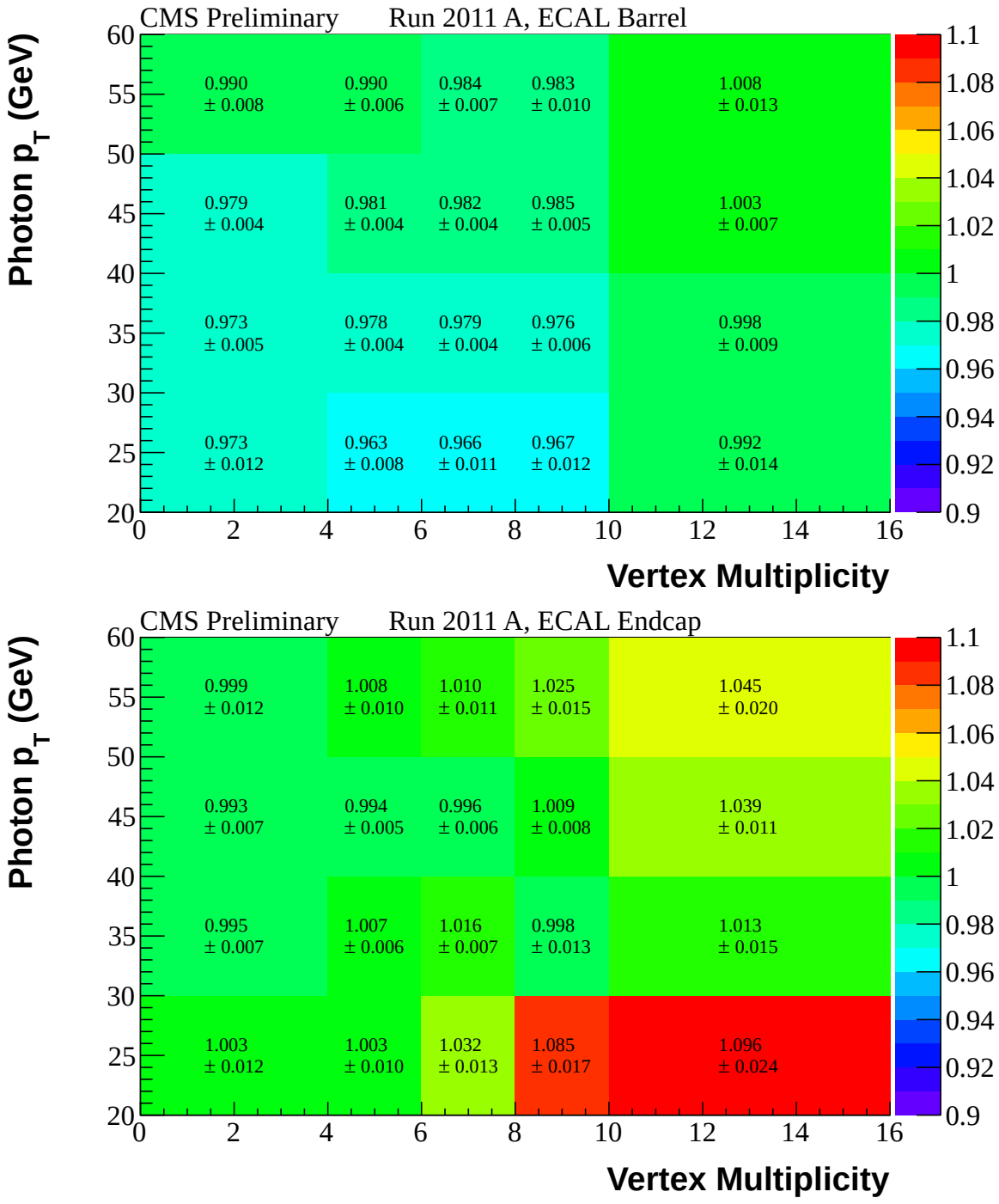

Figure 6.3: Photon efficiency scale factors for the 2011 A run period.

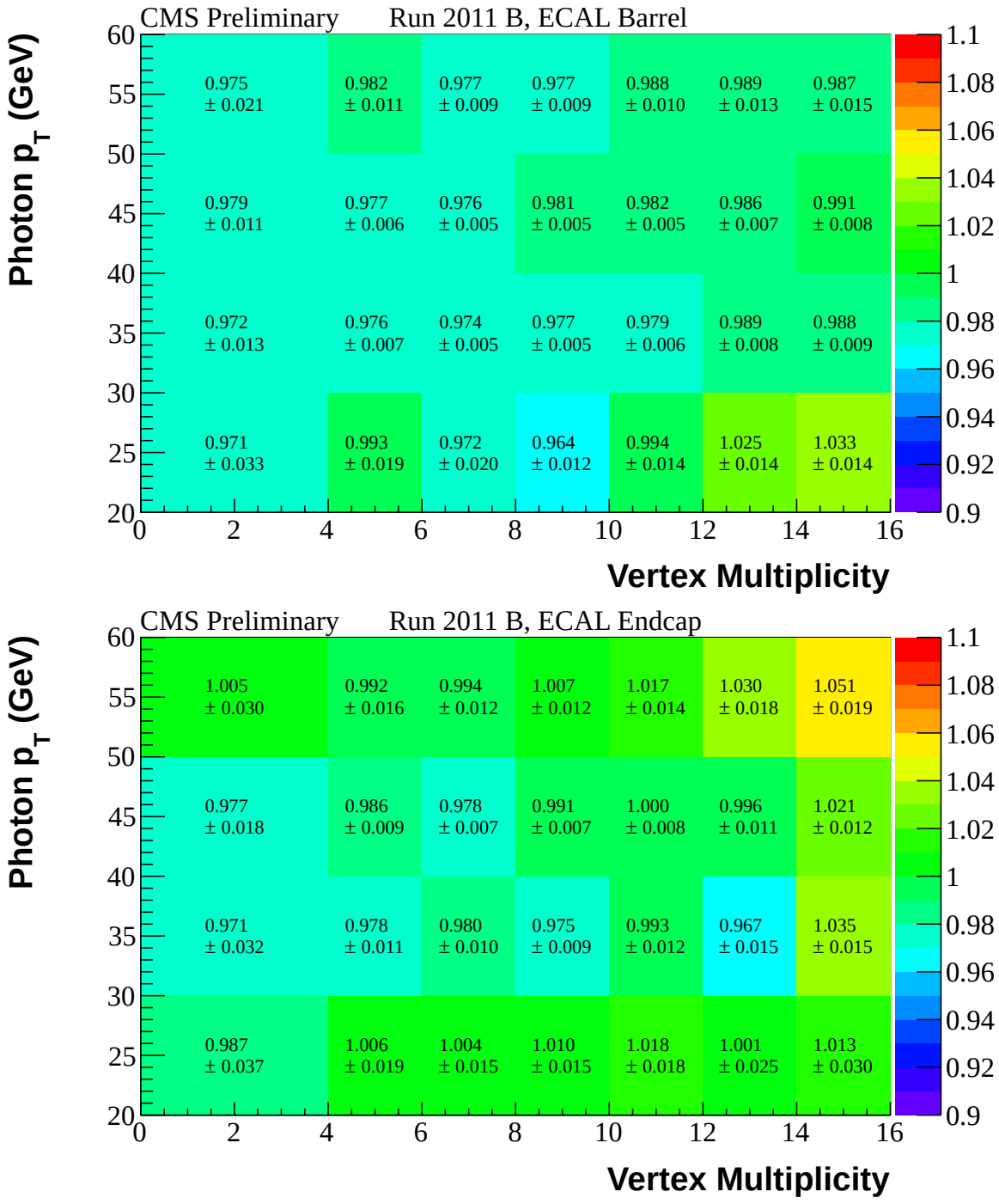

Figure 6.4: Photon efficiency scale factors for the 2011 B run period.

6.1.4 Muon Selection

The general technique for electron selection is also applied to muon selection, with appropriate changes since all muon reconstruction information is from tracking detectors. In particular, instead of matching extrapolated variables between the ECAL and tracker, the goodness of fit of the global muon track and consistency with a high quality reconstructed track in both the muon system and silicon tracker are used as identification requirements. The globally reconstructed muon track is required to have at least one hit in the pixel tracker, eleven hits in the silicon strip tracker and at least one hit in the muon system. Moreover, the track is required to have a χ^2 value of the global track fit less than ten. The muon is also required to be found by the tracker muon algorithm and have at least two segments matched to the propagated track. The same PV matching criteria are applied to muons as done for electrons, assuring that the muons in the pair originate from the primary vertex.

Description	criterion
Kinematics	$p_{\mathrm{T}} > 20$ GeV and $\lvert\eta\rvert < 2.4$
Number of pixel hits	> 0
Number of tracker hits	> 10
χ^2/n.d.f of the global muon fit	< 10
Number of muon hits	> 0
Number of chambers with matched segments	> 1
Vertex d_0	< 0.1 cm
Vertex d_z	< 0.02 cm
Relative Combined Isolation	< 0.1

Table 6.5: Muon identification and isolation requirements. The loose selection is used to identify muons from Z candidates, while the tight selection is used for the W candidates.

Secondary muons from b-jets and decays of pions are rejected by requiring that the reconstructed muon is isolated from surrounding hadronic activity. As for electrons, the isolation energy for tracker, ECAL, and HCAL is summed in a cone with $\Delta R <$

0.3, and the veto area is a cone with $\Delta R < 0.1$ about the muon's track, to remove the minimum ionizing radiation deposition in the calorimeters. The ratio of the pileup corrected isolation sum to the muon p_{T} is required to be less than 0.1. The cuts are summarized in Table 6.5.

$\mathrm{Z}\rightarrow \mu\mu$ decays are used to measure both trigger and selection requirements in both data and MC simulation. Again, the MC is scaled event by event to match the measured efficiency in the data and the muon efficiencies used are summarized in Figure 6.5.

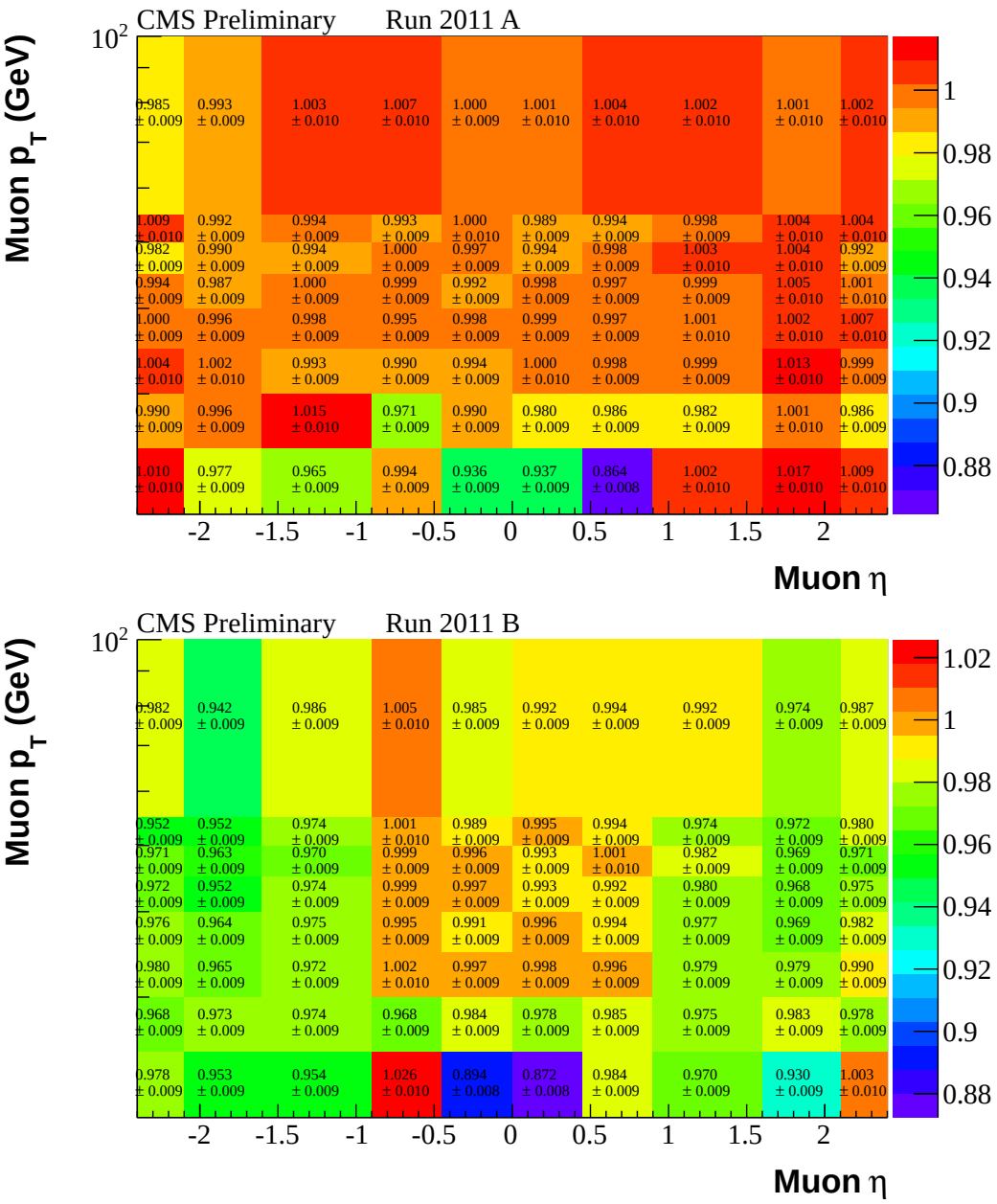

Figure 6.5: Muon efficiency scale factors for the 2011 A and B run periods.

6.1.5 Event Topology

In order to select Zγ events and make a reasonable comparison with theory, there are cuts in addition to the requirement of two high p_{T} leptons and an energetic photon. The Z candidate, formed from the two leptons, is required to have an invariant mass greater than 50 GeV to suppress low mass Drell-Yan and remove the singularity at zero mass[3]. This results in a more numerically stable prediction from the MC and a more pure sample of on-shell Z candidates with which to compare. The theoretical soft singularity of the emitted real photon is controlled by the requirement that the photon E_{T} be larger than 15 GeV. However, there still exists a singularity when the photon is collinear with one of the final state leptons. This is controlled by requiring the minimum ΔR between the lepton and the photon to be less than 0.7.

6.2 Background Estimation

The shower shape variable $\sigma_{i\eta i\eta}$ is used to separate the genuine photons from misidentified jets by making an extended maximum likelihood two-component fit of signal and background templates to data.

The signal component shape is obtained from MC and corrected for the difference between data and MC simulation in an electron control sample obtained from $Z \to ee$ events. This correction is small and is of the order of one percent. The background component shape was derived from data.

Both signal and background templates are obtained in bins of photon p_{T}: $15-20$ GeV, $20-25$ GeV, $25-30$ GeV, $30-35$ GeV, $35-40$ GeV, $40-60$ GeV, $60-90$ GeV, $90-120$ GeV, and $120-500$ GeV. Template shapes for photons reconstructed in the barrel are made separately for each photon p_{T} bin.

[3]Light leptons and quarks are usually considered as massless in most MC programs.

6.2.1 Signal Component Shape

The signal shape is obtained from a MadGraph of Wγ events. The simulation of the electromagnetic showers in MC is cross checked against the data using Z$\rightarrow$ ee events. These events are selected by the di-electron triggers described in Sec. 6.1.1. Events are further required to have at least two electron candidates with $p_{\mathrm{T}} > 20$ GeV and pass WP80 selection criteria described in Sec. 6.1.2 but without the $\sigma_{i\eta i\eta}$ requirement. Both electron candidates are required to be identified in the ECAL fiducial volume and have invariant mass between 60 and 120 GeV. One of the electron candidates, a tag, is required to pass the tight trigger criteria of the di-electron trigger, while no trigger requirements are applied on the other electron candidate, a probe. The purity of this selection is calculated to be 99% for both barrel and endcap regions.

The comparison of the $\sigma_{i\eta i\eta}$ distributions for the probe in data and MC indicates that the mean of the $\sigma_{i\eta i\eta}$ distribution in data is smaller than in simulation by 0.9×10^{-4} (2.0×10^{-4}) for barrel(endcap) and corresponds to 1%.(0.8%) of the average $\sigma_{i\eta i\eta}$ values in MC, which are corrected for the observed shift. The comparison of electron showers in data to those in MC is shown in Figure 6.6. The shift is is used to estimate a systematic error, discussed in Section 6.4.

6.2.2 Background Component Shape

The background templates were made from jet-enriched selected events. Photon candidates in these events are required to pass the photon selection criteria described in Sec. 6.1.3, except for the $\sigma_{i\eta i\eta}$ requirement and the tracker isolation criterion Iso_{TRK} which is altered to select a sideband:

- 2 GeV $< Iso_{TRK} - 0.001E_T^{\gamma} - 0.0167\rho < 5$ GeV for EB
- 2 GeV $< Iso_{TRK} - 0.001E_T^{\gamma} - 0.0320\rho < 3$ GeV for EE

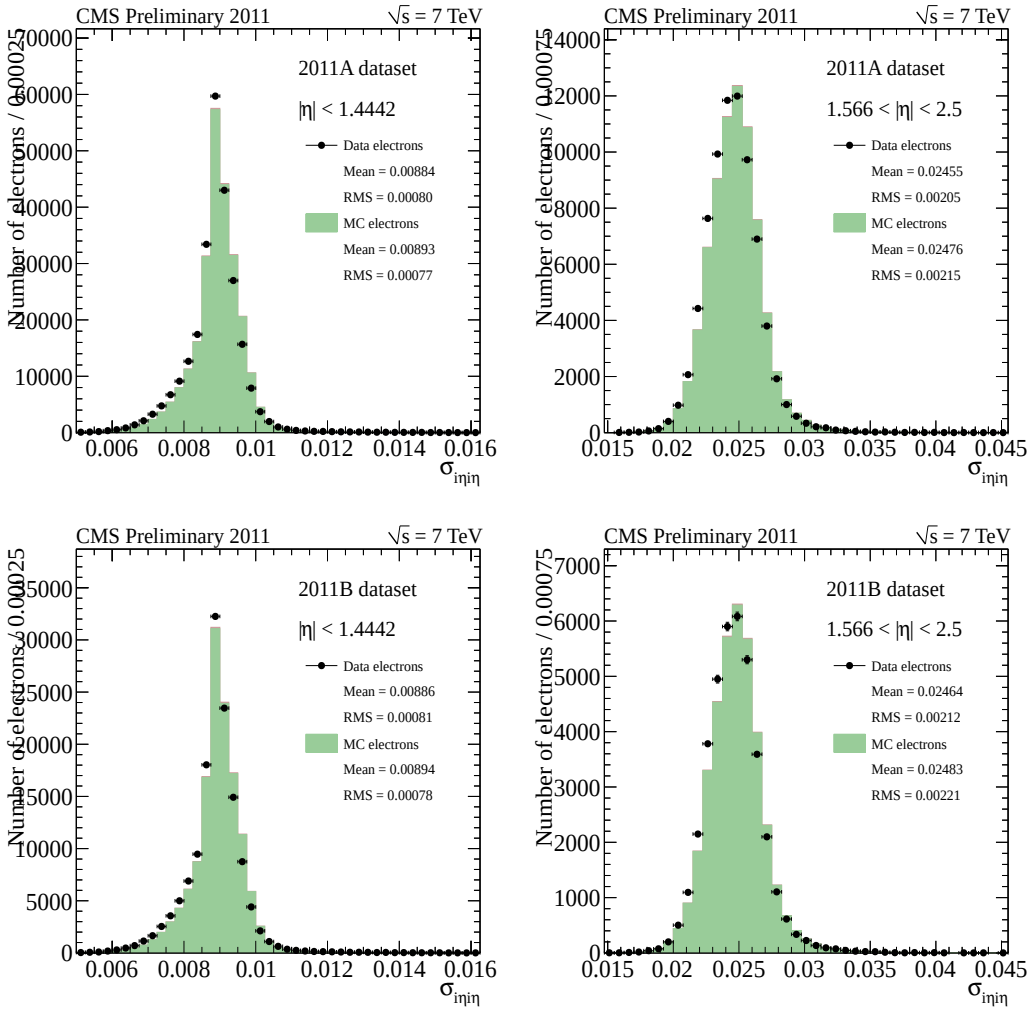

Figure 6.6: The $\sigma_{i\eta i\eta}$ distributions for barrel (left) and endcap (right) for Runs 2011 A and B. The difference of mean values between MC and data are accounted for by shifting the simulation signal shapes.

This requirement ensures that the contribution from genuine photons is negligible, and keeping the isolation requirements close to those for photon selection criteria allows selecting jets with large electromagnetic fraction that have properties similar to those of genuine photons. We also observe that in simulated jet events the $\sigma_{i\eta i\eta}$ is found largely uncorrelated with isolation requirement, so the background shape observed for photon-like jets with the inverted tracker isolation should be the same

as that for isolated photon-like jets.

6.2.3 Two Component Fit

The $\sigma_{i\eta i\eta}$ distribution in data are fitted to the function:

$$f(\sigma_{i\eta i\eta}) = N_S S(\sigma_{i\eta i\eta}) + N_B B(\sigma_{i\eta i\eta}), \tag{6.2}$$

where N_S and N_B are the estimated number of signal and background candidates, $S(\sigma_{\mathrm{i}\eta\mathrm{i}\eta})$ and $B(\sigma_{\mathrm{i}\eta\mathrm{i}\eta})$ are the signal and background template components. Used templates are smoothed with kernel density estimation [66] or direct interpolation, in the case of high statistics templates, to allow for unbinned fits of the $\sigma_{i\eta i\eta}$ distribution of selected photons to be performed.

The fit is performed by using a unbinned extended maximum likelihood (extended-ML), by minimizing:

$$\mathcal{L} = -\ln L = (N_S + N_B) - \sum_{\mathrm{i}=1}^{n} N \ln(N_S S(\sigma_{i\eta i\eta}) + N_B B(\sigma_{i\eta i\eta}). \tag{6.3}$$

N_S and N_B are the best fit number of signal and background events in a given p_{T} bin. S and B are the shapes of the corresponding unbinned templates in the p_{T} bin. N is the total number of data events in the given p_{T} bin. Figure 6.7 shows the result of a typical template fit.

6.3 Comparison of Simulation to Data

The resulting 2D invariant mass distributions are summarized in Figure 6.8, demonstrating the ISR and FSR contributions to the Zγ final states.

Figure 6.9 demonstrates the distributions after full selection for the electron channel and Figure 6.10 for the muon channel. The plotted quantities demonstrate that

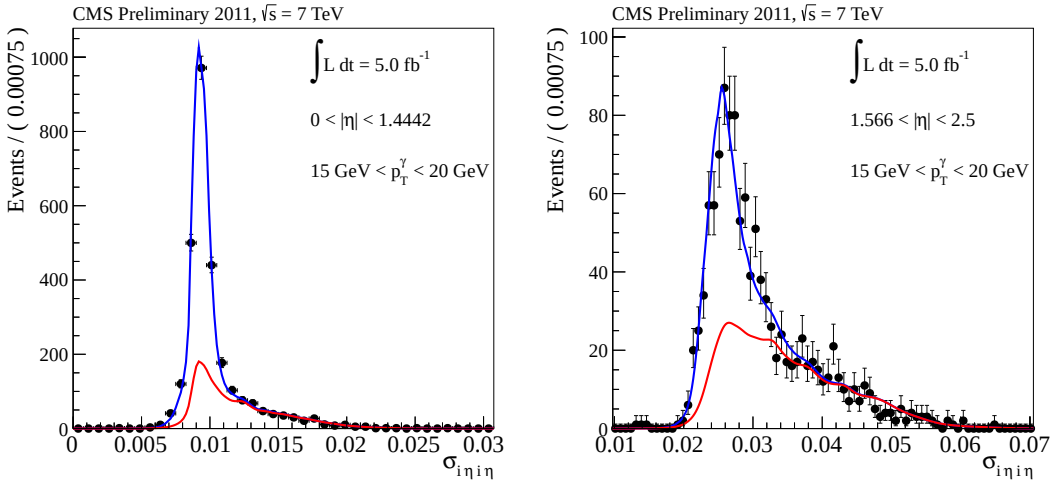

Figure 6.7: An example template fit in the 15-20 GeV bin in the barrel (left) and endcap (right).The signal distribution is indicated by the blue line and the background is indicated by the red line. The full set of template fit results may be found in Appendix A.

the signal monte carlo describes the expected signal well, after corrections to the background are made. Both the shapes and normalization of distributions agree well between data and MC. The background Z($\ell\ell$)+Jets MC is reweighed in yield and photon p_{T} shape to reflect data derived background estimates, the reweighing is applied for all projections of the background MC.

Excellent agreement is found between data and MC predictions after applying data-derived corrections to the efficiency and background yields. In particular, the predicted photon p_{T} spectrum is found to agree with data over a range of 485 GeV for both electron and muon channels. The data to MC disagreement in the dilepton mass spectra is a known effect since additional final state EM radiation is turned off in the signal MC to avoid double counting of the signal. This is reflected in the poor modeling of the low side tail of the dilepton peak but otherwise has no effect aside from jets in the signal MC having a systematically smaller EM fraction than other samples.

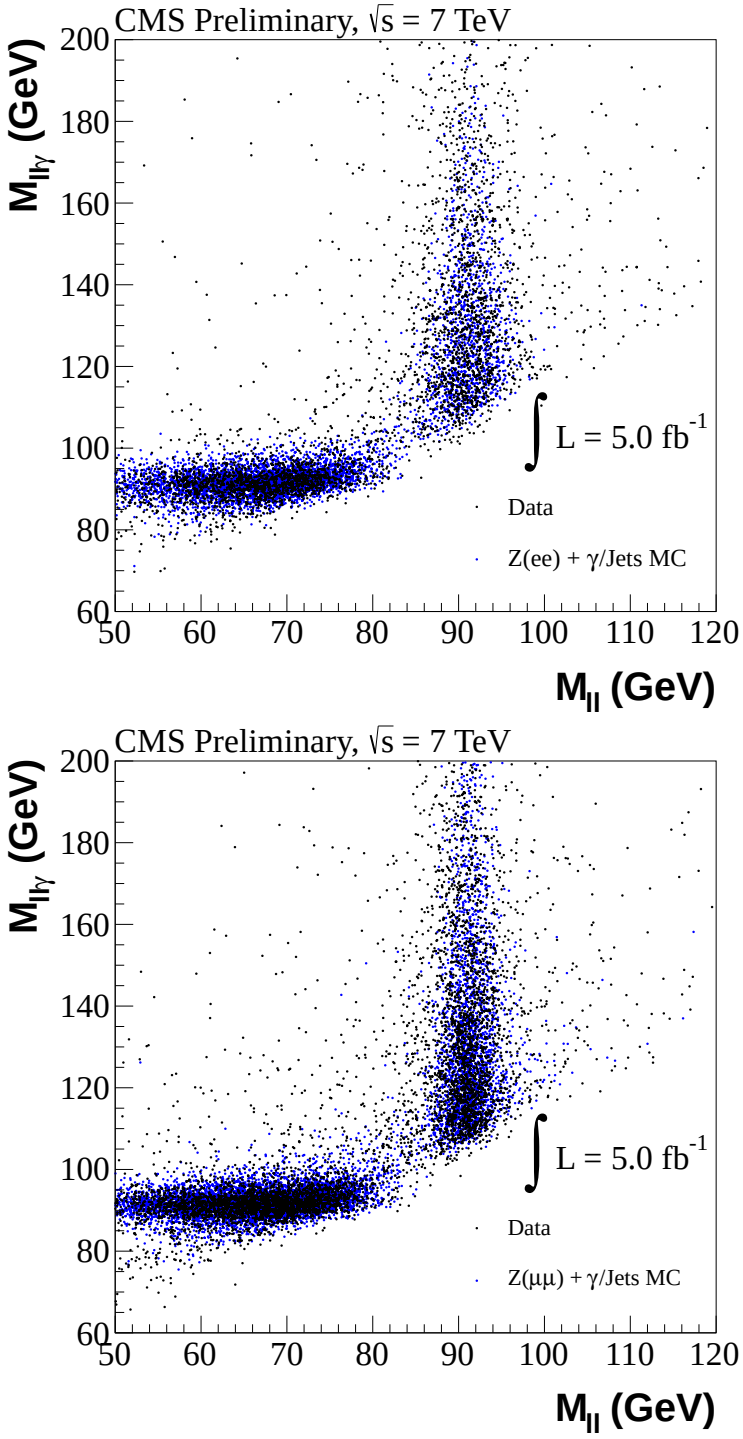

Figure 6.8: Dilepton invariant mass vs. $\ell\ell\gamma$ invariant mass for the $ee\gamma$ channel (top) and $\mu\mu\gamma$ channel (bottom). The ISR dominated and FSR dominated regions can be clearly seen as vertical and horizontal bands, respectively.

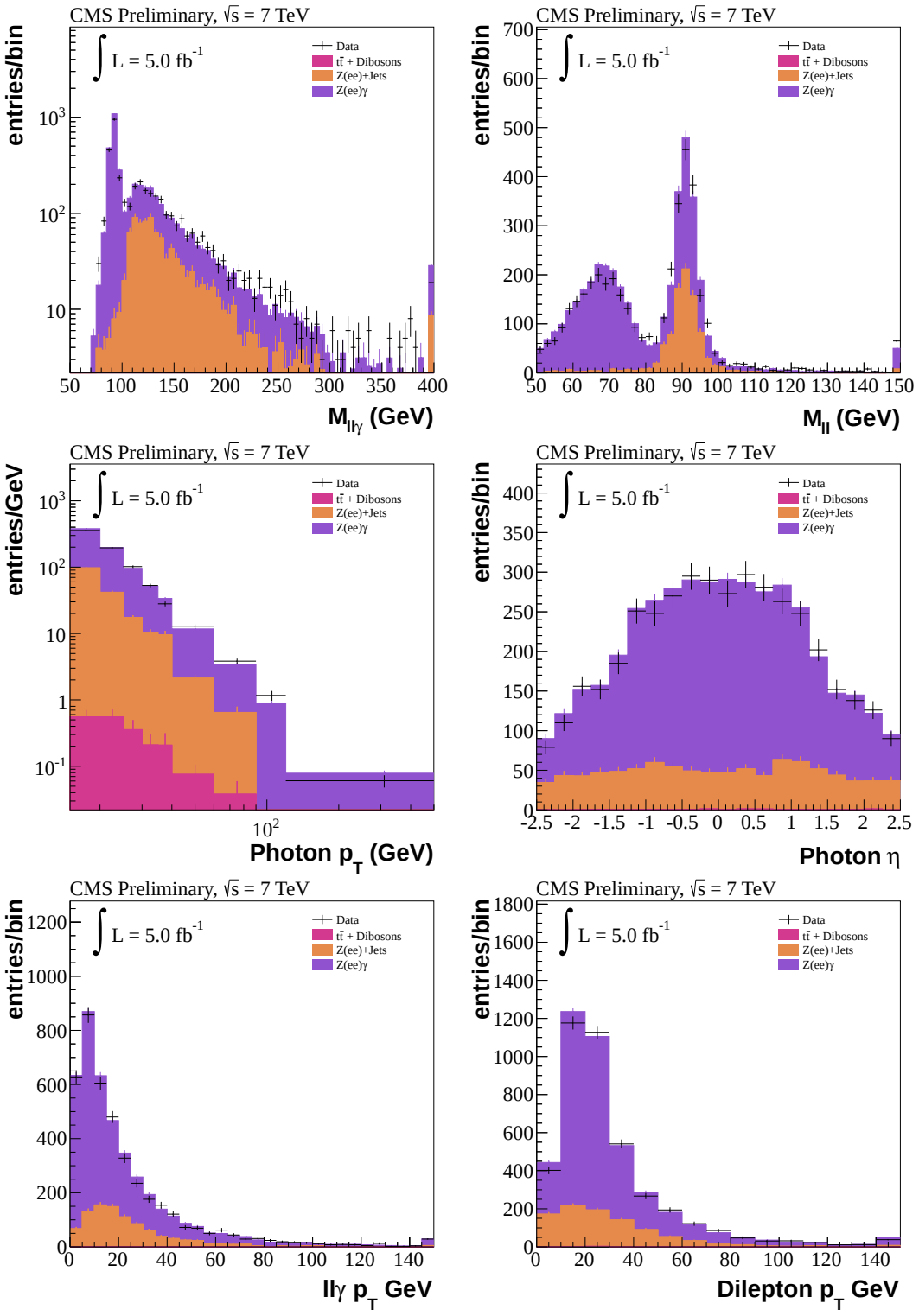

Figure 6.9: The fully selected distributions for the $ee\gamma$ channel.

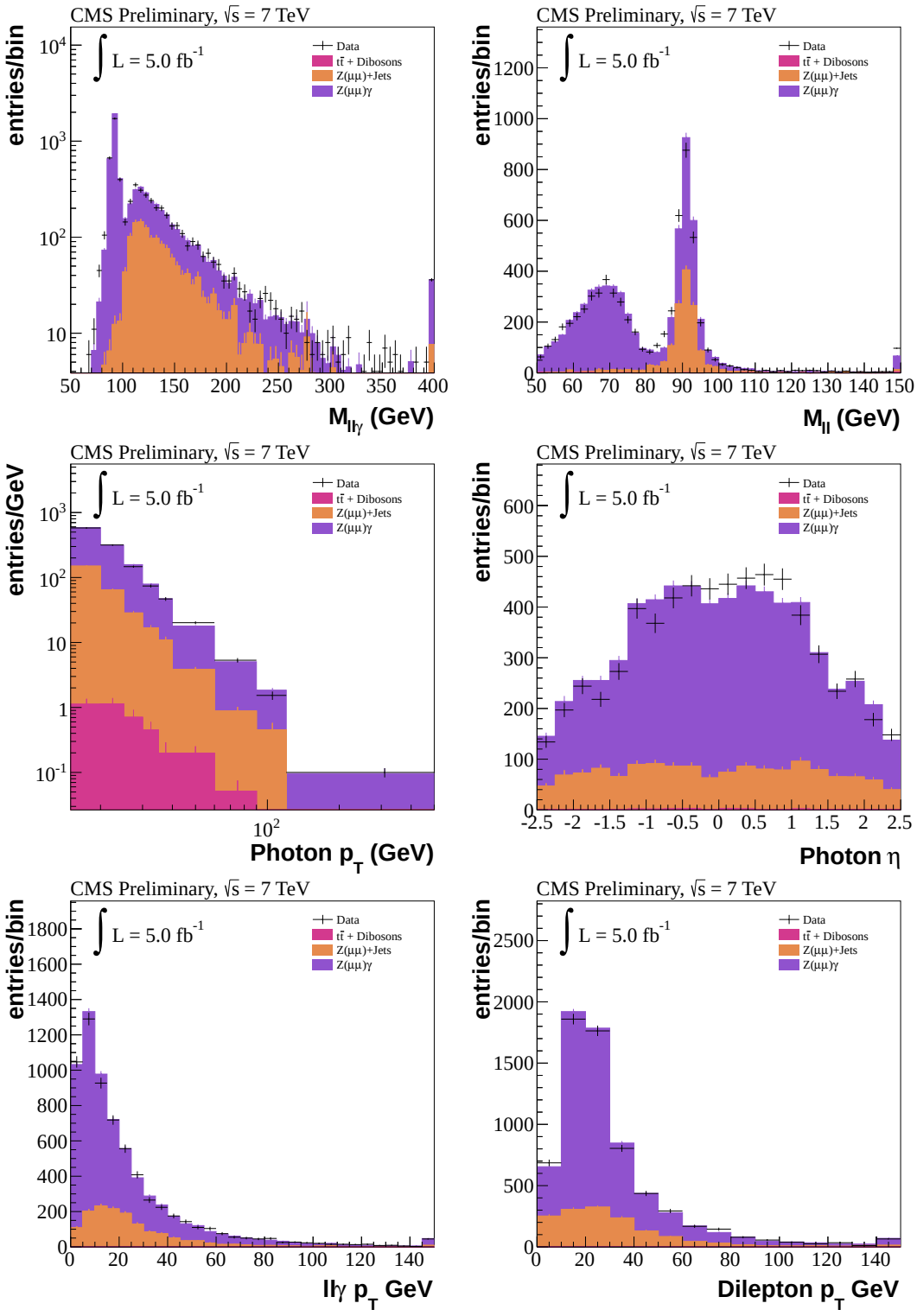

Figure 6.10: The fully selected distributions for the $\mu\mu\gamma$ channel.

6.4 Systematic Uncertainties

6.4.1 Luminosity

The total integrated luminosity is experimentally determined for the full 2011 dataset using a pixel cluster counting technique, effectively determining the cross section for a single pixel cluster [67]. To calculate the luminosity, the total beam current, per-bunch proton population, and size of the luminous region at the CMS interaction point must be taken into account, and then the number of pixel clusters per zero bias trigger are counted. Late arriving particles and activation of the CMS detector material can cause spurious pixel clusters that must be accounted for and subtracted off. The uncertainty in this subtraction term gives rise to part of the systematic uncertainty on the luminosity. The another large part of the luminosity uncertainty comes from variations in the experimentally measured size of the luminous region. The total systematic uncertainty on the luminosity was found to be 2.2% for the full 2011 dataset, with the majority of the certainty coming from the two given sources. This uncertainty is applied as a flat systematic uncertainty to the cross section and is also applied to signal and background contributions determined purely from MC.

6.4.2 Electron and Photon Energy Scales

The electron energy scale in data is varied by 0.5% to take into account the contribution from mis-calibration of the ECAL detector. For photons the energy scale is varied by 1% in the ECAL barrel and 3% in the endcaps. To estimate the systematic effect on the measured cross section the number of signal events is re-evaluated for each systematic variation since the scale variations affect the background subtraction templates. In the case of the variation of the photon energy scale, the background subtraction is performed with signal and background templates that have been appro-

priately modified. This ensures that migrations of photons and misidentified photon-like jets across the low photon p_{T} cut boundaries are properly accounted for when calculating this systematic uncertainty. The migrations from this effect are of order 3%.

6.4.3 Photon and Electron Energy Resolution

The combined acceptance times efficiency, $A \cdot \varepsilon$, is determined from MC simulation of the Zγ signal and is affected by the electron and photon energy resolution by way of migration of events in and out of acceptance. The electron energy resolution is determined in data using Z$\rightarrow ee$ events and calibrating to the Z pole, including the effect of the finite width of the Z. To estimate the effect of the electron resolution on $A \cdot \epsilon$ each electron candidate's energy is randomly smeared by the energy resolution determined in data then standard selection is applied.

The photon energy resolution is determined simultaneously with the photon energy scale in data. The systematic effect of the photon resolution on $A \cdot \epsilon_{MC}$ is calculated by deterministically rescaling the reconstructed photon energy in MC simulation to match that in data using the parton-level photon energy.

6.4.4 Pileup Modeling

The number of pileup interactions per event is estimated from data using a convolution procedure that extracts the estimated pileup from the per-bunch instantaneous luminosity recorded by the luminosity monitors. This methodology requires the total inelastic pp scattering cross section, 68 ± 3.4 mb, to estimate the number of pileup events in a given bunch crossing. The MC samples used to compare with the data are reweighted to match the pileup distribution measured from the data. A change in the

total number of pileup events, within the errors, can alter efficiencies and thus $A \cdot \epsilon_{MC}$. The systematic uncertainty on $A \cdot \epsilon_{MC}$ due to modeling of the pileup interactions is estimated by varying the total inelastic cross section within its uncertainties.

6.4.5 PDF Uncertainties

The uncertainties on Parton Distribution Functions can alter the acceptance in simulation, especially for very forward, low x, Zγ events where the PDFs are not well determined. To estimate the systematic effect on $A \cdot \epsilon_{MC}$, LHAPDF [68] was used to generate per-event weights using variations along the 21 sets of eigenvectors of the CTEQ6L [69] PDF model. To assign an uncertainty due to variation of the PDF on the acceptance we use the 'modified tolerance method' [70] . In this method, asymmetric uncertainties $\Delta\sigma^+$ and $\Delta\sigma^-$ are defined as

$$\Delta\sigma^+ = \sqrt{\sum_{i=1}^{20}[max(\sigma_i^+ - \sigma_0, \sigma_i^- - \sigma_0, 0)]^2}$$

$$\Delta\sigma^- = \sqrt{\sum_{i=1}^{20}[max(\sigma_0 - \sigma_i^+, \sigma_0 - \sigma_i^-, 0)]^2}$$

These definitions give an estimate of the size of the largest positive and negative deviations of the cross section coming from varying the PDF eigenvectors. The larger of $\Delta\sigma^+$ or $\Delta\sigma^-$ is used to assign a symmetric systematic uncertainty on $A \cdot \epsilon_{MC}$ due to PDF variations.

6.4.6 Data/Monte Carlo Efficiency Scale Factors

The tag-and-probe efficiencies are subject to both statistical variation and variation arising from signal and background shape choices. Each of these variations can change the passing and failing signal and background yields, thus changing the measured

efficiency. Since in this analysis a per-event scale factor is used to correct the total $A \cdot \epsilon$ in MC, to reflect the efficiencies found in the data, the error on the ratio $\rho_{eff} = \epsilon_{\mathrm{Data}}/\epsilon_{\mathrm{MC}}$ is used to determine the systematic as it is exactly the error on a weight being applied to the MC. To calculate the systematic on $A \cdot \epsilon$ the central value of ρ_{eff} is varied up and down by one sigma and applied as a per-event weight. The maximal deviation in acceptance from the reweighing is taken as a systematic uncertainty.

6.4.7 Background Estimation

Template method

For the Zγ analysis the template method has three major systematic errors that must be taken into account. These errors fall into three categories, signal shape, background shape, and sampling bias and are detailed below:

1. Signal shape: As described in Sec. 6.2.1, the signal $\sigma_{i\eta i\eta}$ template in simulation needs to be corrected by 0.9×10^{-4} for barrel and 2.1×10^{-4} for endcap to match $\sigma_{i\eta i\eta}$ templates observed in data. We take this difference as a systematic uncertainty on signal template and re-calculate the background estimation to measure its effect on the final result.

2. Background shape: To obtain the background $\sigma_{i\eta i\eta}$ template we use photon-like jets selected by requiring a tracker 'anti-isolation' requirement. Using this template to infer the background from photon-like jets that pass the full photon isolation requirements can cause a bias if the $\sigma_{i\eta i\eta}$ template is correlated with tracker isolation. A contribution from genuine photons that pass the anti-isolation requirement can also cause a bias in estimation of the background. The size of these systematic effects are estimated in MC simulation where one can

distinguish genuine photons from jets. The resulting p_{T} dependent systematic uncertainties are given in Figure 6.11.

3. Sampling bias: Since smoothing is used to determine a continuous function that describes the $\sigma_{i\eta i\eta}$ distribution of the background, the effect of the statistical sampling of the background probability density function describing the true underlying shape must be understood. To study this, a bootstrapping technique exploiting MC simulation is used to generate a known true distribution of background from which we can throw toy template distributions. These toy distributions are then smoothed and used to fit the background fraction in data. The results of each toy template distribution fit is saved and the variance associated with the statistical fluctuation in the template is recorded and taken as a systematic error.

The results of applying the template method to the selected data and the corresponding systematics are shown in Figure 6.12 and Table 6.6, respectively. In each case the comparison of the template method yield with the raw predicted yield from MC is shown. Large disagreements at low photon E_{T} are expected between the data-driven estimation and the MC expectation. The MC is known to be wrong and underestimate the jet background to photons and the data-driven method has a clear advantage since it uses real photon-like jets from data. Therefore the background estimate from the data-driven method is known to be a more accurate calculation of the background yield.

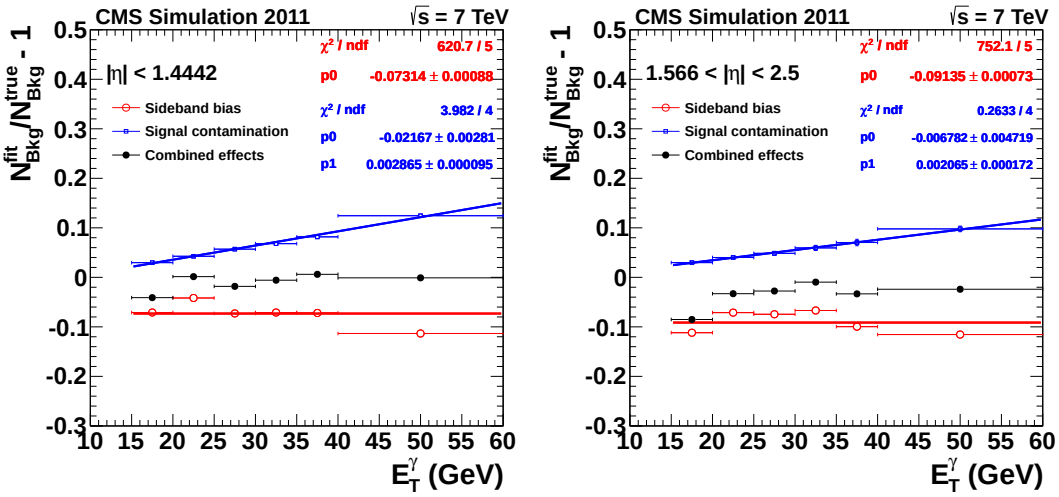

Figure 6.11: The uncertainty for 'sideband bias' and 'signal contamination' on the background template for barrel (left) and endcap (right). The change in the estimated number of background events due to 'anti-isolation' requirement (sideband bias) is given as a function of photon p_{T} as red circles, while the contamination from genuine photons are given as blue dots. The overall effect is given as black.

	$Z\gamma \to ee\gamma$		$Z\gamma \to \mu\mu\gamma$	
ECAL	Template	MC truth	Template	MC truth
Barrel	591.3 ± 24.5 (stat.) ± 26.3 (syst.)	466.0 ± 15.5	914.7 ± 63.2 (stat.) ± 110.2 (syst.)	383.8 ± 11.7
Endcap	314.7 ± 43.3 (stat.) ± 17.5 (syst.)	219.9 ± 10.6	489.6 ± 43.9 (stat.) ± 37.3 (syst.)	195.3 ± 8.5
Total	905.9 ± 49.8 (stat.) ± 31.5 (syst.)	686.0 ± 18.8	1404.3 ± 77.0 (stat.) ± 116.4 (syst.)	579.1 ± 14.4

Table 6.6: Z/γ^*+jets background estimation for the template method compared to MC truth(Z+jets only) using full 2011 dataset. The uncertainty for the data-driven method is statistical and systematic, while the MC truth uncertainty is statistical only.

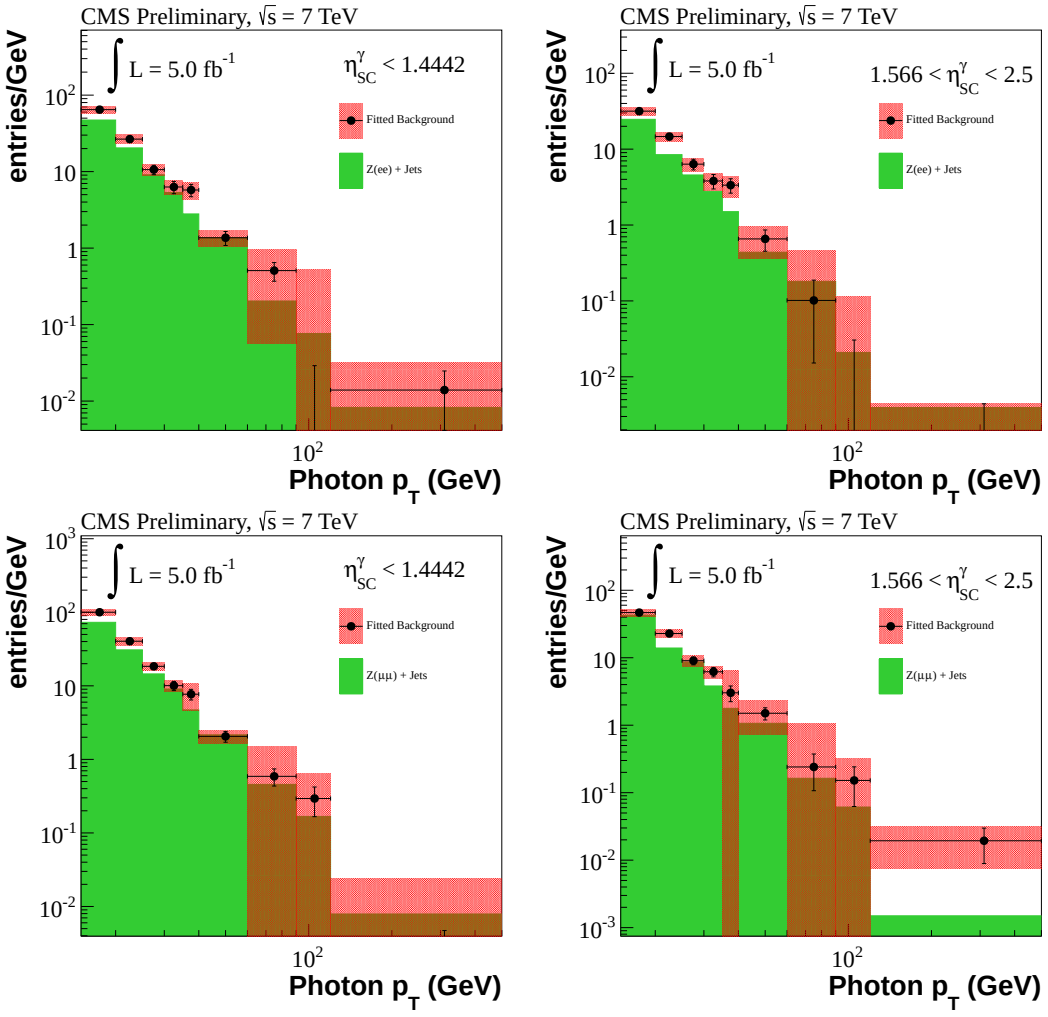

Figure 6.12: The results of applying the template method to the $\sigma_{i\eta i\eta}$ distributions in the observed data for the electron (top) and muon (bottom) channels in the EB (left) and EE (right). The black error bar is the statistical error and the hashed region represents additional systematic error. The significantly higher data-derived fake rate is expected.

		$ee\gamma$	$\mu\mu\gamma$
Source	Systematic uncertainty	Effect on N_{sig}	
Electron and photon energy scale	ele: 0.5%; pho: 1% (EB) 3% (EE)	3.0 %	n/a
Photon energy scale	1% (EB) 3% (EE)	n/a	4.19%
Muon p_T scale	0.2%	n/a	0.60%
Total uncertainty on N_{sig}		3.0 %	4.23%
Source	Systematic uncertainty	Effect on $\mathcal{F} = A \cdot \epsilon_{MC}$	
Electron and photon energy resolution	1% (EB), 3% (EE)	0.2 %	n/a
Photon energy resolution	1% (EB), 3% (EE)	n/a	0.06%
Muon p_T resolution	0.6%	n/a	0.08%
Pileup	Vary estimated PU using 68.3 ± 3.4 mb	0.6 %	0.44%
PDF	CTEQ6L reweighting	1.1%	1.10%
Signal Modeling		0.6 %	1.10%
Total uncertainty on $\mathcal{F} = A \cdot \epsilon_{MC}$		1.4 %	1.22%
Source	Systematic uncertainty	Effect on ρ_{eff}	
Electron reconstruction	0.4%	0.8 %	n/a
Electron trigger	0.1%	0.1 %	n/a
Electron ID and isolation	2.5%	5.0 %	n/a
Muon trigger	1.5%	n/a	1.0 %
Muon reconstruction	0.9%	n/a	1.0 %
Muon ID and isolation	0.9%	n/a	2.30%
Photon ID and isolation	0.5% (EB), 1.0% (EE)	0.5 %	1.00%
Total uncertainty on ρ_{eff}		5.1 %	2.51%
Source	Systematic uncertainty	Effect on background yield	
Template method	4.4% (EB), 5.6% (EE)	5.1 %	n/a
	4.9% (EB), 5.8% (EE)	n/a	5.5%
Total uncertainty on background		5.1 %	5.5%
Source	Systematic uncertainty	Effect on luminosity	
Luminosity	2.2%	2.2%	2.2%

Table 6.7: A summary of all systematic uncertainties on $A{\cdot}\varepsilon$, ρ_{eff}, N_{sig} and Luminosity.

Chapter 7

The Measurement of the Zγ Cross Section

The cross section of a given process is measured using the following formula:

$$\sigma = \frac{N_{\text{sig}}}{A_{\ell\ell\gamma} \cdot \epsilon \cdot \mathcal{L}} \tag{7.1}$$

where N_{sig} is the number of observed signal events, A is the fiducial and kinematic acceptance, ϵ is the selection efficiency for events in the acceptance, and $\mathcal{L}$ is the integrated luminosity. The value of A is affected by the PDF and other theoretical uncertainties, while the value of ϵ is susceptible to uncertainties from triggering and reconstruction. In order to control the efficiency uncertainties, corrections to the efficiencies in simulation are obtained from data. These correction factors come from efficiency ratios $\rho_{eff} = \epsilon/\epsilon_{\text{MC}}$ derived by measuring ϵ and ϵ_{MC} in the same way on data and simulation, respectively. The product $A_{\ell\ell\gamma} \times \epsilon$ is then replaced by $\mathcal{F}_{\ell\ell\gamma} \times \rho_{eff}$, where $\mathcal{F}_{\ell\ell\gamma} \equiv A_{\ell\ell\gamma} \times \epsilon_{\text{sim}}$ is the fraction of generated events selected in the simulation. The number of signal events N_{sig} is obtained by subtracting the estimated number of background events N_{bkg} from the observed number of selected events N_{obs}.

Equation (7.1) can therefore be rewritten as

$$\sigma = \frac{N_{\text{obs}} - N_{\text{bkg}}}{\mathcal{F} \cdot \rho_{eff} \cdot \mathcal{L}}. \tag{7.2}$$

$\mathcal{F}_{\ell\ell\gamma}$ is calculated from MC, as $\mathcal{F}_{\ell\ell\gamma}$ is defined as $N_{accept}/N_{gen,\ kin}$, where N_{accept} is the number of events passing all selection cuts, and $N_{gen,\ kin}$ is the number of generated events with $E_T^{\gamma} > 15$, $\Delta R_{\ell,\gamma} > 0.7$.

7.1 Extraction of the Cross Section

This section describes the measurement of the production cross section for $Z\gamma \to \ell\ell\gamma$, where $\ell = e,\ \mu$. As the cross section diverges at LO for soft photons or collinear to charged lepton, the measurement is restricted to the following kinematic range:

- The transverse photon energy must be larger than 15 GeV.
- The lepton and the photon must be spatially separated by $\Delta R(\ell, \gamma) > 0.7$.

Parameters	$Z\gamma \to ee\gamma$	$Z\gamma \to \mu\mu\gamma$
$N_{observed}$	4108 ± 64.1 (stat.)	6463 ± 80.4 (stat.)
$N_{background}^{DataDriven}$	905.9 ± 49.8 (stat.) ± 31.5 (syst.)	1404.3 ± 56.4 (stat.) ± 77.0 (syst.)
$N_{background}^{other}$	21.2 ± 1.8 (stat.)	23.7 ± 2.2 (stat.)
N_{Sig}	3154.2 ± 81.0 (stat.)± 95.1 (syst.)	5034.9 ± 98.2 (stat.) ± 213.2 (syst.)
$A \cdot \epsilon_{MC}$	0.132 ± 0.0018 (syst.)	0.196 ± 0.001 (stat.)
ρ_{eff}	0.929 ± 0.0466 (syst.)	0.945 ± 0.016 (syst.)
$\int L\ dt$	4961.1 ± 109.1 (syst.)	4998.9 ± 110.0 (syst.)

Table 7.1: Summary of parameter values for the $Z\gamma$ cross section measurement for the full 2011 dataset.

For $Z\gamma \to ee\gamma$, ρ_{eff} in Equation 7.2 is calculated as a product of data/MC correction factors for electron and photon reconstrution and identification efficiencies, *i.e.*, $\rho^2_{\text{reco}} \cdot \rho^2_{WP85} \cdot \rho_{\gamma} \cdot \rho_{trigger}$. For electrons and photons in barrel and endcap, different correction factors are considered. Similar to the electron channel, ρ_{eff} in $Z\gamma \to \mu\mu\gamma$

is calculated as a product of data/MC correction factors for muon and photon reconstrution and identification efficiencies.

The numbers that are used to calculate the cross sections are summarized in Table 7.1. The measured cross sections are:

$$\sigma(pp \to Z\gamma \to ee\gamma) = 5.20 \pm 0.13 \text{ (stat.)} \pm 0.30 \text{ (syst.)} \pm 0.11 \text{ (lumi.) pb.}$$

$$\sigma(pp \to Z\gamma \to \mu\mu\gamma) = 5.43 \pm 0.10 \text{ (stat.)} \pm 0.29 \text{ (syst.)} \pm 0.12 \text{ (lumi.) pb.}$$

Since the cross sections are found to be consistent with each other within their errors, the electron and muon channels are combined using a best linear unbiased estimate (BLUE), effectively an error weighted average of the individual cross sections [71]. Applying this method improves the precision on the measurement since it reduces the uncertianty coming from uncorrelated systematics, in addition to the $1/\sqrt{2}$ gain in statistical accuracy. The cross section derived from the BLUE combination is:

$$\sigma(pp \to Z\gamma \to \ell\ell\gamma) = 5.33 \pm 0.08 \text{ (stat.)} \pm 0.25 \text{ (syst.)} \pm 0.12 \text{ (lumi.) pb.}$$

All three results are consistent with the theoretical NLO cross section prediction of 5.45 ± 0.27 pb. within errors.

Finally, we present a summary of the Zγ cross sections measured with different lower bounds on the photon p_{T}. The measured cross sections, predictions from the Monte Carlo generator MCFM, and their errors are summarized in Table 7.2 and shown in Figure 7.1.

Zγ		
	$ee\gamma$	$\mu\mu\gamma$
$E_{\mathrm{T}}^{\gamma} > 60$ GeV	$0.142 \pm 0.019(\mathrm{stat.}) \pm 0.019(\mathrm{syst.}) \pm 0.003(\mathrm{lumi.})$	$0.139 \pm 0.013(\mathrm{stat.}) \pm 0.015(\mathrm{syst.}) \pm 0.003(\mathrm{lumi.})$
Combination	$0.140 \pm 0.011(\mathrm{stat.}) \pm 0.013(\mathrm{syst.}) \pm 0.003(\mathrm{lumi.})$ pb	
NLO Prediction	0.124 ± 0.009 pb	
$E_{\mathrm{T}}^{\gamma} > 90$ GeV	$0.047 \pm 0.013(\mathrm{stat.}) \pm 0.010(\mathrm{syst.}) \pm 0.001(\mathrm{lumi.})$	$0.046 \pm 0.008(\mathrm{stat.}) \pm 0.010(\mathrm{syst.}) \pm 0.001(\mathrm{lumi.})$
Combination	$0.046 \pm 0.007(\mathrm{stat.}) \pm 0.009(\mathrm{syst.}) \pm 0.001(\mathrm{lumi.})$ pb	
NLO Prediction	0.040 ± 0.004 pb	

Table 7.2: The summary of the Zγcross section measurements and predictions for photon $p_{\mathrm{T}} > 60$ and 90 GeV.

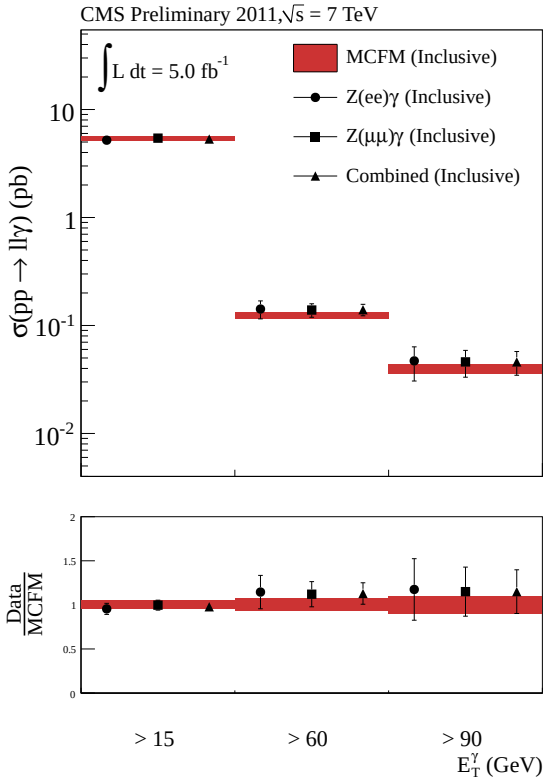

Figure 7.1: The summary of all cross section measurements for the Zγ channel.

Chapter 8

Anomalous Triple Gauge Coupling Limits

Triple gauge boson couplings (TGC) are a consequence of the non-Abelian nature of the SM electroweak sector $SU(2)_L \times U(1)_Y$ and are uniquely predicted as discussed in Section 1.3. The $ZZ\gamma$ and $Z\gamma\gamma$ vertices which vanish in the SM at tree level can be studied using $Z\gamma$ production. Experimental measurement of TGCs is an important test of the SM. Also, a number of extensions of the SM can manifest themselves in processes with multiple bosons in the final state. Thus, a measurement of TGCs can be sensitive to new phenomena at high energies that would require more energy or luminosity to be observed directly.

In this analysis the $ZZ\gamma$, and $Z\gamma\gamma$ couplings are measured without form-factor scaling, as this provides a result without any particular bias that can arise due to choice of the form-factor energy dependence, as discussed in Section 2.2.1.

8.1 $ZZ\gamma$ and $Z\gamma\gamma$ couplings

The most general vertex function [10] for $ZZ\gamma$ was discussed in Section 2.3 and as a reminder is repeated and revisited briefly.

$$\begin{aligned}\Gamma^{\alpha\beta\mu}_{\mathrm{Z}\gamma\mathrm{Z}}(q_1,q_2,P) &= \frac{P^2-q_1^2}{m_{\mathrm{Z}}^2}\Bigg[\; h_1^{\mathrm{Z}}(q_2^\mu g^{\alpha\beta}-q_2^\alpha g^{\mu\beta}) \\ &\quad + \frac{h_2^{\mathrm{Z}}}{m_{\mathrm{Z}}^2}P^\alpha\Big[(P\cdot q_2)g^{\mu\beta}-g_2^\mu P^\beta\Big] \\ &\quad + h_3^{\mathrm{Z}}\epsilon^{\mu\alpha\beta\rho}q_{2\rho} \\ &\quad + \frac{h_4^{\mathrm{Z}}}{m_{\mathrm{Z}}^2}P^\alpha\epsilon^{\mu\beta\rho\sigma}P_\rho q_{2\sigma}\Bigg]\end{aligned}$$

with $Z\gamma\gamma$ vertex obtained by the following replacements:

$$\frac{P^2-q_1^2}{m_Z^2}\to\frac{P^2}{m_Z^2}\;\; and\;\; h_i^Z\to h_i^\gamma,\; i=1,...,4. \tag{8.1}$$

The couplings h_i^V with $V=Z,\gamma$ and $i=1,2$ violate CP symmetry, while those with $i=3,4$ are CP-even. Although at tree level all these couplings in the SM are equal to zero, at one-loop level the CP-conserving couplings are $O(10^{-4})$. As the sensitivity to both CP-odd and CP-even couplings are about the same, we interpret the results in terms of h_i^V with $i=3,4$.

8.2 Likelihood Formalism

One effect of introducing anomalous coupling parameters in the SM Lagrangian is an enhancement of the diboson production cross section when $\hat{s}$ is large. This results in an excess of events with high momentum bosons. As the transverse energy of the photon is more sensitive to the effect of anomalous triple gauge couplings, aTGCs, than that of W or Z bosons, we use photon p_{T} as the observable to measure aTGCs.

We interpret the aTGC results by setting bounds on the ratio of the observed signal to that of the expected aTGC yield using the likelihood formalism described

below. The probability of observing $\mathbf{X}$ events with a specific value of p_T for a given expectation value d in data is given by the Poisson distribution:

$$p(\mathbf{X};d) = \frac{d^{\mathbf{X}}e^{-d}}{\mathbf{X}!} \quad , \quad d = \mu \cdot \mathbf{s}(\vec{\alpha},\vec{\theta_s}) + \mathbf{b}(\vec{\theta_b}), \tag{8.2}$$

where signal $\mathbf{s}(\vec{\alpha},\vec{\theta_s})$ and background $\mathbf{b}(\vec{\theta_b})$ expectations are described in terms of the TGC values $\vec{\alpha}$ and nuisance parameters $\vec{\theta_s}$ and $\vec{\theta_b}$. The parameter μ is the signal strength modifier. Here, d is comprised of both signal and background predictions that are modeled separately.

The nuisance parameters are resolved into three that represent the increase and decrease of expectation values given a fractional change in integrated luminosity f_L, signal, and background systematic uncertainties $f_{Sig.}^{Syst.}$ and $f_{Bkg.}^{Syst.}$, respectively:

$$\mathbf{s}(\vec{\alpha},\vec{\theta_s}) = f_{\mathcal{L}} \cdot f_{Sig.}^{\text{Syst.}} \cdot N^{\text{Sig.}}(\vec{\alpha}) \qquad \mathbf{b}(\vec{\theta_b}) = f_{bkg}^{\text{Syst.}} \cdot N^{\text{bkg}}. \tag{8.3}$$

Here, N_{sig} and N_{bkg} are the predicted signal and background event yields.

With this definition of d for each bin i of the photon p_T distribution with data event yield N_i, we construct a likelihood function:

$$L(\mu,\vec{\alpha},\vec{\theta}) = \prod_i Poisson(N_i, d_i(\mu,\vec{\alpha},\vec{\theta})) \quad , \text{ where } \quad \vec{\theta} = (\vec{\theta_s},\vec{\theta_b}) \tag{8.4}$$

with the Poisson function defined in Eq. 8.2. We assume that the errors on the quoted luminosity, signal selection, and background fraction are log-normally distributed and reflect this in the nuisance parameters by requiring log-normal constraints.

We determine the upper limits on TGCs by using the following test statistics:

$$t_{\mu,\vec{\alpha}} = -2\ln\lambda(\mu,\vec{\alpha}) \quad , \text{ where } \qquad \lambda(\mu,\vec{\alpha}) = \frac{L(\mu,\vec{\alpha},\hat{\hat{\vec{\theta}}})}{L(\hat{\mu},\vec{\alpha},\hat{\hat{\vec{\theta}}})} \tag{8.5}$$

with $\hat{\hat{\vec{\theta}}}$ being the conditional maximum-likelihood estimator of $\vec{\theta}$ and $\hat{\mu}$ and $\vec{\theta}$ being their maximum-likelihood estimators. We exclude the hypothesized values of TGCs

based on whether the ratio of p-values:

$$CL_s = \frac{p_{s+b}}{1 - p_b} \tag{8.6}$$

is less than a given threshold. More details can be found in [72]. This formalism is implemented using the RooStats package [73].

8.2.1 Tests of Two Limit Setting Techniques

The CLs criterion is not the only viable choice for setting limits on anomalous triple gauge couplings. Additionally, the CLs treatment does not transition in a reasonable way to allowed regions where the null hypothesis is excluded. Specifically, the property that the CLs confidence interval always covers the null hypothesis prevents this kind of behavior entirely. This property instead results in the behavior that the presense of a real anomalous triple gauge coupling is indicated merely by the observed limit wildly disagreeing with the expected limit in the case of no signal and no actual exclusion of the null hypothesis.

The profile likelihood treatment, similar to that used by CDF and D0, instead uses Wilks' theorem which holds that maximum likelihood estimates are distributed as a χ^2 distribution and hence their quantiles correspond to confidence intervals. To calculate the quantiles, the number of degrees of freedom is assigned to be the number of parameters of interest being varied at the time. In the case of aTGC limits, due to the degeneracies in shape between the different couplings, at most two couplings are varied at a time.

To verify these behaviors a case study was performed using pseudo-data taken from aTGC limits being set for Wγ, a corresponding charged triple gauge coupling analysis. Since this study was performed to understand the behavior of statistical techniques and was presented before results were made public, it is scaled to different

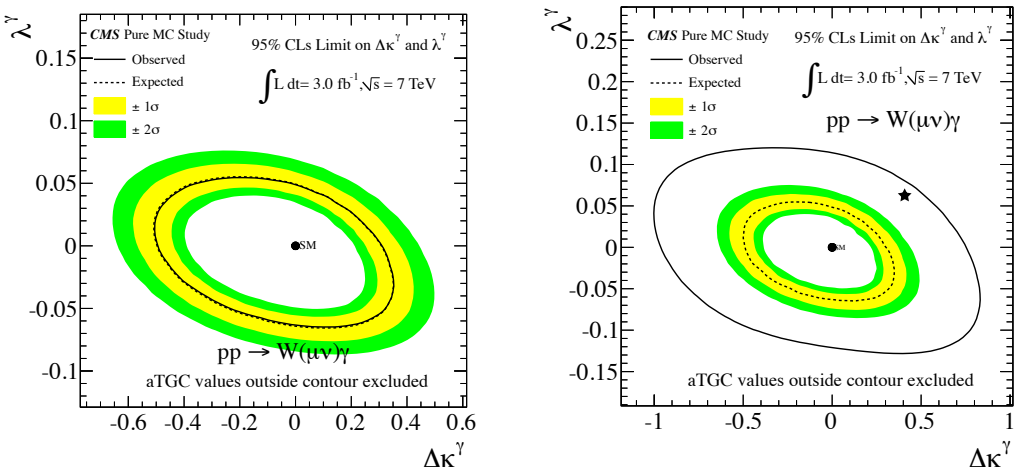

Figure 8.1: CLs limits in the scenario of anomalous triple gauge couplings for a toy MC study representing 3 fb^{-1}. The left plot demonstrates the response of the limits in the case of no aTGC. The right plot demonstrates the response with an aTGC signal represent, and the non-exclusion of the null hypothesis, the Standard Model.

integrated luminosity, 3 fb^{-1}, and has different systematics compared to the true analysis. The results of performing the CLs limit setting procedure with and without an anomalous triple gauge coupling signal is shown in Figure 8.1. The null-covering property of the CLs methodology is readily apparent. The exact same aTGC data, treated with using profile likelihood limits shows the formation of allows regions and rejection of the null hypothesis and is shown in Figure 8.2. However, there are some further problems in the use of profile likelihood limits. For instance, there is a degeneracy in the values of the parameters excluded since the deformations in the p_{T} distributions from aTGCs are insensitive to the sign of the anomalous coupling and the minimizers and contour finders [74] used to determine the limit will only find one of the allow regions. This results in an improper limit again since one of the degenerate values will be improperly excluded. Since either limit setting technique has a signature of the data not agreeing with the null hypothesis, both are equally applicable for setting limits and CLs limits are used in this thesis.

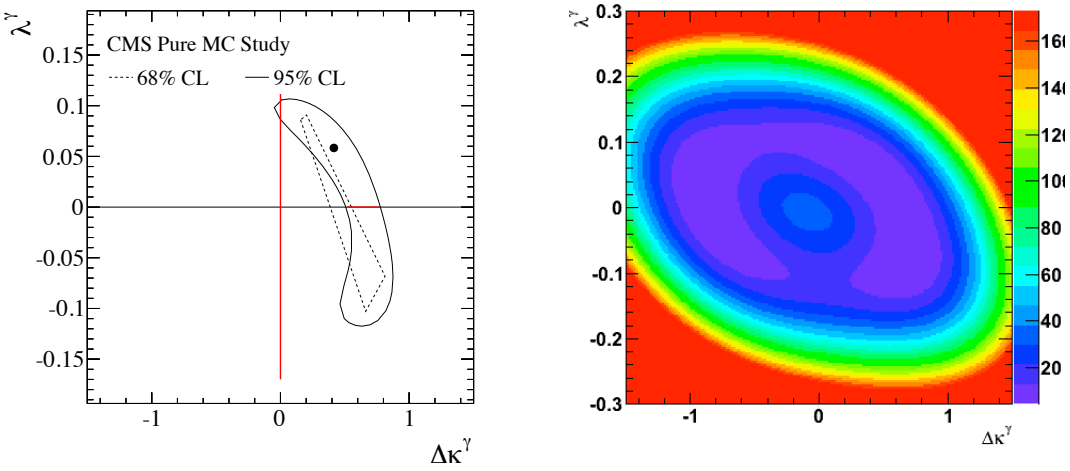

Figure 8.2: Profile likelihood limits on anomalous triply gauge couplings for the same toy MC study as Figure 8.1. Here the SM is excluded but only one of the degenerate allowed regions is found as shown in the likelihood scan in the right plot.

8.3 Limits on Zγ Anomalous Triple Gauge Couplings

The aTGC signal is generated using Sherpa [28] to simulate the $Z\gamma$+n jet (n $\leq$ 1) process. Two aTGC parameters, h_3^V and h_4^V with $V = Z,\ \gamma$ are freely varied. The generated data are normalized to the calculated NLO cross section from MCFM [19] including anomalous triple gauge couplings.

One and two dimensional limits are set in the h_3^V and h_4^V parameter space. For one dimensional limits when $V = Z$, we set all $Z\gamma\gamma$ couplings to their SM values, to zero, and for $V = \gamma$ we set all $ZZ\gamma$ couplings to zero.

The 95% C.L. two-dimensional contours are given in Fig. 8.3 for the scenario with no form-factor, and their corresponding one-dimensional limits in Table 8.1.

	h_3^γ	h_4^γ	h_3^Z	h_4^Z
$Z\gamma \to ee\gamma$	[-0.013, 0.013]	[-1.1e-4, 1.1e-4]	[-0.011, 0.011]	[-9.9e-5, 9.5e-5]
$Z\gamma \to \mu\mu\gamma$	[-0.013, 0.013]	[-1.1e-4, 1.2e-4]	[-0.011, 0.011]	[-1.0e-4, 1.1e-4]
$Z\gamma \to \ell\ell\gamma$	[-0.010, 0.010]	[-8.8e-5, 8.8e-5]	[-8.6e-3, 8.4e-3]	[-8.0e-5, 7.9e-5]

Table 8.1: One-dimensional limits on $Z\gamma$ anomalous trilinear gauge couplings.

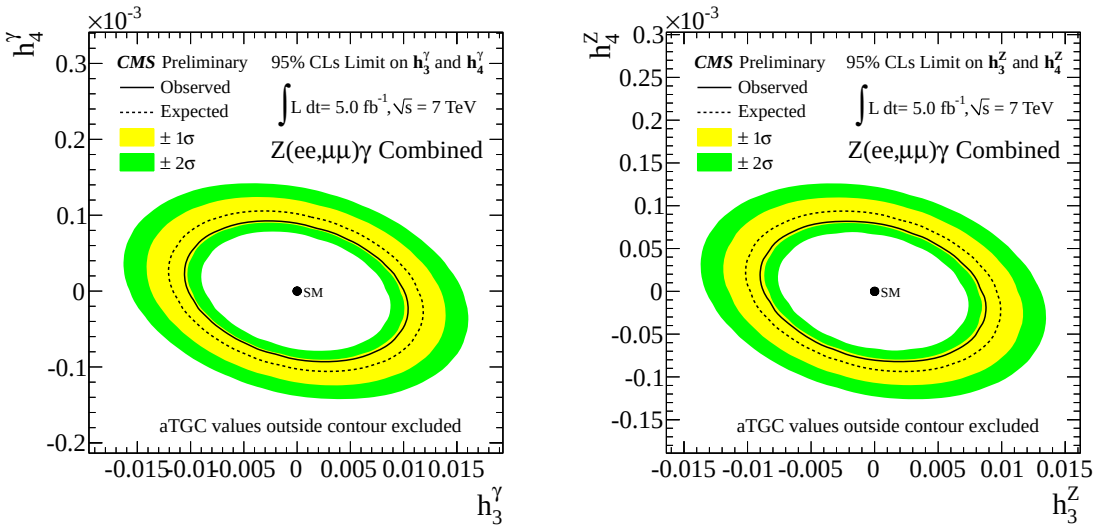

Figure 8.3: 95% confidence level contours for $Z\gamma\gamma$ (left) and $ZZ\gamma$ (right) couplings from the combined information of the electron and muon channels. The observed limits are within one standard deviation of the expected sensitivity.

8.4 Previous Results

Both the Tevatron [75] and LEP [76] colliders have produced results on anomalous triple gauge couplings. Different choices of limit setting technique and kinematic variables were used in each analysis due to the different kinematic properties of each collider in addition to the nature of the colliding particles. The LEP experiments set limits using angular correlations in addition to photon p_T shape since the direction and charges of the incoming leptons were known, making the LEP experiments sensitive to effects dependent on angular correlation and thus on CP.

The Tevatron experiments used photon p_T based analyses to extract limits on anomalous triple gauge couplings and are therefore insensitive to the difference between the CP even and CP odd neutral aTGCs. The Tevatron experiments chose to analyze the p_{T} distribution since this analysis variant is very robust and sensitive to the magnitude of the anomalous couplings and when measuring a difference from zero the magnitude is the quantity of primary importance. There is difficulty in adding meaningful angular variables, since it requires detailed knowledge of the detector efficiencies as well as accurate and precise simulation of the detector and physics involved, as to not create fake physical signals from detector mismodelings or inefficiencies [16, 17]. Furthermore, the angular effects of aTGCs would show up at only at high photon pT, being washed out by Standard Model production elsewhere.

8.4.1 The LEP Experiments

The LEP accelerator was an electron-positron collider at CERN located in the same tunnel as the LHC is presently. On the LEP ring there were four experiments, DELPHI, L3, ALEPH and OPAL [77–80]. Each of the experiments was a general purpose particle physics detector aiming to thoroughly study the newly discovered W and Z bosons. Along with measuring the properties of the W and Z bosons [81], the gauge boson couplings to each other were measured by each experiment, including results on Zγ aTGC limits. Due to the 'clean'[1] nature of events at LEP, the Zγ final states with the largest branching fractions were studied first, since there was effectively no background. This is in contrast with the Tevatron and LHC, where the $q\bar{q}\gamma$ and $\nu\bar{\nu}\gamma$ final states of the Z are difficult to detect due to the large backgrounds from QCD

[1]There is practically no QCD background in electron-positron collisions, except from ISR photons that decay into quark pairs.

processes[2].

The DELPHI collaboration set limits on anomalous triple gauge couplings by measuring the total cross section of the process $e^+e^- \to \nu\bar{\nu}\gamma$, with the requirement that the energy of the photon be greater than 25 GeV and the polar angle be $25° < \theta_\gamma < 135°$ [82]. Here, the polar angle is measured as the angle of the photon with respect to the LEP electron direction in the lab frame. The associated measured cross section by the DELPHI collaboration was:

$$\sigma(e^+e^- \to \gamma + \text{invisible particles}) = 1.47 \pm 0.38(\text{stat.}) \pm 0.30(\text{syst.})\text{pb},$$

limits on aTGC were set using a form factor cutoff scale of 1 TeV and are shown in Figure 8.4.

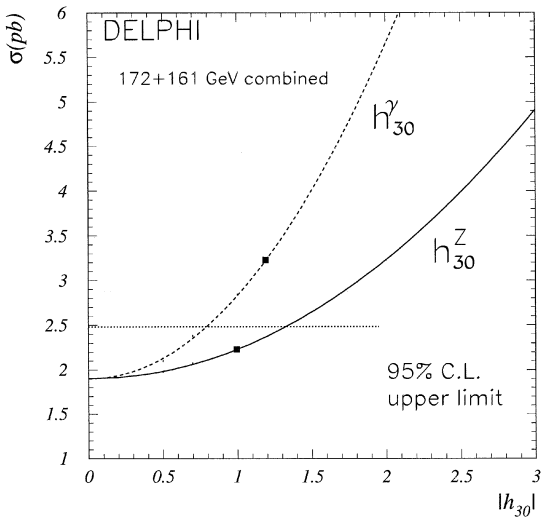

Figure 8.4: Limits on anomalous triple gauge couplings from the DELPHI collaboration using the $e^+e^- \to \nu\bar{\nu}\gamma$ final state. Limits are set on $h_3^{Z,\gamma}$ with a cutoff scale $\Lambda =$ 1 TeV and n = 3. The square points correspond to the unitarity bounds of for this cutoff scale. [82]

The L3 collaboration performed a similar analysis. Here, the final state photon was required to have energy greater than 15 GeV and to be consistent with a photon

[2]At the Tevatron and LHC the high-purity charged lepton final states of the Z are used to eliminate background.

that originated from the interaction region[3]. The polar angle of the photon was required to be within the range $20° < \theta_\gamma < 160°$ [83]. The aTGC limits were set using form factors with cutoff scales of 0.5 and 1 TeV and were compared to the available limits established by CDF at the Tevatron [84], adopting the same form factors for direct comparison. These limits are shown in Figure 8.5.

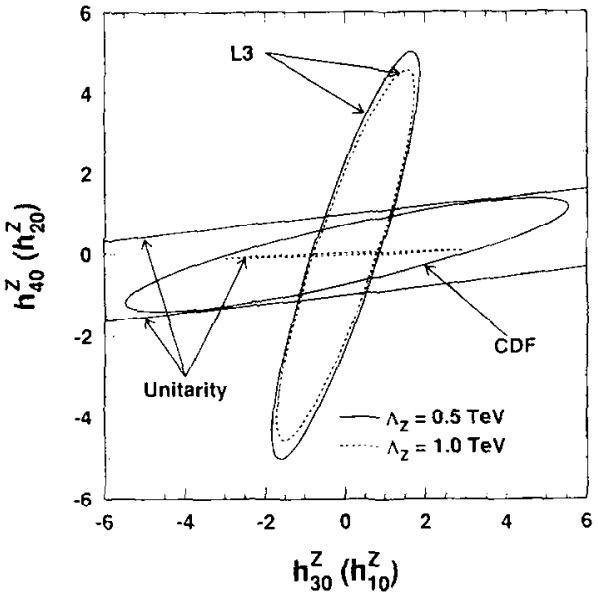

Figure 8.5: Limits on anomalous triple gauge couplings from the L3 collaboration using the $e^+e^- \to \nu\bar{\nu}\gamma$ final state. Limits are set on $h^Z_{3,4}$ with cutoff scales $\Lambda = 0.5$ & 1 TeV and n = 3. A comparison to the CDF collaboration's results is displayed as well. [83]

Due to improvements of the theoretical description and better understanding of the detector performance, the ALEPH collaboration was able to set limits on neutral anomalous triple gauge couplings using both the p_T shape and angular distributions of the Zγ final state. The ALEPH collaboration investigated the $q\bar{q}\gamma$ final state to probe the anomalous couplings using a kinematic dependent photon energy cut of $E_\gamma > E_{peak} - 15GeV$, $|\cos\theta_\gamma| < 0.95$ and more performant jet-finding algorithms [85]. This

[3]L3 had a layered calorimeter capable, to some extent, of pointing.

analysis demonstrates the ability of angular correlations to provide a determination of the sign of the anomalous triple gauge coupling parameters and the limits set can be seen in Figure 8.6.

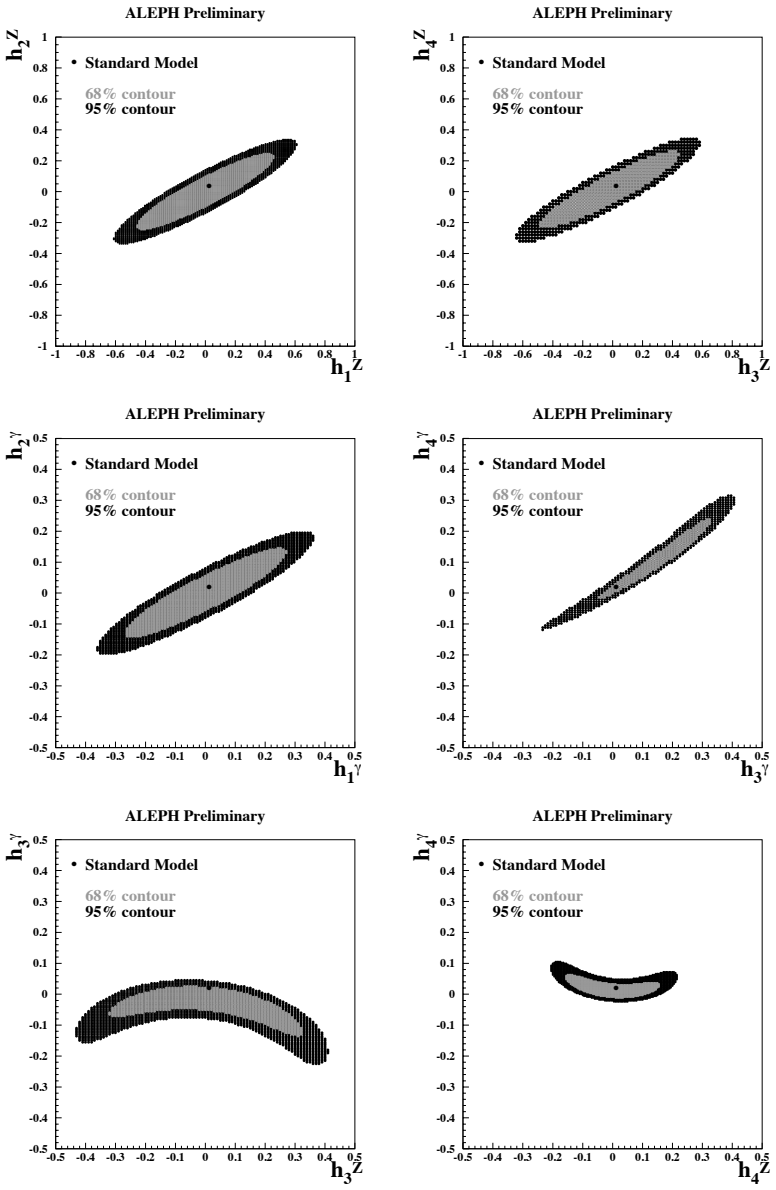

Figure 8.6: Limits on anomalous triple gauge couplings from the ALEPH collaboration using the $e^+e^- \to q\bar{q}\gamma$ final state. Limits are set on all eight anomalous couplings using a reweighing technique. Both p_T and angular information are input to the fit. No form factor is used. [85]

The OPAL collaboration also used a p_T and angular based analysis of the $\nu\bar{\nu}\gamma$ and $q\bar{q}\gamma$ final states to probe for anomalous couplings [29]. This analysis represents the most advanced and precise of all the LEP analyses summarized here. In the OPAL analysis, the selection of the photon is common between the hadronic and leptonic channels, requiring: $50\ GeV < E_\gamma < 90\ GeV$ and $15^\circ < \theta_\gamma < 165^\circ$. The resulting aTGC limits are presented in Figure 8.7.

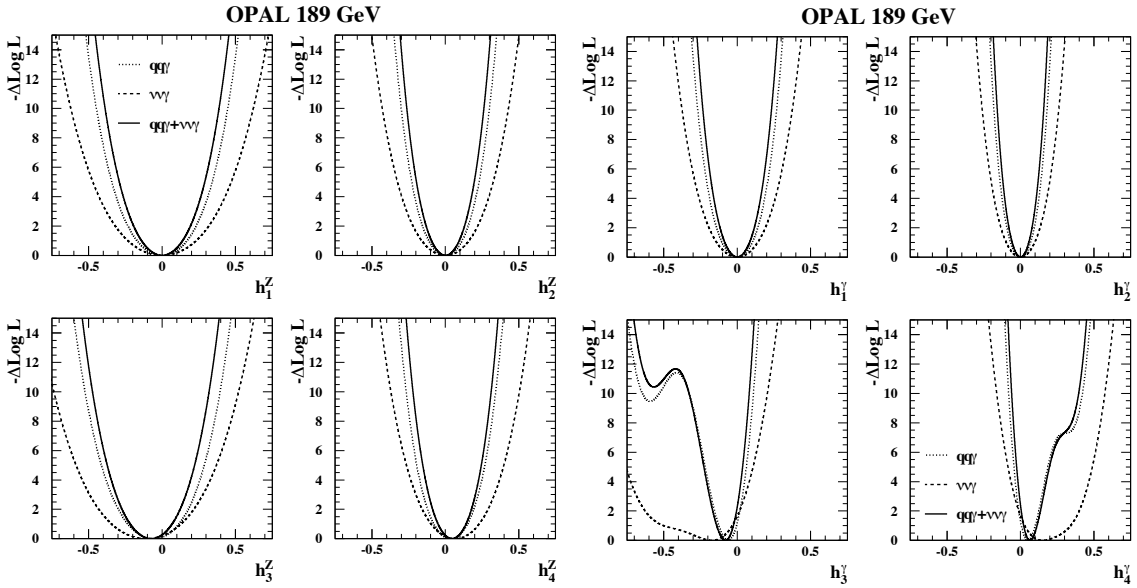

Figure 8.7: Limits on anomalous triple gauge couplings from the OPAL collaboration using the $e^+e^- \to q\bar{q}\gamma$ and $e^+e^- \to \nu\bar{\nu}\gamma$ final states. Limits are set on all eight anomalous couplings using a multidimensional fit based on MC yields. Both p_T and angular information are input to the fit. No form factor is used. [29]

Throughout all the studies performed and limits set by the four LEP collaborations there were no statistically significant deviations of the measured neutral aTGCs from their predicted standard model values. However, it is of note that the sensitivity of the experiments was intrinsically kinematically limited by the LEP center of mass energy of 208 GeV, and the effect of the aTGCs depends critically on the available energy in the initial state. Nevertheless, these measurements played a crucial role in improving the analysis techniques, both theoretically and in terms of statistical

methods, and represented a fundamental milestone for further measurements with higher kinematic reach typical of experiments at the Tevatron and LHC.

8.4.2 Experiments at the Tevatron

The CDF [86] and DØ [87] detectors operated from 1983 until 2011 at the proton-antiproton Tevatron collider, which operated at 1.0, 1.6, 1.8, and 1.96 TeV center of mass energies. While the two detectors' main contribution to particle physics was the discovery of the top quark [88,89], each also made significant contributions in setting limits on neutral aTGCs. The significantly higher center of mass energy available at the Tevatron coupled with larger luminosity improved the limits by nearly an order of magnitude compared to the even the most recent LEP results. Since the Tevatron is a hadron collider, there is a significant rate of jets being identified as photons. This causes idenfication of hadronic Z decays to be prone to large fake rates due to the large cross section of $pp \to 3 \text{ jets} + X$ at hadron colliders. In light of this, the aTGC analyses performed at the Tevatron use only the electron, muon and neutrino decays of the Z boson to tag candidate events[4]. The hadronic jet background is estimated by analyzing the differences in the shape of the energy deposit left by 'fake' photons as compared to true electrons or photons.

Both aTGC analyses performed by CDF [90] and DØ [91] set limits on the CP-conserving neutral aTGCs parameters, $h_3^{Z,\gamma}$ and $h_4^{Z,\gamma}$, using the p_T distribution of photons identified in association with a Z boson decaying leptonically. The resulting limits from the DØ analysis are found in Figure 8.8. The corresponding limits from the CDF collaboration, set using more data and the same final states, are shown in Figure 8.9. The DØ experiment was the first to exploit the $\nu\bar{\nu}\gamma$ final state, due to

[4]Limits obtained from tau decays of the Z in the search for Zγ have not yet been considered at the Tevatron.

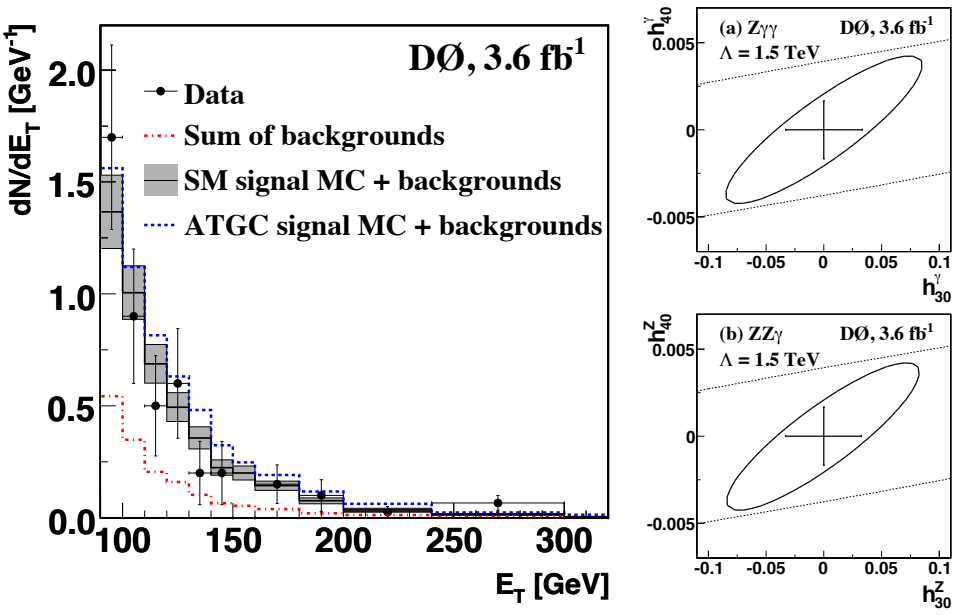

Figure 8.8: Limits from D0 on anomalous triple gauge couplings using all leptonic decay modes of the Z except that to taus. The spectrum shown to the left is for the $\nu\bar{\nu}\gamma$ final state only. [91]

the much larger branching ratio of the Z to the three neutrinos.

Parameter	(Λ = 1.2 TeV)	(Λ = 1.5 TeV)
h_3^Z	[-0.024,0.027]	[-0.020,0.021]
h_4^Z	[-0.0013,0.0013]	[-0.0009,0.0009]
h_3^γ	[-0.026,0.026]	[-0.022,0.020]
h_4^γ	[-0.0012,0.0013]	[-0.0008,0.0008]

Figure 8.9: Current limits from CDF on anomalous triple gauge couplings including all leptonic decays of the Z aside from taus. [90]

8.4.3 aTGC Limits from ATLAS with 1 fb^{-1}

The ATLAS experiment at the LHC has recently produced limits on Zγ anomalous triple gauge couplings [92]. The methodology used was a reweighing technique where a fully reconstructed sample with an anomalous triple gauge coupling was produced and then subsequently re-weighed using a quadratic function determined from generator

level information to represent effect of different anomalous triple gauge couplings. The limits are set using the profile likelihood methodology. Unlike the CMS analysis presented here, a jet veto is applied to remove the effects of higher order corrections to the Zγ cross section. Like the CMS, CDF, and D0 analyses the ATLAS aTGC limits are extracted using the photon p_{T} distribution only and use only one bin in photon p_{T} to measure the deviation in the cross section. The results of this analysis are shown in Figure 8.10.

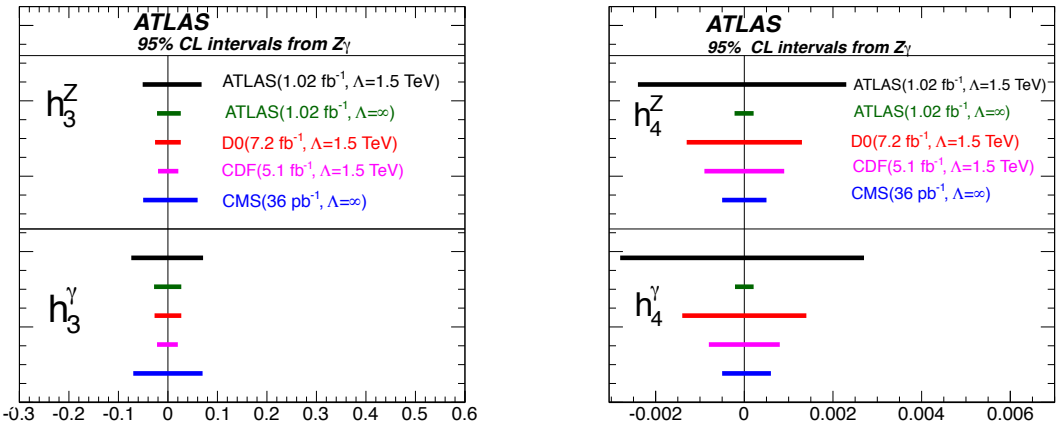

Figure 8.10: Current one dimensional limits from ATLAS using 1 fb^{-1} of integrated luminosity collected in 2011. A comparison to CDF, D0 and CMS 36 pb^{-1} results is shown. [92]

8.4.4 Comparison To Presented Results

The results presented in this thesis represent a significant increase in statistical power over the results from LEP, The Tevatron, and ATLAS at the LHC. The LEP results, while they do make use of angular variables and decays of the Z with higher branching fraction, are limited both in statistics and energy reach. The presented limits are more stringent than the LEP results by at least two orders of magnitude in all cases.

The Tevatron results all use a form factor of 1.2-2 TeV, arbitrarily limiting their

sensitivity to couplings since form factors suppress the aTGC enhancements to the cross section. This also makes the limits difficult to compare between CMS and the Tevatron, though some guess can be made from the ATLAS results in Figure 8.10. Still, the higher energy reach available at the LHC allows better probing of aTGCs as their effects in the case of $Z\gamma$ scale linearly or better with the average $\hat{s}$ available in collisions.

The LHC results from ATLAS use only 1 fb^{-1} of data and do not analyze the shape of the photon p_{T} distribution that they are using to set limits, though the detriment of this is reduced as the photon p_{T} cut in the aTGC analysis is 60 GeV. Since aTGCs are an effect that manifests at high photon p_{T}, the shape is an important factor and this is included in the CMS analysis since it is performed differentially in photon p_{T} starting from 40 GeV. The CMS expected limits on, *i.e.* sensitivity to, the anomalous triple gauge couplings using the full 5.0 fb^{-1} is an expected factor of $1/\sqrt{5}$ better than those of ATLAS. This indicates the the primary reason for the improvement is the larger statistical sample. Correspondingly, the observed limits, given in Table 8.1, on the couplings are a factor of 2.8 better than those of ATLAS, slightly better than statistics but likely driven by the underflucuation seen compared to the expected limits. This represents a significant improvement in limits on anomalous triple gauge couplings and a powerful verification of the Standard Model.

Chapter 9

Conclusions

9.1 Summary

The complete methodology for performing the analysis on the Zγ final state at CMS to calculate its production cross section and set limits on anomalous triple gauge couplings has been presented. The analysis depends critically on three reconstruction algorithms to accurately and efficiently identify muons, electrons and photons. The identification of muons, electrons, and photons is achieved through the use of stringent isolation criteria, accurate modeling of shower shape profiles, and performing track fit algorithms.

Since there is still a significant irreducible background from fake photons due to jets that hadronize into π^0s, a data-driven background estimation technique was implemented based on shower shapes since the MC does not accurately predict the fake photon yield. The results of the data-driven background estimations, in addition to percent-level corrections from MC based background estimates, were used to extract the number of signal events in the electron and muon decay channels of the Z in the Zγ diboson system.

Using these techniques, the Zγ cross section was extracted in the electron and muon channels using the entire statistics of the 2011 CMS dataset. The measured cross sections and their combination are found in agreement with NLO standard model predictions within errors. Additionally, limits on the neutral ZγZ and Z$\gamma\gamma$ anomalous triple gauge couplings were set using the CLs methodology with allowed regions: $-0.010 < h_3^\gamma < 0.010$, $-8.8 \cdot 10^{-5} < h_4^\gamma < 8.8 \cdot 10^{-5}$, $-8.6 \cdot 10^{-3} < h_3^Z < 8.3 \cdot 10^{-3}$, and $-8.0 \cdot 10^{-5} < h_4^Z < 7.9 \cdot 10^{-5}$ at 95% confidence level. No form factor was used in limit setting and the statistical senstivity of the measurement improved by a factor of $1/\sqrt{5}$ upon the most recent limits published by the ATLAS collaboration.

9.2 Outlook

The 2012 dataset being collected presently represents rich opportunities for further studies of the Zγ final state since it should provide more than 20 fb^{-1} of data. The study of the recently discovered boson at 125 GeV [93,94] is of enormous interest since, as it decays to $\gamma\gamma$, it is likely to decay to Zγ as well and, according to standard model expectations, should become accessible with the full 2012 dataset. Furthermore, the study of anomalous triple gauge couplings will remain relevant since the statistical power of the dataset will allow even more stringent limits to be set. Recent advents in theoretical treatment of anomalous triple gauge couplings in the context of effective field theory [95] will provide a modern and more theoretically consistent framework for simulating and describing aTGCs.

An aspect of anomalous triple gauge couplings which has been so far out of reach at hadron colliders is the study of the angular correlations and spin alignment of the Zγ final state. A method for extracting this information using a data-driven technique to estimate the phase space is discussed in Appendix C. Moreover, the analysis

program used for extracting the anomalous triple gauge couplings was developed in a generalized way such that any relevant physical observable can be used to test for aTGCs. The general nature of the program has allowed it to be used to extract anomalous couplings in several diboson final states at CMS. Since most of these diboson final states have low cross sections, the results obtained using the 2011 dataset should be significantly improved in 2012. These additional final states and their corresponding aTGC limits are discussed in Appendix B.

Bibliography

[1] B. Pontecorvo. Neutrino Experiments and the Problem of Conservation of Leptonic Charge. *Soviet Journal of Experimental and Theoretical Physics*, 26:984, May 1968.

[2] The SNO Collaboration. Direct evidence for neutrino flavor transformation from neutral-current interactions in the sudbury neutrino observatory. *Phys. Rev. Lett.*, 89:011301, Jun 2002.

[3] The Super-Kamiokande Collaboration. Measurements of the Solar Neutrino Flux from Super-Kamiokande's First 300 Days. *Physical Review Letters*, 81:1158–1162, August 1998.

[4] The Daya Bay Collaboration. Observation of electron-antineutrino disappearance at Daya Bay. *Phys.Rev.Lett.*, 108:171803, 2012.

[5] Vernon D. Barger. COLLIDER PHYSICS PHENOMENOLOGY. 1985.

[6] Emmy Noether. Invariant Variation Problems. *Gott.Nachr.*, 1918:235–257, 1918.

[7] Peter W. Higgs. Spontaneous Symmetry Breakdown without Massless Bosons. *Phys.Rev.*, 145:1156–1163, 1966.

[8] G. Antchev, P. Aspell, I. Atanassov, V. Avati, J. Baechler, et al. First measurement of the total proton-proton cross section at the LHC energy of $\sqrt{s} = 7TeV. Europhys. Lett., 96 : 21002, 2011.$

[9] G. Arnison and others (The UA1 Collaboration). Experimental observation of lepton pairs of invariant mass around 95 gev/c2 at the cern sps collider. *Physics Letters B*, 126(5):398 – 410, 1983.

[10] U. Baur and E. L. Berger. Probing the weak-boson sector in zγ production at hadron colliders. *Phys. Rev. D*, 47:4889–4904, Jun 1993.

[11] U. Baur, T. Han, and J. Ohnemus. Qcd corrections and anomalous couplings in zγ production at hadron colliders. *Phys. Rev. D*, 57:2823–2836, Mar 1998.

[12] A.D. Martin, W.J. Stirling, R.S. Thorne, and G. Watt. Parton distributions for the LHC. *Eur.Phys.J.*, C63:189–285, 2009.

[13] Diogo Boito, Oscar Cata, Maarten Golterman, Matthias Jamin, Kim Maltman, et al. A new determination of $\alpha_s from hadronic \tau$ *decays*. *Phys.Rev.*, $D84$: 113006, 2011.

[14] Kuang-Ta Chao, Han-Wen Huang, and Yu-Quan Liu. Gluonic and leptonic decays of heavy quarkonia and the determination of alpha-s (m(c)) and alpha-s (m(b)). *Phys.Rev.*, D53:221–230, 1996.

[15] Michael E. Peskin and Daniel V. Schroeder. An Introduction to quantum field theory. 1995.

[16] K. O. Mikaelian, M. A. Samuel, and D. Sahdev. Magnetic moment of weak bosons produced in pp and $p\overline{p}$ collisions. *Phys. Rev. Lett.*, 43:746–749, Sep 1979.

[17] C. J. Goebel, F. Halzen, and J. P. Leveille. Angular zeros of brown, mikaelian, sahdev, and samuel and the factorization of tree amplitudes in gauge theories. *Phys. Rev. D*, 23:2682–2685, Jun 1981.

[18] Stefano Frixione, Paolo Nason, and Carlo Oleari. Matching NLO QCD computations with Parton Shower simulations: the POWHEG method. *JHEP*, 0711:070, 2007.

[19] John M. Campbell, R. Keith Ellis, and Ciaran Williams. Vector boson pair production at the LHC. *JHEP*, 1107:018, 2011.

[20] Tom Melia, Paolo Nason, Raoul Rontsch, and Giulia Zanderighi. W+W-, WZ and ZZ production in the POWHEG BOX. *JHEP*, 1111:078, 2011.

[21] Simone Alioli, Paolo Nason, Carlo Oleari, and Emanuele Re. NLO vector-boson production matched with shower in POWHEG. *JHEP*, 0807:060, 2008.

[22] Ryan Gavin, Ye Li, Frank Petriello, and Seth Quackenbush. FEWZ 2.0: A code for hadronic Z production at next-to-next-to-leading order. *Comput.Phys.Commun.*, 182:2388–2403, 2011.

[23] Kaoru Hagiwara, R.D. Peccei, D. Zeppenfeld, and K. Hikasa. Probing the Weak Boson Sector in e+ e- → W+ W-. *Nucl.Phys.*, B282:253, 1987.

[24] C. N. Yang. Selection rules for the dematerialization of a particle into two photons. *Phys. Rev.*, 77:242–245, Jan 1950.

[25] K. Arnold, J. Bellm, G. Bozzi, F. Campanario, C. Englert, et al. Release Note – Vbfnlo-2.6.0. 2012.

[26] K. Arnold, J. Bellm, G. Bozzi, M. Brieg, F. Campanario, et al. VBFNLO: A Parton Level Monte Carlo for Processes with Electroweak Bosons – Manual for Version 2.5.0. 2011.

[27] K. Arnold, M. Bahr, Giuseppe Bozzi, F. Campanario, C. Englert, et al. VBFNLO: A Parton level Monte Carlo for processes with electroweak bosons. *Comput.Phys.Commun.*, 180:1661–1670, 2009.

[28] T. Gleisberg, Stefan. Hoeche, F. Krauss, M. Schonherr, S. Schumann, et al. Event generation with SHERPA 1.1. *JHEP*, 0902:007, 2009.

[29] G. Abbiendi et al. Search for trilinear neutral gauge boson couplings in $Z\gamma$ production at $S^{(1/2)} = 189$-GeV at LEP. *Eur.Phys.J.*, C17:553–566, 2000.

[30] O. Bruning, H. Burkhardt, and S. Myers. The large hadron collider. *Prog.Part.Nucl.Phys.*, 67:705–734, 2012.

[31] CMS Collaboration. Cms luminosity - public results. `https://twiki.cern.ch/twiki/bin/view/CMSPublic/LumiPublicResults`, July.

[32] S. Chatrchyan et al. The CMS experiment at the CERN LHC. *JINST*, 3:S08004, 2008.

[33] G. Aad et al. The ATLAS Experiment at the CERN Large Hadron Collider. *JINST*, 3:S08003, 2008.

[34] Jr. Alves, A. Augusto et al. The LHCb Detector at the LHC. *JINST*, 3:S08005, 2008.

[35] K. Aamodt et al. The ALICE experiment at the CERN LHC. *JINST*, 3:S08002, 2008.

[36] Christiane Lefvre. The cern accelerator complex. complexe des acclrateurs du cern. `https://cdsweb.cern.ch/record/1260465?ln=en`, Dec 2008.

[37] Mike Syphers. Overview of lhc accelerator. `http://atlas.physics.arizona.edu/~johns/downloads/linac/UTclass2lhc.pdf`.

[38] Lenny Rivkin. Synchrotron radiation. `http://cas.web.cern.ch/cas/Bulgaria-2010/Talks-web/Rivkin-1-web.pdf`.

[39] A.L. Macpherson. Lhc availability and performance in 2011. `http://indico.cern.ch/getFile.py/access?contribId=2&sessionId=0&resId=2&materialId=paper&confId=164089`, Feb 2012.

[40] Fermilab Accelerator Division. Accelerator division world records. `http://tomato.fnal.gov/ops/records.php`, August.

[41] Stephen P. Martin. A Supersymmetry primer. 1997.

[42] CMS, tracker technical design report. 1998.

[43] CMS: The electromagnetic calorimeter. Technical design report. 1997.

[44] CMS: The hadron calorimeter technical design report. 1997.

[45] CMS, the Compact Muon Solenoid. Muon technical design report. 1997.

[46] Serguei Chatrchyan et al. Performance of CMS muon reconstruction in pp collision events at sqrt(s) = 7 TeV. 2012.

[47] (ed.) Sphicas, P. CMS: The TriDAS project. Technical design report, Vol. 2: Data acquisition and high-level trigger. 2002.

[48] S. Dasu et al. CMS. The TriDAS project. Technical design report, vol. 1: The trigger systems. 2000.

[49] Nicholas Metropolis and S. Ulam. The monte carlo method. *Journal of the American Statistical Association*, 44(247):pp. 335–341, 1949.

[50] G Peter Lepage. A new algorithm for adaptive multidimensional integration. *Journal of Computational Physics*, 27(2):192 – 203, 1978.

[51] Setsuya Kawabata. A New version of the multidimensional integration and event generation package BASES/SPRING. *Comput.Phys.Commun.*, 88:309–326, 1995.

[52] Torbjorn Sjostrand, Stephen Mrenna, and Peter Z. Skands. PYTHIA 6.4 Physics and Manual. *JHEP*, 0605:026, 2006.

[53] Johan Alwall, Michel Herquet, Fabio Maltoni, Olivier Mattelaer, and Tim Stelzer. MadGraph 5 : Going Beyond. *JHEP*, 1106:128, 2011.

[54] Simone Alioli. NLO and Parton Showers: The POWHEG-BOX. pages 204–208, 2010.

[55] Stefano Frixione, Fabian Stoeckli, Paolo Torrielli, Bryan R. Webber, and Chris D. White. The MCaNLO 4.0 Event Generator. 2010.

[56] P. Waller, J. Ebke, and T. Brooks. "mcviz: A hep monte carlo visualizer". `https://github.com/mcviz/mcviz/wiki`, July 2012.

[57] Johan Alwall. Matching of w+jets in madevent and pythia. `https://server06.fynu.ucl.ac.be/projects/madgraph/raw-attachment/wiki/MGTalks/Wjets-270308.pdf`, March 2008.

[58] Michelangelo L. Mangano, Mauro Moretti, Fulvio Piccinini, and Michele Treccani. Matching matrix elements and shower evolution for top-quark production in hadronic collisions. *JHEP*, 0701:013, 2007.

[59] S. Catani, F. Krauss, R. Kuhn, and B.R. Webber. QCD matrix elements + parton showers. *JHEP*, 0111:063, 2001.

[60] S. Agostinelli et al. GEANT4: A Simulation toolkit. *Nucl.Instrum.Meth.*, A506:250–303, 2003.

[61] R.K. Bock, H. Grote, D. Notz, M. Regler, and (ed.) Regler, M. Data analysis techniques for high-energy physics experiments. *Camb.Monogr.Part.Phys.Nucl.Phys.Cosmol.*, 11:1–434, 2000.

[62] Kenneth Rose. Deterministic annealing for clustering, compression, classification, regression, and related optimization problems. In *Proceedings of the IEEE*, pages 2210–2239, 1998.

[63] G L Bayatian et al. *CMS Physics Technical Design Report Volume I: Detector Performance and Software*. Technical Design Report CMS. CERN, Geneva, 2006. There is an error on cover due to a technical problem for some items.

[64] Matteo Cacciari. FastJet: A Code for fast k_t clustering, and more. pages 487–490, 2006.

[65] Serguei Chatrchyan et al. Measurement of $W\gamma$ and $Z\gamma$ production in pp collisions at $\sqrt{s} = 7$ TeV. *Phys.Lett.*, B701:535–555, 2011.

[66] Kyle S. Cranmer. Kernel estimation in high-energy physics. *Comput.Phys.Commun.*, 136:198–207, 2001.

[67] The CMS Collaboration. Absolute calibration of the luminosity measurement at cms: Winter 2012 update. 2012. CMS-PAS-SMP-12-008.

[68] D Bourilkov, R C Group, and M R Whalley. LHAPDF: PDF use from the Tevatron to the LHC. 2006.

[69] S. Kretzer, H.L. Lai, F.I. Olness, and W.K. Tung. Cteq6 parton distributions with heavy quark mass effects. *Phys.Rev.*, D69:114005, 2004.

[70] Michiel Botje, Jon Butterworth, Amanda Cooper-Sarkar, Albert de Roeck, Joel Feltesse, et al. The PDF4LHC Working Group Interim Recommendations. 2011.

[71] AC Aitken. On least squares and linear combination of observations. 55:42–48, 1934.

[72] G. Cowan, K. Cranmer, E. Gross, O. Vitells. Asymptotic formulae for likelihood-based tests of new physics. *Eur.Phys.J.*, C71:1554, 2011.

[73] Lorenzo Moneta, Kevin Belasco, Kyle S. Cranmer, S. Kreiss, Alfio Lazzaro, et al. The RooStats Project. *PoS*, ACAT2010:057, 2010.

[74] F. James and M. Roos. Minuit: A System for Function Minimization and Analysis of the Parameter Errors and Correlations. *Comput.Phys.Commun.*, 10:343–367, 1975.

[75] TeVI Group. Design Report Tevatron 1 project. 1984.

[76] LEP DESIGN REPORT: VOL. 2. THE LEP MAIN RING. 1984.

[77] P.A. Aarnio et al. The DELPHI detector at LEP. *Nucl.Instrum.Meth.*, A303:233–276, 1991.

[78] The Construction of the L3 Experiment. *Nucl.Instrum.Meth.*, A289:35–102, 1990.

[79] D. Decamp et al. ALEPH: A detector for electron-positron annnihilations at LEP. *Nucl.Instrum.Meth.*, A294:121–178, 1990.

[80] K. Ahmet et al. The OPAL detector at LEP. *Nucl.Instrum.Meth.*, A305:275–319, 1991.

[81] Precision Electroweak Measurements and Constraints on the Standard Model. 2010.

[82] P. Abreu et al. Measurement of Trilinear Gauge Couplings in e^+e^- Collisions at 161-GeV and 172-GeV. *Phys.Lett.*, B423:194–206, 1998.

[83] M. Acciarri et al. Measurement of energetic single photon production at LEP. *Phys.Lett.*, B346:190–198, 1995.

[84] F. Abe et al. Measurement of $W + \gamma$ and $Z + \gamma$ cross-sections in the electron and muon channels in $S^{(1/2)} = 1.8$-TeV anti-P P collisions. 1994.

[85] Limits on anomalous neutral gauge couplings using data from Z Z and Z gamma production between 183-GeV - 208-GeV. 2001.

[86] R. Blair et al. The CDF-II detector: Technical design report. 1996.

[87] V.M. Abazov et al. D0 Run IIB upgrade technical design report. 2002.

[88] F. Abe et al. Observation of top quark production in $\overline{p}p$ collisions with the collider detector at fermilab. *Phys. Rev. Lett.*, 74:2626–2631, Apr 1995.

[89] S. Abachi et al. Search for high mass top quark production in $p\overline{p}$ collisions at $\sqrt{s} =$ 1.8 tev. *Phys. Rev. Lett.*, 74:2422–2426, Mar 1995.

[90] T. Aaltonen et al. Limits on Anomalous Trilinear Gauge Couplings in $Z\gamma$ Events from $p\bar{p}$ Collisions at $\sqrt{s} = 1.96$ TeV. *Phys.Rev.Lett.*, 107:051802, 2011.

[91] V.M. Abazov et al. Measurement of the Z gamma —gt; nu anti-nu gamma cross section and limits on anomalous Z Z gamma and Z gamma gamma couplings in p anti-p collisions at s**(1/2) = 1.96-TeV. *Phys.Rev.Lett.*, 102:201802, 2009.

[92] Georges Aad et al. Measurement of W gamma and Z gamma production cross sections in pp collisions at sqrt(s) = 7 TeV and limits on anomalous triple gauge couplings with the ATLAS detector. 2012.

[93] Serguei Chatrchyan et al. Observation of a new boson at a mass of 125 GeV with the CMS experiment at the LHC. *Phys.Lett.B*, 2012.

[94] Georges Aad et al. Observation of a new particle in the search for the Standard Model Higgs boson with the ATLAS detector at the LHC. 2012.

[95] Celine Degrande, Nicolas Greiner, Wolfgang Kilian, Olivier Mattelaer, Harrison Mebane, et al. Effective Field Theory: A Modern Approach to Anomalous Couplings. 2012.

[96] K. Hagiwara, S. Ishihara, R. Szalapski, and D. Zeppenfeld. Low energy effects of new interactions in the electroweak boson sector. *Phys. Rev. D*, 48:2182–2203, Sep 1993.

[97] G. Gounaris, J.L. Kneur, D. Zeppenfeld, Z. Ajaltouni, A. Arhrib, et al. Triple gauge boson couplings. 1996.

[98] Serguei Chatrchyan et al. Measurement of W+W- Production and Search for the Higgs Boson in pp Collisions at sqrt(s) = 7 TeV. *Phys.Lett.*, B699:25–47, 2011.

[99] Measurement of the zz production cross section and search for anomalous coupling in $2\ell 2\ell'$ final states in pp collisions at $\sqrt{s} = 7$ tev. 2012. CMS-PAS-SMP-12-007, In Preparation.

[100] U. Baur and David L. Rainwater. Probing neutral gauge boson selfinteractions in Z Z production at the Tevatron. *Int.J.Mod.Phys.*, A16S1A:315–317, 2001.

[101] Pietro Faccioli, Carlos Lourenco, Joao Seixas, and Hermine K. Wohri. Model-independent constraints on the shape parameters of dilepton angular distributions. *Phys.Rev.*, D83:056008, 2011.

[102] Pietro Faccioli, Carlos Lourenco, Joao Seixas, and Hermine K. Wohri. Rotation-invariant observables in parity-violating decays of vector particles to fermion pairs. *Phys.Rev.*, D82:096002, 2010.

[103] Faccioli, Pietro and Lourenco, Carlos and Seixas, Joao and Wohri, Hermine K. Determination of chi-c and chi-b polarizations from dilepton angular distributions in radiative decays. *Phys.Rev.*, D83:096001, 2011.

[104] Pietro Faccioli, Carlos Lourenco, and Joao Seixas. A New approach to quarkonium polarization studies. *Phys.Rev.*, D81:111502, 2010.

[105] Pietro Faccioli, Carlos Lourenco, Joao Seixas, and Hermine K. Wohri. Towards the experimental clarification of quarkonium polarization. *Eur.Phys.J.*, C69:657–673, 2010.

[106] T. Hahn. CUBA: A Library for multidimensional numerical integration. *Comput.Phys.Commun.*, 168:78–95, 2005.

[107] Wouter Verkerke and David P. Kirkby. The RooFit toolkit for data modeling. *eConf*, C0303241:MOLT007, 2003.

[108] "measurement of the y(1s), y(2s), and y(3s) polarizations in pp collisions at $\sqrt{s} = 7tev$". $CERNPreprint : CERN - PH - EP - 2012 - 205, 2012$.

Appendix A

Template Method Fit Results

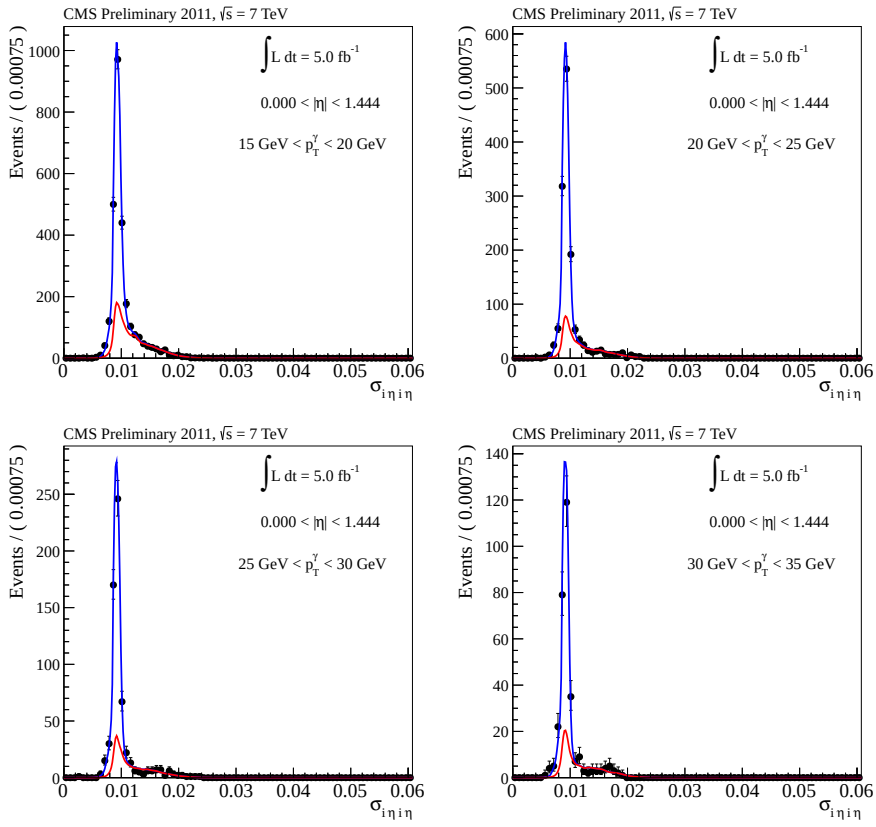

Figure A.1: Template fit results in the ECAL barrel for 15 GeV $< p_{\mathrm{T}}^{\gamma} <$ 35 GeV in the muon channel. The blue line is the signal template and the red line is the background template.

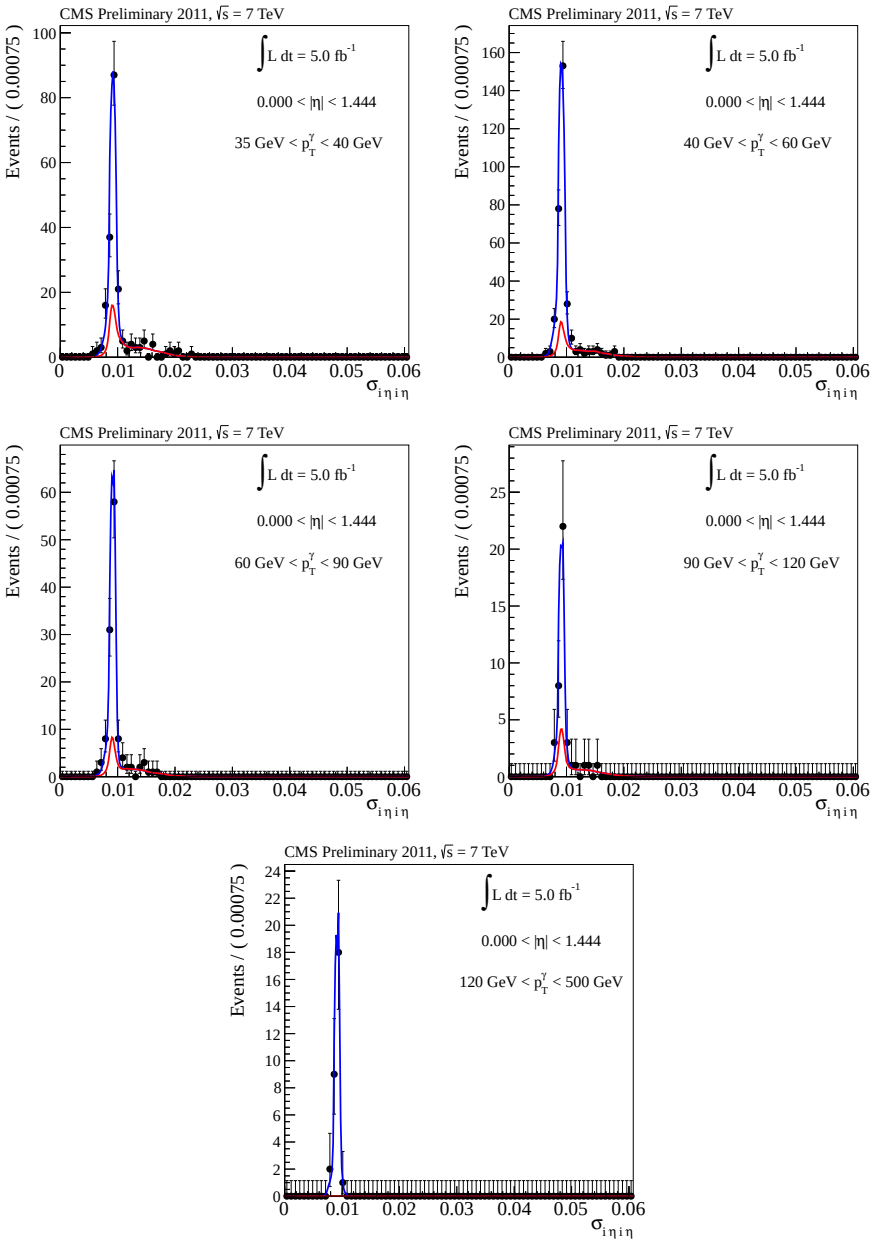

Figure A.2: Template fit results in the ECAL barrel for 35 GeV $< p_{\mathrm{T}}^{\gamma} <$ 500 GeV in the muon channel. The blue line is the signal template and the red line is the background template.

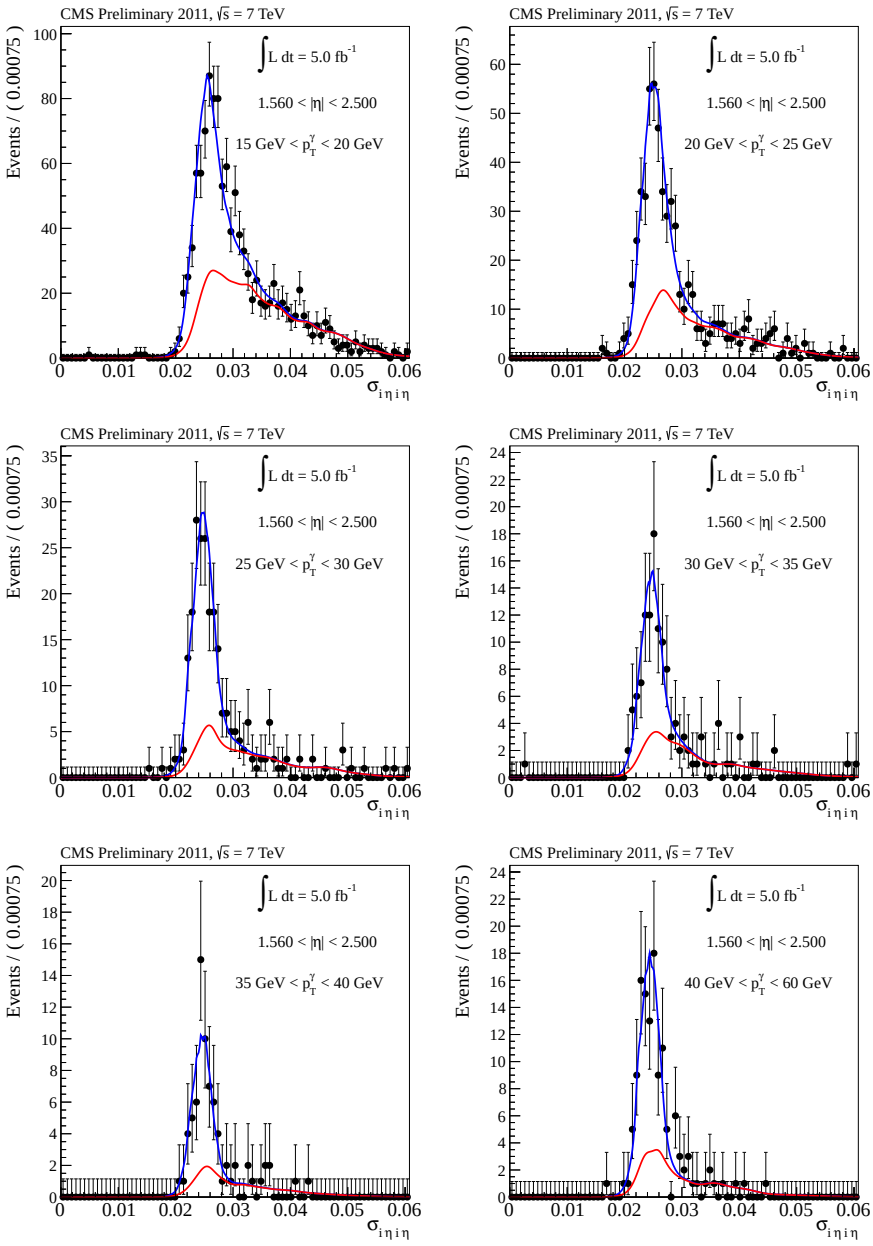

Figure A.3: Template fit results in the ECAL endcap for 15 GeV $< p_{\mathrm{T}}^{\gamma} <$ 60 GeV in the muon channel. The blue line is the signal template and the red line is the background template.

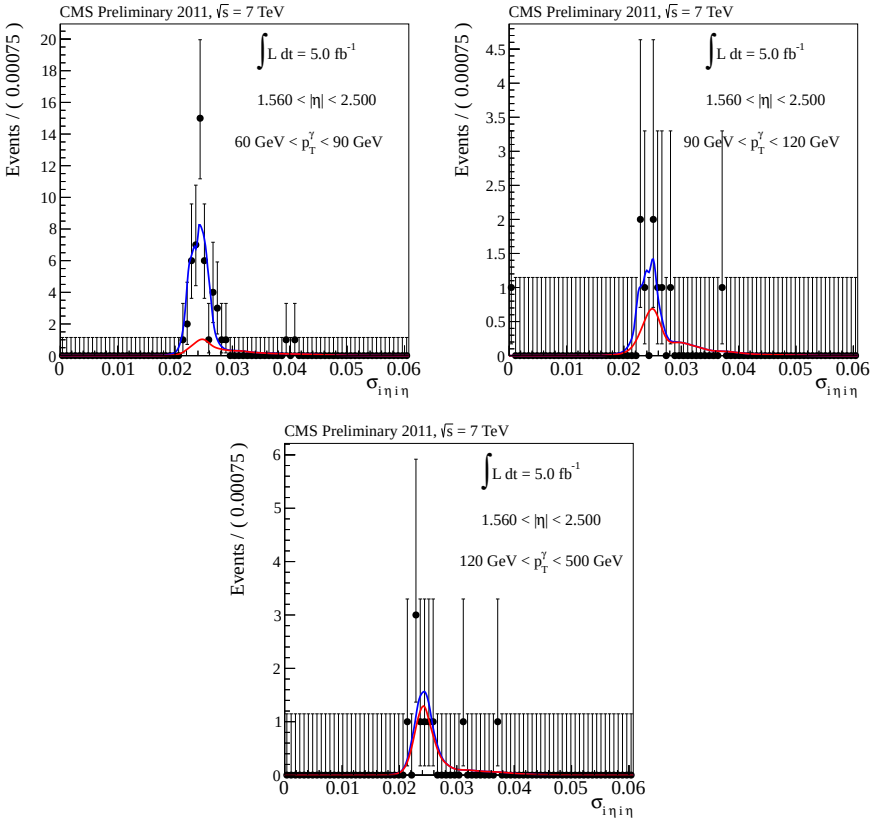

Figure A.4: Template fit results in the ECAL endcap for 60 GeV $< p_{\mathrm{T}}^{\gamma} <$ 500 GeV in the muon channel. The blue line is the signal template and the red line is the background template.

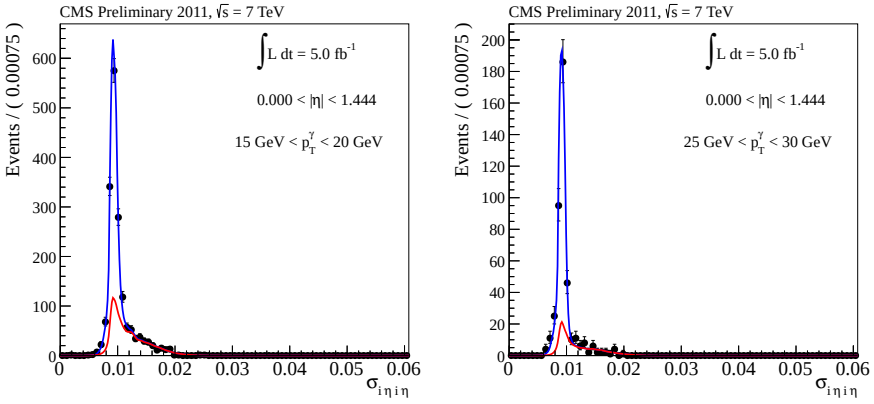

Figure A.5: Template fit results in the ECAL barrel for 15 GeV $< p_{\mathrm{T}}^{\gamma} <$ 30 GeV in the electron channel. The blue line is the signal template and the red line is the background template.

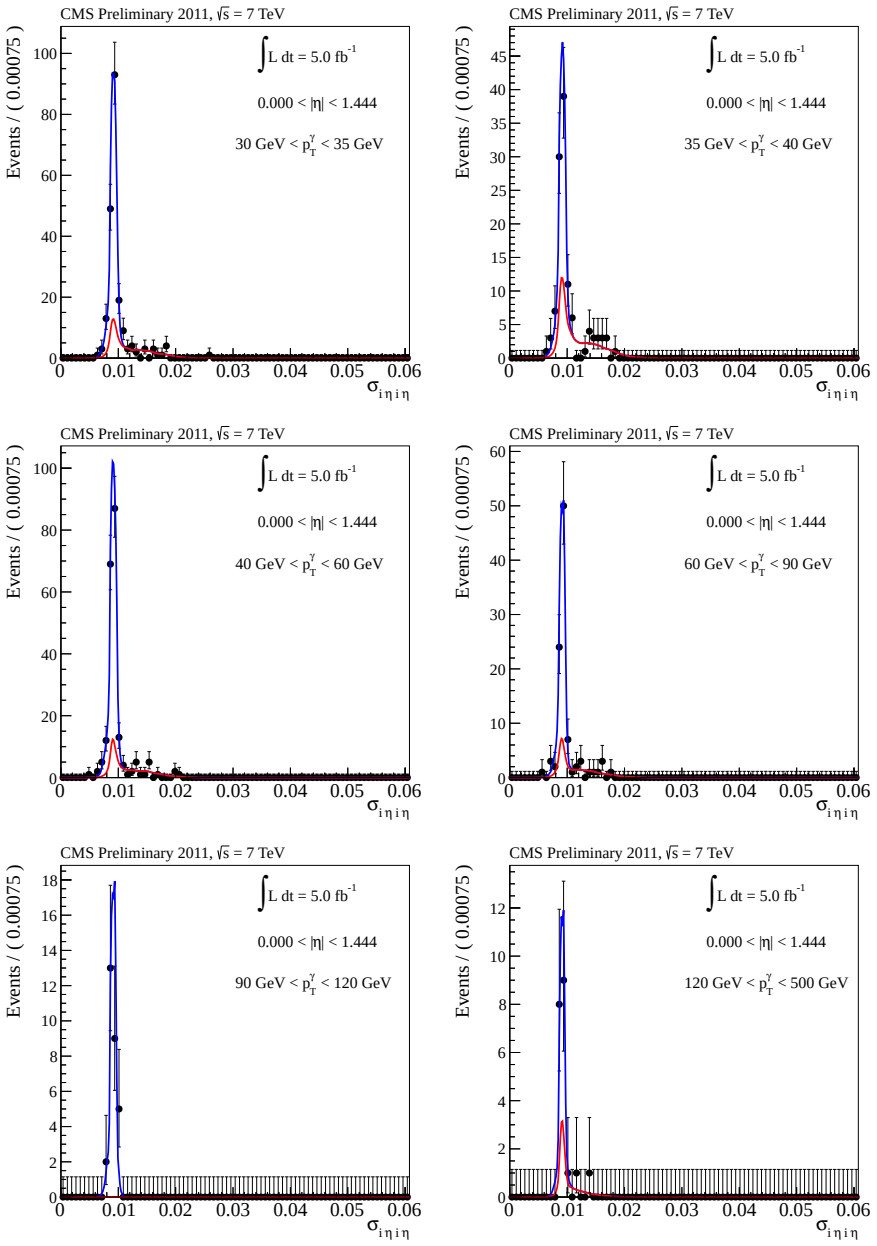

Figure A.6: Template fit results in the ECAL barrel for 30 GeV $< p_{\mathrm{T}}^{\gamma} <$ 500 GeV in the electron channel. The blue line is the signal template and the red line is the background template.

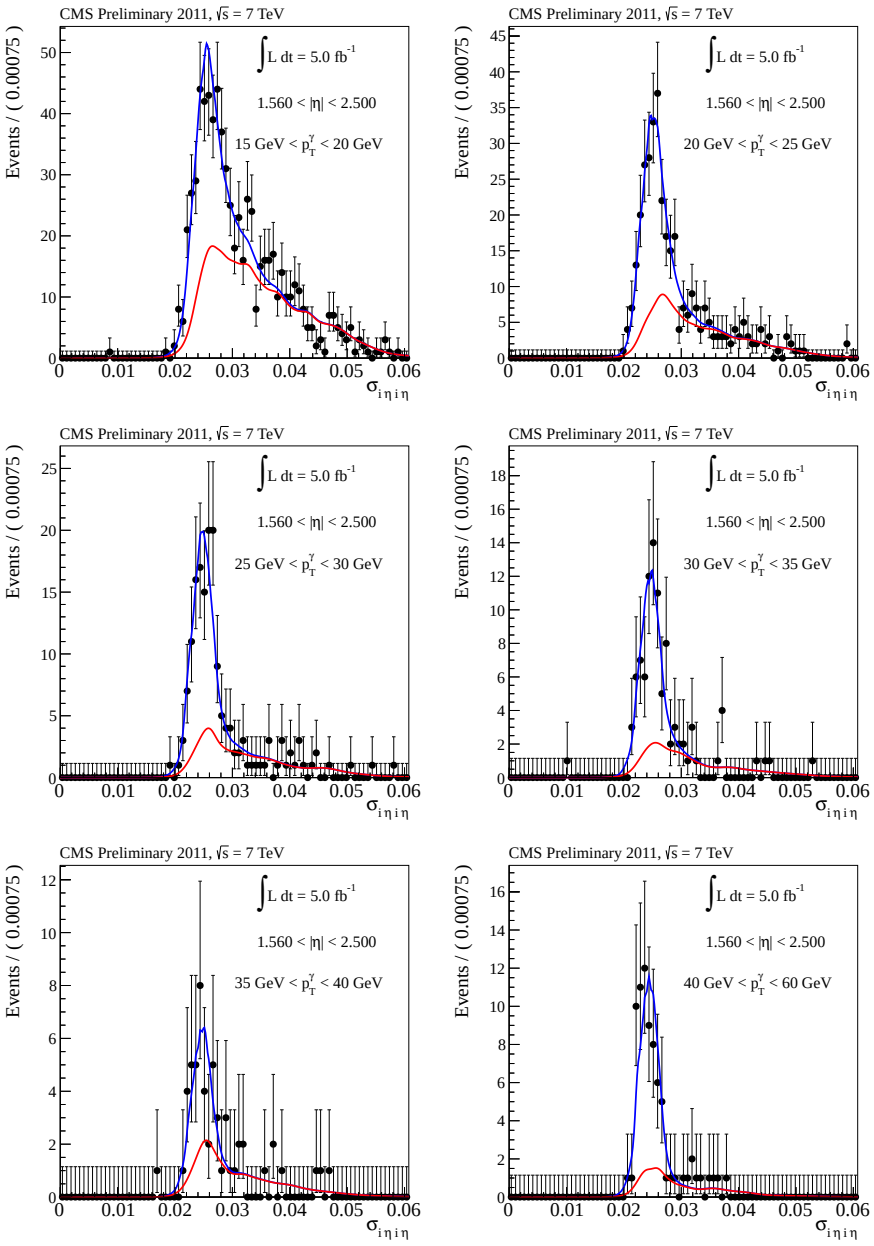

Figure A.7: Template fit results in the ECAL endcap for 15 GeV $< p_{\mathrm{T}}^{\gamma} <$ 60 GeV in the electron channel. The blue line is the signal template and the red line is the background template.

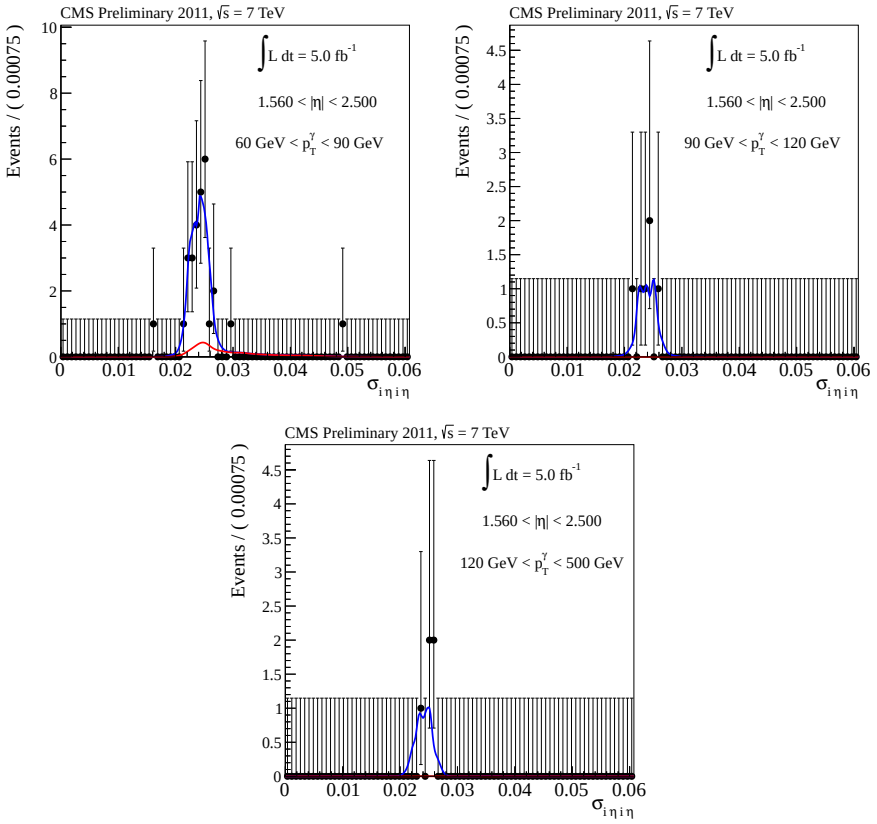

Figure A.8: Template fit results in the ECAL endcap for 60 GeV $< p_{\mathrm{T}}^{\gamma} <$ 500 GeV in the electron channel. The blue line is the signal template and the red line is the background template.

Appendix B

Other Anomalous Triple Gauge Coupling Measurements

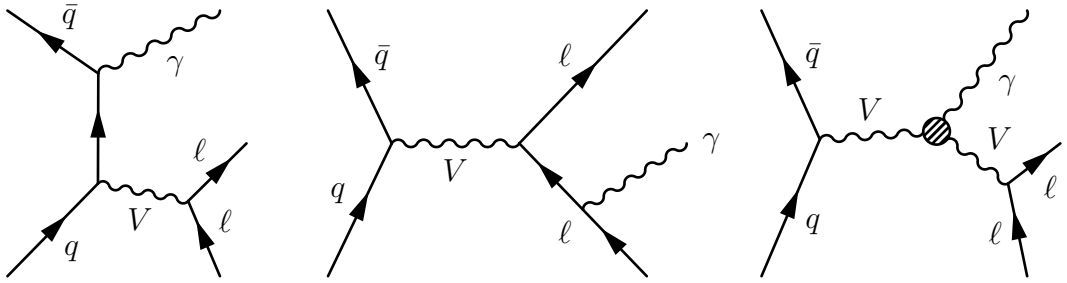

Figure B.1: The LO α_S diagrams for Vγ production, where V=W,Z,γ^*. The Wγ coupling occurs naturally in the SM, unlike Zγ. In the case of Wγ production the charged lepton is radiating the photon in the FSR diagram.

The measurement of and limits on anomalous triple gauge couplings presented for the Zγ analysis were performed in tandem with the search for anomalous couplings in the Wγ. The same class of Feynman diagrams, Figure B.1, describes the production of Wγ as for Zγ with the exception that there is a naturally arising triple gauge vertex between the W$^{\pm}$ bosons since they are charged. Instead of the couplings $h_i^{Z/\gamma}$ being introduces in the vertex function, the charged anomalous triple gauge couplings are inserted into the SM using a lagrangian approach [23], where the lagrangian is given

by:

$$\begin{aligned}
\mathcal{L}_{WWV}/g_{WWV} &= ig_1^V\left(W_{\mu\nu}^\dagger W^\mu V^\nu - W_\mu^\dagger V_\nu W^{\mu\nu}\right) + i\kappa_V W_\mu^\dagger W_\nu V^{\mu\nu} \\
&+ \frac{i\lambda_V}{m_W^2} W_{\lambda\mu}^\dagger W_\nu^\mu V^{\nu\lambda} - g_4^V W_\mu^\dagger W_\nu\left(\partial^\mu V^\nu + \partial^\nu V^\mu\right) \\
&+ g_5^V \varepsilon^{\mu\nu\rho\sigma}\left(W_\mu^\dagger \overleftrightarrow{\partial}_\rho W_\nu\right) + i\tilde{\kappa}_V W_\mu^\dagger W_\nu \tilde{V}^{\mu\nu} \\
&+ \frac{i\tilde{\lambda}_V}{m_W^2} W_{\lambda\mu}^\dagger W_\nu^\mu \tilde{V}^{\nu\lambda}
\end{aligned}$$

, where V = Z, γ. The anomalous couplings $\Delta g_1^V = g_1^V - 1$, $\Delta\kappa_V = \kappa_V - 1$, and λ_V are related in the 'LEP parameterization' [96,97], which is motivated by requiring the non-zero anomalous couplings to not affect gauge, C, or P invariance. The general LEP parameterization of the couplings is:

$$\Delta\kappa_Z = \Delta g_1^Z - \Delta\kappa_\gamma \tan^2\theta_W \quad \text{and} \quad \lambda_Z = \lambda_\gamma = \lambda \tag{B.1}$$

and in the 'equal couplings' scenario, where the γWW and ZWW couplings are set equal and enforces the relation $\Delta g_1^Z = \Delta g_1^\gamma = 0$, leaving two free anomalous couplings to study using the Wγ final state.

The CMS Collaboration(CITE ME – Vγ) set limits on $\Delta\kappa_\gamma$ and λ_γ using the same limit setting program 'aTGCRooStats', developed by the author, to calculate the 95% CLs interval. The combined one and two dimensional limits set with the electron and muon channels of the Wγ analysis are shown in Figure B.2. As with the limits on Zγ no form factor or energy dependence of the coupling is assumed in the limits on Wγ aTGCs. The analysis to set the limits on these parameters using the WZ diboson process is currently in progress, using the same limit setting techniques and programs. The corresponding analysis using WW exists as a 2010 analysis on 36 pb^{-1} [98], where a preliminary version of aTGCRooStats was used as a cross check. The WW result based on the full 2011 dataset is in preparation.

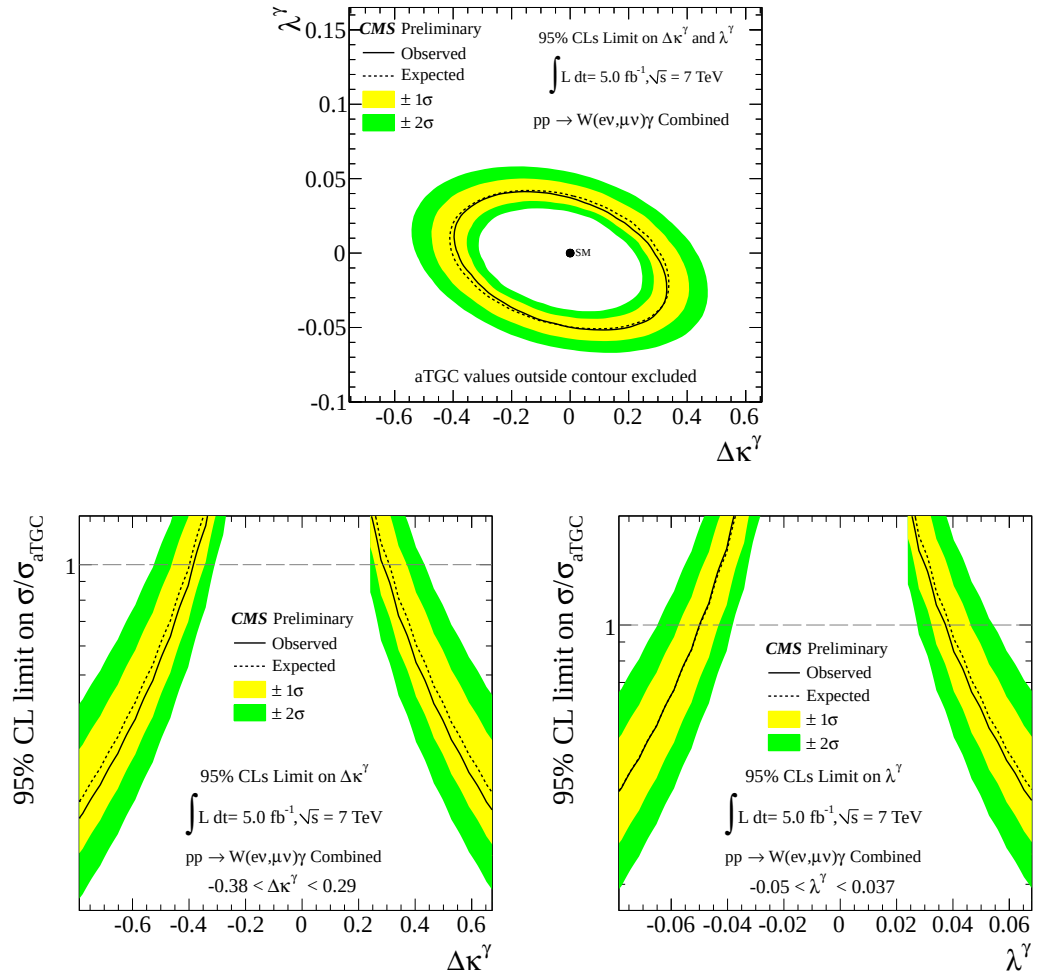

Figure B.2: The two (top) and one (bottom) dimensional limits on $\Delta\kappa_\gamma$ and λ_γ set with the electron and muon channels of the Wγ analysis. The two bottom plots are cross sections of the top plot when the coupling not being plotted is zero.

Diboson processes with a massless, 'on-shell', photon in the final state, Wγ and Zγ, have the a unique advantage since they directly observe the photon from the interaction. However, the diboson processes with two massive bosons in the final state are important as well in the context of aTGCs since there are additional aTGCs or overlapping sets of aTGCs when considering these processes. The LO Feynman diagrams for these processes is given in Figure B.3. The charged triple gauge couplings, resulting in the WW and WZ final states, all share the same set of couplings when

considered under the LEP parameterization. These channels can be combined to gain improvement in the statistical power of the limits and to test the universality conditions of the equal couplings scenario.

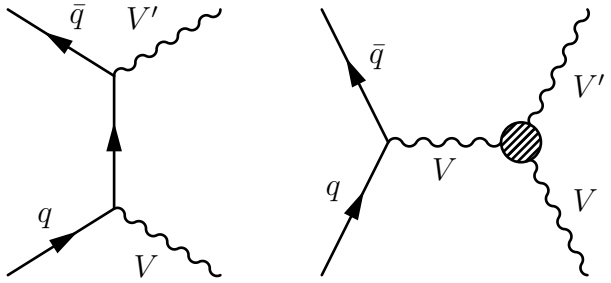

Figure B.3: The LO α_S diagrams for VV production, where V,V'=W,Z. TGCs occur naturally in the SM between the massive vector bosons, except ZZ.

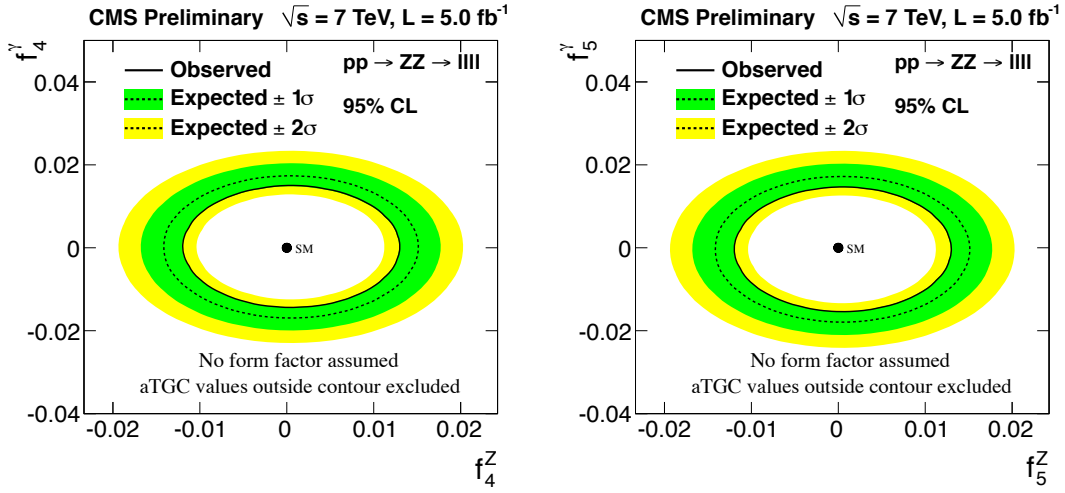

Figure B.4: The two dimensional limits for ZZ anomalous triple gauge couplings. The observed limit is within one sigma of the observed and sets the most stringent limits to date on ZZ aTGCs. [99]

The ZZ anomalous triple gauge couplings are treated in a similar fashion to the Zγ couplings in that they are introduced via a vertex function that contains the triple gauge couplings. The vertex function for ZZ aTGCs is [23, 100]:

$$g_{ZZV}\Gamma^{\alpha\beta\mu}_{ZZV} = e\frac{P^2 - M_V^2}{M_Z^2}\left[if_4^V\left(P^\alpha g^{\mu\beta} + P^\beta g^{\mu\alpha}\right) + if_5^V\epsilon^{\mu\alpha\beta\rho}(q_1 - q_2)_\rho\right],$$

where P, q_1, and q_2 are labeled the same as in Figure 2.11, except q_2 is an outgoing Z boson. As in Zγ, the incoming particle may be an off-shell photon or a Z, giving rise to two sets of couplings depending on the incoming particle. In the CMS analysis of ZZ anomalous triple gauge couplings [99], using aTGCRooStats, only the decays of Zs into light leptons are considered, yielding low background. However, instead of using the boson p_{T}, limits are set using the four-lepton invariant mass since in the case of ZZ production it yields equivalent signal significance for aTGCs and doesn't change shape when including higher order corrections. The limits set are given in Table B.1 for one dimensional limits and Figure B.4 for two dimensional limits. As with the limits on Zγ no form factor or energy dependence of the coupling is assumed in the limits on ZZ aTGCs.

Channel	f_4^Z	f_5^Z	f_4^γ	f_5^γ
$ZZ \to \ell\ell\ell\ell$	[-0.012,0.013]	[-0.012,0.013]	[-0.014,0.014]	[-0.015,0.015]

Table B.1: The one dimensional anomalous triple gauge coupling limits for ZZ.

With the completion of the WZ and WW results, CMS will provide a theoretically rich set of results measuring very precisely the interactions, or lack thereof, of the four electroweak bosons. The ATLAS experiment also performs these measurements and combinations of the 2011 and, later, 2012 aTGC results are foreseen.

Appendix C

A Data-Driven Method for Extraction of Spin Alignment Anisotropy Parameters

The measurement of spin alignment, or 'polarization', is a powerful tool for examining the ways in which a particle or system of particles is produced. The spin projection J_z, with z the spin quantization axis, determines how decay products are oriented in the final state since the decay products' spin projections must sum to yield the spin projection of the parent particle. Considering the case of Z production it is apparent that a particular production mode corresponds to a particular polarization of the Z, since the total spin alignment of the initial quarks annhilating to form the Z determines this. Furthermore any angular distributions measured from the decay will be the average of all polarizations being produced, weighted by their rates. A description of the angular distributions of vector particles' decay products and constraints on those distributions are given in [101, 102]. An extension to higher dimensional angular distributions is given in the context of χ_c decays [103], but is

equally applicable to the Zγ final state since it also a final state that consists of a heavy vector particle and a photon.

Polarization measurements are canonically performed by taking a physical polarization distribution, such as:

$$w(\cos\theta, \varphi) = \lambda_\theta \cos^2\theta + \lambda_\varphi \sin^2\theta \cos 2\varphi + \lambda_{\theta\varphi} \sin 2\theta \cos\varphi \tag{C.1}$$

for parity conserving decays of vector particles, and then modifying this function by the detector acceptance and efficiency in a bin of p_{T} and rapidity of the parent particle. $\cos\theta$ and φ are the polar and azimuthal helicity angles measured in the center of mass frame of a particle, which decribe the decay angles of the daughter particles in the center of mass frame with respect to a chosen z-axis. The acceptance and efficiency are commonly given as 'maps' in the angular variables being measured, such a map is shown in Figure C.1 This naïvely produces a model of the observed polarization distribution including all detector effects and is then used to measure the observed angular distributions.

However, a problem arises when attempting to measure these distributions from data. The support of the theoeretical polarization distribution being measured depends in a multidimensional way, *i.e.* in all angles of the distribution, on the kinematics of the parent particle and the cuts on (*i.e.* kinematic and geometric acceptance) and efficiency of finding the decay products. This problem was first described in the context of b-physics [104,105], where the solution of measuring the distributions fully differentially in all angles was given. This solves the problem of integrating over zeros in the acceptance distribution as well as resolving the ambiguity in the polarization measurement if the natural polarization frame is rotated away from the experimental one. However, this significant advancement does not address the long standing issue of the dependence of polarization measurements on monte carlo for estimation

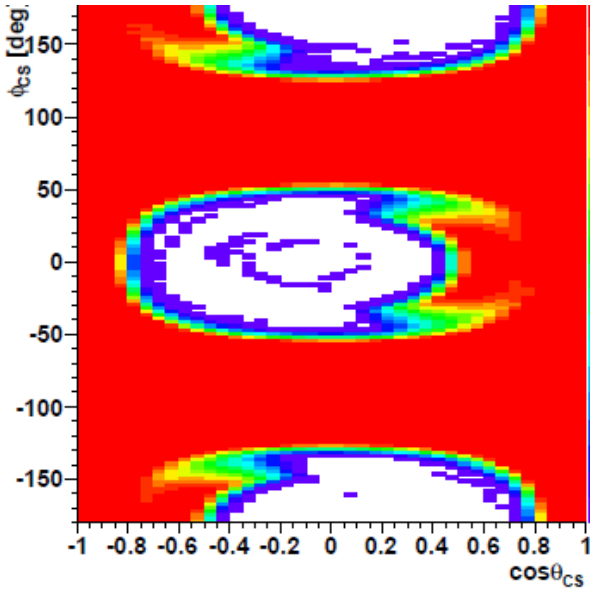

Figure C.1: A typical acceptance map used in polarization measurements, binned in $\cos\theta$ and φ.

of kinematic acceptance.

If the acceptance in the MC does not model the acceptance in data, the polarization measurement will be biased, since any remaining differences between the acceptance-corrected distribution being determined with a fit and the real detector acceptance will be accounted for by variation of the parameters of the polarization distribution. These differences can arise from using different signal models in MC that can change the average acceptance due to having a different kinematic distribution from the data. Therefore a method for determining the acceptance from data is required, to remove acceptance modeling issues. Furthermore, the absolute efficiencies are also used to deform the physical polarization function. If the efficiencies in data and monte carlo are different, assuming the MC efficiencies results in the same kind of bias.

These problems all arise from a reliance on the MC and use of averages to determine the deformations in the physical polarization function caused by acceptance and

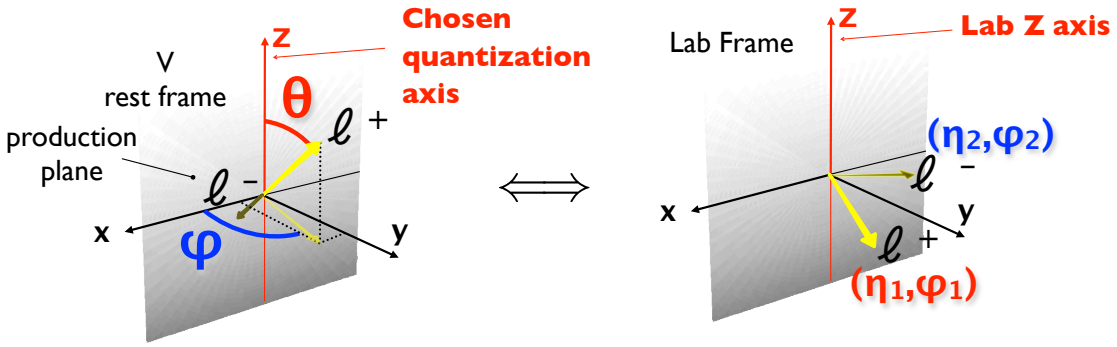

Figure C.2: The one-to-one correspondance between a chosen polarization frame and the lab frame, by way of a unique lorentz boost.

efficiency. If, however, the acceptance is considered per-event and is interpreted as the full decay phase space of one parent particle, a key relation arises. Per event, the kinematics of the parent particle are completely determined from the decay products and need not be averaged over. Furthermore, this treatment fixes the lorentz boost between center of mass and lab frames shown in Figure C.2, and from this the entire decay phase space of the parent particle can be calculated unambiguously using on-the-fly Monte-Carlo [106] for each event to integrate the total avaiable phase space, thus determining the support of the polarization function. This effectively re-decays the observed final state, determining exactly what final state kinematics are within detector acceptance and can contribute to the result.

Since there is now a unique correspondence between center of mass and lab frames, kinematic cuts in the lab frame correspond directly to the center of mass frame. Therefore, so long as the cuts are within the sensitive region of a detector, the kinematic part of the acceptance can be completely factorized out and calculated from the known initial state kinematics, since the polarization function must be zero outside of the kinematic acceptance. An example of the phase space of Z decay, using the kinematic cuts of the Zγ analysis, is shown in Figure C.3. This causes all other de-

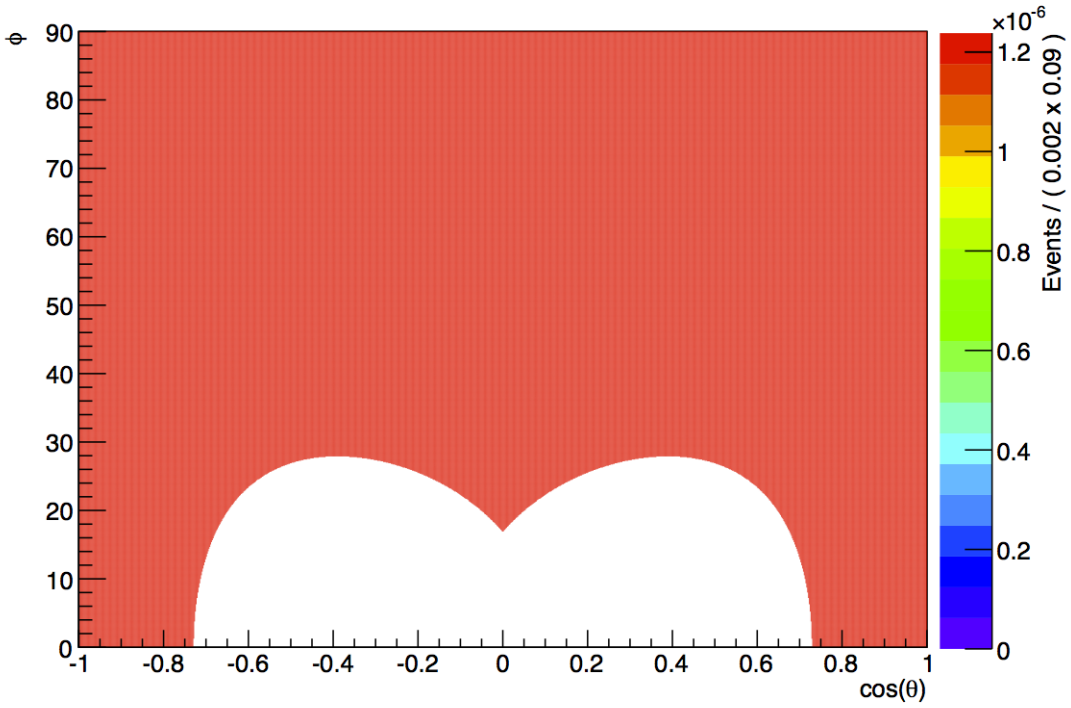

Figure C.3: The phase space scan of the decay of a Z boson with $p_{\mathrm{T}} = 30$ GeV using the Zγ analysis cuts, the red regions are where both leptons are within kinematic cuts and white is where at least one is not.

formations in the physical polarization function to be described by efficiencies, which can be measured from data with lab-frame coordinates using tag-and-probe and applied in-situ to the on-the-fly MC since the lab frame momenta of decay products are uniquely determined. This produces a realistic estimation of the rates of a specfic parent particle being detected in any part of the detector within the kinematic cuts. This determines unabiguously the deformations in the physical polarization function both acceptance and efficiency.

To perform a fit of the physical polarization function this technique is performed for each observed particle. The general conditional probability distribution function,

PDF, used to describe the angular distribution, in the 2D case is:

$$p(\cos\theta, \varphi|\tilde{p}, \vec{\lambda}) = \frac{\varepsilon(p_1, p_2) w(\cos\theta, \varphi|\tilde{p}, \vec{\lambda})}{\int\int_{\mathcal{R}} \varepsilon(\cos\theta, \varphi) w(\cos\theta, \varphi|\tilde{p}, \vec{\lambda}) \mathrm{d}\cos\theta \mathrm{d}\varphi} \tag{C.2}$$

where $\tilde{p}$ is the momentum of the parent particle, p_1 and p_2 are the momenta of the daughter particles, ε is the efficiency of finding the lepton pair in the detector and $\mathcal{R}$ is region of phase space where both final state particles are within kinematic requirements. This defines, for a given initial momentum, a probability distribution with exactly the support of the data and includes all efficiency effects. Furthermore, this alleviates the problems related to using MC acceptance maps since at no point in the calculating is any distribution ever assumed aside from the distribution being fit for, which is required for proper normalization.

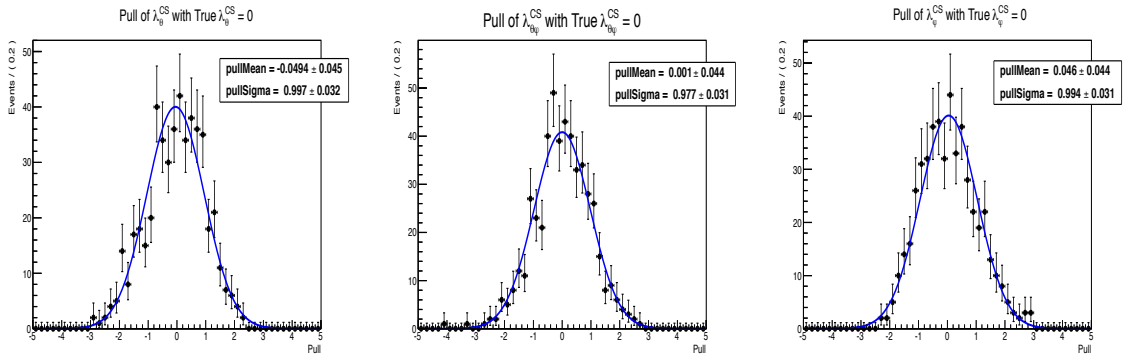

Figure C.4: The pull distributions of the polarization parameters given in when all true values of parameters are zero, *i.e.* isotropic distribution. All distributions have a mean consistent with zero and a standard deviation of one, implying that there is no bias.

Since the PDF is conditional on the initial state momentum, it may be applied to each observed event and the product forms a likelihood that convolutes over all events, with each PDF having the appropriate support for its initial state. The negative-log-likelihood can then be minimized and a solution to the coefficients in the polarization distribution estimated. Additional models and observables, such as invariant mass, may be added to the likelihood to separate species of events in a data sample and then

measure their polarization simultaneously. Extensions to higher-dimensional angular distributions are straightforward since the total acceptance is the product of all two body decays in the total decay, for instance 2 sets of 2 angles for Zγ and 3 sets of 2 angles for ZZ.

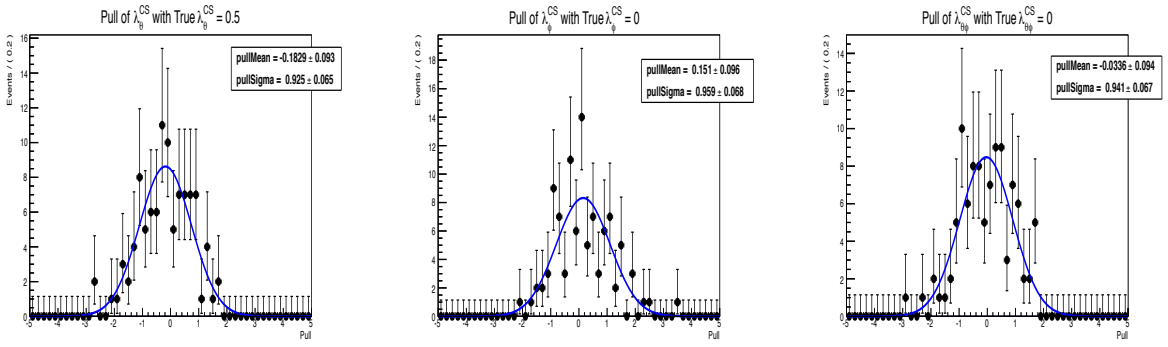

Figure C.5: The pull distributions of the polarization parameters given in when true $\lambda_\theta = 0.5$ and all other parameters are zero. All distributions have a mean consistent with zero and a standard deviation of one, implying that there is no bias.

This procedure has been implemented in C++ as extensions to the RooFit framework [107] for use in b-physics and electroweak physics. Pull distributions, showing that the procedure itself is unbiased for zero polarization and large vector-like polarizations are shown in Figures C.4, C.5, and C.6. This technique requires precise knowledge of the detector efficiencies and accurate models of signal and background. The application of this technique to the Zγ final state is in progress, pending precise determination of the absolute photon ID efficiencies. Additionally, a similar technique to measure the polarization of the upsilon 1S, 2S, and 3S is completed and soon to be published by the CMS collboration [108].

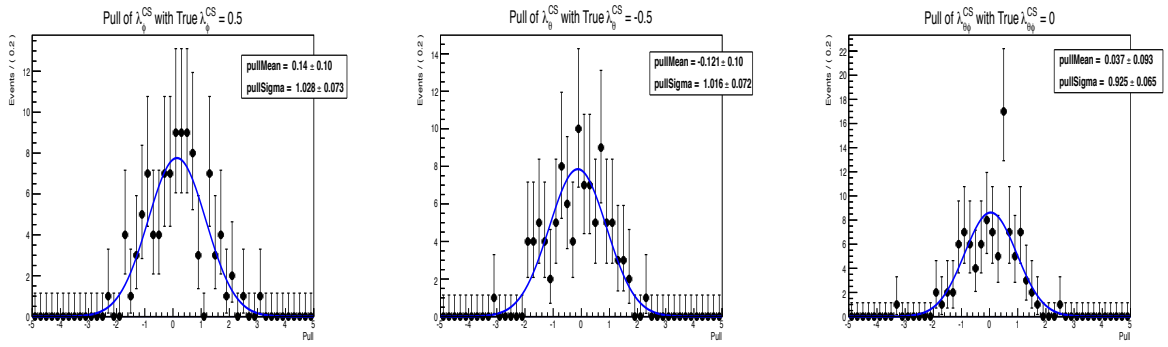

Figure C.6: The pull distributions of the polarization parameters given in when true $\lambda_\theta = -0.5$ and all other parameters are zero. All distributions have a mean consistent with zero and a standard deviation of one, implying that there is no bias.